UNIVERSIDAD DE GUANAJUATO

CENTRO DE INVESTIGACIONES EN ÓPTICA A.C.

$Bi_{12}TiO_{20}$ Fiber Optic Voltage Sensor for Industrial Applications

by

FRANCISCO GERARDO PEÑA LECONA

Submitted in partial fulfillment of the
requirements for the degree of

Doctor en Ciencias (Óptica)

May, 2004

Universidad de Guanajuato
Centro de Investigaciones en Óptica

$Bi_{12}TiO_{20}$ FIBER OPTIC VOLTAGE SENSOR FOR INDUSTRIAL APPLICATIONS

by

FRANCISCO GERARDO PEÑA LECONA

Submitted in partial fulfillment of the requirements for the degree of

Doctor en Ciencias (Óptica)

Asesor: Dr. Juan Francisco Mosiño
Co-Asesor: Dr. Valery N. Filippov

May, 2004

Dedicatory

This thesis and all the effort that I spent during my doctorate studies, are dedicated to my adorable, loving and beautiful wife

Blanca Rocío

that is my perfect complement and whom I love and I admire so much and that without her, I would never have done this project.

To my adorable daughters

Natalia** and **Regina

that are, together with their mother, the unique reason of my existence.

With all the love of my heart.

Preface

There has been a significant progress during the last years toward the development of a new class of sensors that use fiber optics. These sensors are capable to detect acoustic fields, lineal and rotational acceleration, electric and magnetic fields, and many other physical parameters. In general, the sensor modulates some feature of the luminous wave in an optic fiber as the intensity or the phase. The modulation of the phase usually becomes modulation of intensity before it is carried out the detection. This can be achieved by means of an optic interferometer or with the use of electro-optic materials. The resulting signals (intensity or phase) can be measured far from places outside of the sensor (a mechanism of the type transducer-modulator-demodulator) by means of a system of signal transmission for fiber optic. The optic signal can be in an analogical or discrete way and the system can operate with or without the optic-to-electric signal conversion or electric-to-optics. Even for the simplest case, in the one that a visual field or an image will be transmitted in a fiber cable, the own fiber can work as a sensor and should be considered all the aspects to achieve the conduction of the luminous wave through the fiber.

The content of the present dissertation is a contribution to these multiple applications that has the fiber optics in the land of the science. In particular, the study concentrates on the use of the optic fiber as a guide of luminous wave besides an electro-optic crystal, both in an arrangement for the voltage measurement. Voltage sensors based on optical fiber have been study object in the recent years and along which the authors have used diverse technical and elements in order to achieving a high sensitivity in the measurement and a high stability again the variations of temperature mainly.

This dissertation introduces the basic concepts of the fundamental configuration proposed for the used voltage sensor. Shows the theory that sustains each one of the carried out experiments. Also, provides and discusses the experimental results obtained, all this with the purpose and the effort of throwing a new light in the applicable measurement techniques to the industry where the environmental conditions are usually a hard test for the devices and where the security for people should be primordial.

Acknowledgements

I wish to thank to my advisor Professor Valery Nicolai Filippov for encourage me to do research in fibre optic sensors, for his teaching and for his guidance that led me to the great satisfaction that I have experienced through the development of my doctorate studies.

To my advisor and friend Dr. Juan Francisco Mosiño for his valuable help at the top of my doctorate studies and the friendship that he gives me.

I am especially indebted with my great friend Dr. René Martínez Celorio for all the personal and academic attention offered since the first day that I began with my studies and for the whole scientific instruction that I have received from him.

Thanks to my class partners José Vega and Juan José Soto that were moreover my friends.

Thanks to the academic personnel, technician and administrative of the CIO for the whole received help, especially to Angeles Sánchez and Guillermina Muñiz that have been great persons and they will be always my friends.

To CONACyT, CONCyTEG and CIO for all the helpfull that they gave me during my studies.

Agradecimientos

Más que hacer una traducción, quisiera extender mis agradecimientos.

Agradezco a mi padre Rufino Peña Valenzuela y a mi madre Susana Lecona López por su infinita paciencia, el cuidado en las bases de mi educación y todo el amor que me tienen.

A mis hermanos Antonio, Edmundo, Mauro, Alfredo y Rufino y a mis hermanas Carmen, Isabel y Susana, a quienes amo y admiro mucho, por todo el cariño y comprensión que me han brindado a lo largo de mi vida.

Agradezco a Dios por haberme permitido llegar al fin de este proyecto, por todas la bendiciones que he estado recibiendo a lo largo de mi vida y por todo el más sublime conocimiento que jamás adquiriré en otra parte fuera de su Palabra.

Finalmente, deseo agradecer a todos mis demás parientes, amigos, compañeros del CIO y a toda esa gente que me dio una palabra de aliento cuando más lo necesité.

Table of contents

$Bi_{12}TiO_{20}$ Fiber Optic Voltage Sensor for Industrial Application

Content

List of Figures

Chapter two

Chapter three

Chapter Four

Chapter Five

Chapter Six

List of tables

Chapter One:

Introduction

§1.1 Background

A sensor system or simply sensor is usually made up of a transducer device, a communication channel and a subsystem for generating and/or detecting, treating processing and conditioning the signal, all of these being either integrated or not integrated. If luminous radiation is used in any of the subsystems the photonic system is understood to be an Optical Sensor (OS) [1]. In general, an OS is a photonic system in which the measured object magnitude or input signal (V_i) introduces modifications or modulations in some of the characteristics of light in an optical system. After being detected, processed and conditioned, the system will deliver an output signal (V_0), usually in the electric domain, which will be a valid reproduction of the object variable. The transmitted or reflected light can be modulated by the modulating signal in its amplitude, phase, frequency or polarization characteristics. In accordance with this concept, if any of the processes or parts use fiber-optic technology, then we have a fiber optic sensor (FOS) that is a subdivision of OS. It is well known that the propagation modes of the light in fibers possess polarization properties and these properties can be influenced by external conditions. Therefore, it might thus be possible to use fibers as indicators of those external conditions, that is, to use them as measurement sensor [2].

Development of FOS began in earnest in 1977 even though some isolated demonstrations preceded this date [3]. Ever since, a great quantity of ideas has been proposed and several techniques have been discovered for different measurements and applications.

FOS technology has matured to the point in which the impact of this technology is now evident. FOS offers several advantages in those that are included: immunity to the electromagnetic interference, lightweight, small size, high sensibility, and large bandwidth. They have the versatility of being configured in arbitrary shapes and they offer a common

technological base in the devices to sensing different physical perturbations (acoustic, magnetic, temperature, rotation, voltage, current, etc.) [4]. FOS can be built to be used in high voltage, high temperature, corrosive and other environmental conditions, besides the inherent compatibility with technology of remote sensing. The progress is demonstrating that these advantages have been substantial in the last years that it was considered the use of the fiber optics for applications in the industry of the electricity supply where we would have many advantages over traditional techniques [5,6].

For example, the traditional techniques used for voltage measurement in the industry have begun to be substituted by FOS for measurement of electric and magnetic fields and electrical current, because of their inherently dielectric nature. They provide galvanic isolation of the sensor head from ground potential, are less sensitive to electromagnetic interference, generally are of small size, and provide superior safety. Nearly all electric and magnetic field sensors based upon fiber optics are hybrid devices; that is, the fiber is attached to some other material and is used to monitor any changes in that material with electric and magnetic fields. This is required for electric fields since the intrinsic inversion symmetry of the glass matrix of the optical fiber precludes a Pockels effect; it is required for magnetic fields because the Verdet constant of telecommunication optical fiber is very small [7,8].

§1.2 Justification

There are three fundamental mechanisms for the measurement of electric fields: *electrostatic induction*, *electrostatic forces* and *electrophysical phenomena*.

Electrostatic induction mechanism has been the traditional method for the measurement of high voltage in the industry since years [9]. Using the *electrostatic induction* mechanism is possible to measure high voltage up to about 200 kV and several forms of voltmeters have been devised. These voltmeters are easy to manage and can be connected directly across the test circuit to take the measure. The Abraham voltmeter is the most

commonly used electrostatic meter in high voltage testing equipment and for industrial applications [9].

The principle of the *electrostatic induction* is very known and we can summarize as follows: When two parallel conducting plates (with cross section area A and spacing x) are charged (q) and have a potential difference V, then the energy stored W is given by: $W = \frac{1}{2}CV^2$ and the change $dW = \frac{1}{2}V^2 dC = Fdx$.

Therefore, the force can be given in terms of the capacitance change as:

$$F = \frac{1}{2}V^2 \frac{dC}{dx} \tag{1.1}$$

For uniform field, the capacitance $C = \frac{A\varepsilon}{x}$ where ε is the relative permittivity of the medium. Finally,

$$F = -\frac{1}{2}A\varepsilon \frac{V^2}{x^2} \tag{1.2}$$

It is thus seen that the force of attraction is proportional to the square of the potential difference applied, so that the meter reads the square value (or can be marked to read the rms value).

Electrostatic voltmeters of the attracted disc type may be connected across the high voltage circuit directly without the use of any potential divider or other reduction method and can be used to measure both a.c. and d.c. voltages .

Nevertheless, owing to the difficulty of the designing electrostatic voltmeters for the measurement of extra high voltages which will be free from errors due to corona effects, within the instrument, and to the external electrostatic fields, a number of special methods have been devised for the same purpose.

Other mechanisms for high voltage measurement based on the *electrostatic induction* are by using transformers and potential dividers [9]. The spark over of the sphere gaps and other type of gaps are also used, especially in the calibration of meters in high voltage measurements.

However, as we can deduce, the main disadvantage of the methods based on *electrostatic induction* is, in general, the disturbance over the field to be measured. All of them rely on the accurate measurement of the current resulting from the time variation of the charges induced on a metallic body immersed in the field. Therefore, this mechanism is not suitable for use with fiber optics.

The second mechanism mentioned before as *electrostatic forces* consists in the measurement of high voltage using a variable gap in a Fabry-Perot micro cavity [10,11]. Electric fields can be measured due the attractive and the repulsive forces over a movable mirror attached to a diaphragm plate of the Fabry–Perot cavity. These forces produce a relative variation of the reflectivity (or transmissivity) due the displacement of the diaphragm and this force is proportional to the electric field to be measured. We can summarize the *electrostatic force* mechanism as follows: Whenever a conductor is placed into an electric field, the free electrons in the material rearrange themselves in such a way as to render its interior field-free. This electron arrangement gives place to an induced charge on the surface of the conductor. However, the net charge in the body remains zero. The Coulombic attraction between the induced surface charge and the external electric field E_0, develops an electrostatic force density F_s which acts normal to the surface of the conductor, for otherwise the charges would move along the surface contradicting the assumption of an equipotential surface. The magnitude of F_s is given by [12]:

$$F_s = \frac{\varepsilon_0}{2} E_{surface}^2 \tag{1.3}$$

where $E_{surface}$ is the intensity of the field right at the surface of the conductor and ε_0 is the permittivity in vacuum. The magnitude and distribution of $E_{surface}$ is the result of the superposition of the applied field E_0 plus the field resulting from the induced charges E_i. Hence, the magnitude of $E_{surface}$ is a function of position and strongly dependent on the geometry of the conductive body.

By combining the concept of a Faraday cage with an optical interferometer it is possible to measure the low pressure due F_s. Since the transmissivity (or reflectivity) of a Fabry-Perot cavity is extremely sensitive to changes in the length of the cavity which in this

case is caused by a differential pressure acting upon a movable mirror arrangement at one end of the cavity.

The reflectance of a Fabry-Perot will be a function of spacing, index of refraction, mirror reflectivities and wavelength. Assuming that the mirrors are lossless, the reflected intensity is given as follows [13]:

$$\frac{I_r}{I_0} = \frac{4\sqrt{R_1 R_2}\,\sin^2\left(\frac{2\pi h}{\lambda}\right)}{\left(1-\sqrt{R_1 R_2}\right)^2 + 4\sqrt{R_1 R_2}\,\sin^2\left(\frac{2\pi h}{\lambda}\right)} \tag{1.4}$$

with $h = h_0 + \delta h$; where R_1 and R_2 are the mirror relectivities, h is the variable gap, h_0 is the height of the unperturbed cavity and δh is the deflection of the membrane that supports the mirror.

Nevertheless, in spite of this mechanism can be implemented using fiber optics, this method is sophisticate in the design and in the construction because the devices require a sensor element that uses the small and thin plate supported by a corrugated membrane with special characteristics.

Finally, methods based on *electrophysical phenomena* are today more investigate and there is a lot of literature reliable. It is standing that for *electrophysical phenomena*, the changes of the physical and geometrical properties of a material due the electric field applied [14]. This phenomena is used for the measurement of voltage either in a spectroscopic way using the high Rydberg states [15] or by means the use of FOS taking the properties of the materials and passing light throw them. Using FOS for example, the fiber sometimes is used to sense dimensional changes of a piezoelectric material [16-32] or an electrostrictive material [33-37] in the presence of electromagnetic fields. Depending on the level of sensitivity required, the readout can be either by simple intensity measurement or by interferometric techniques [38,39]. Photoelectroluminescent phenomenon of some semiconductors is also take with fiber optics to carry out electric field measurements [40,41]. Using small bulk materials with electro-optic Pockels effect properties as $LiNbO_3$ [42-51], $Bi_4Ge_3O_{12}$ [52-56], $Bi_{12}GeO_{20}$ (BGO) [57,58], $Bi_{12}SiO_{20}$ (BSO) [59-62] and $Bi_{12}TiO_{20}$ (BTO) [63-67] or materials with

electro-optic Kerr effect properties [68,69], the light can be coupled with the fiber and modulated.

The conditions of designing a sensor involve among other factors, the easiness in the construction, the portability, the sensitivity and the independence with the variations of the environmental conditions [1]. Among the different techniques based on the electrophysical phenomena for the voltage measurement, the one that fulfils the approach of the construction easiness and portability are the sensors based on the electro-optic technique.

However, there are two obstacles that prevent the application of these sensors in industry. First, their sensitivity is somewhat low, and second the temperature stability of the entire sensor does not meet industrial requirements. In general, attention is paid to the temperature stability of crystal parameters [62, 70-76].

We have proposed to investigate the use of the BTO photorefractive crystal as electro-optic component in a voltage sensor due to the advantages that offers over other crystals used for the same purpose. The BTO photorefractive crystal has higher stability to the variations of the environmental temperature (compared with the $LiNbO_3$), has lower optical activity (compared with the BSO and BGO) and has higher electro-optic coefficient (compared with $Bi_4G_3O_{12}$) [77].

Therefore, the present dissertation is enclosed to demonstrate the use of the BTO crystal in an electro-optic voltage sensor for industrial applications, within several configurations, as well as in demonstrating the advantages that presents as much in sensitivity as in stability.

§1.3 Contributions

In the present dissertation, the theory of the electric field sensors based on the electrophysical phenomena as electro-optic effect is presented. Applications of BTO photorefractive crystal as electro-optic element are investigated in great detail and new configurations for voltage sensor are examined.

To demonstrate the feasibility for industrial applications of the remote voltage sensor based on a BTO crystal, the experiments were made and the results were registered and published in the following works:

1) **Role of Photoconductivity for operation of fiber optic electric field sensors: theory and experiments**. Here, the authors demonstrate theoretical and experimentally that the presence of the photoconductivity in a voltage sensor based on a BTO electro-optic crystal defines a non-uniform sensitivity region that must be to take into account for future designs of sensors based on photorefractive crystals type.

2) **Fiber optic optically controlled voltage sensor**. Here, the authors show the theory and the experiments for a new voltage sensor configuration that has optically controlled sensitivity.

3) **Fiber optic voltage and temperature sensor**. Here, the authors propose a configuration based on electro-optic modulator with a BTO crystal for voltage and temperature and it is demonstrated experimentally.

4) **An electro-optic fiber sensor with double pass configuration for measuring high AC voltage**. Here, the authors demonstrate the industrial application of a new configuration for an electro-optic fiber sensor for measuring two different waveforms of high AC voltage.

§1.4 Contents by chapter

Configurations of voltage sensor based on $Bi_{12}TiO_{20}$ crystal for industrial applications will be presented. In Chapter Two, fiber optic voltage sensor basis such as crystal optics, index ellipsoid, Jones matrix formalism and the amplitude modulation are considered.

In Chapter Three, the theory of electro-optic voltage sensors are presented. Materials for electro-optic voltage sensors and considerations such as the crystal dimensions and the photoconductivity effect for operation of fiber optic electric field sensors based on photorefractive crystals are considered. Moreover, several configurations reported up to now are described.

Chapter Four is devoted to a new configuration proposed for optically controlled voltage sensor. Where the control of the sensitivity made of the interaction of two widely separated wavelengths is demonstrated.

In Chapter Five, a fiber optic configuration for voltage and temperature measurements is proved by means of theory and experiments.

In Chapter Six, we show a new configuration for high AC voltage measurements for two available waveforms: continuos electric wave form and transient electric wave form.

Finally in Chapter Seven, general conclusions and ideas for further work are given.

References.

[1] J. M. López-Higuera, *Hanbook of Optical Fiber Sensing Technology*, 1st Ed. (John Wiley & Sons, LTD, London, 2002), Chaps.1 and 27

[2] A. J. Rogers, "Optical fibers in communications and measurement", *CEGB Research*, (BINITI No. **12**), 1984, pp. 3-17.

[3] G. A. Masey, D. C. Erickson and R. A. Kadlec, "Electromagnetic field Components: Their Measurement Using Linear Electrooptic and Magnetooptic Effects", *Appl. Opt*., vol. **14**, 2712-2719, (1975).

[4] B. Lee, "Review of the present status of optical fiber sensors", *Opt. Fiber Technol*., No **9**, 57-79, (2003).

[5] H. J. M. Hulshof, W. R. Rutgers, A.H. V.D. Wey, "Optical Voltage Sensors: Aplications in Electric Power Systems", *Proc. SPIE on Fiber Optic Sensors II*, vol. **798,** pp. 266-269, (1987).

[6] Thomas Bosselmann, "Magneto and Electrooptic Transformers meet espectations of Power Industry", *from the 12th International Conference on Optical Fiber Sensors, Opt. Soc. Am.*, vol. **16**, pp. 111-114, (1997).

[7] Allen H. Cherin, *An introduction to optical fibers*, (Mc Graw-Hill, New York, 1985) Chaps. 7-9.

[8] Frederick C. Allard, *Fiber Optics Handbook for Engineers and Scientists*, (Mc Graw-Hill, New York, 1989) Chap 4.

[9] Lucas J. R., *High Voltage Engineering*, revised edition, (Open University of Sri Lanka, 2001), Chap 6.

[10] A.Méndez, T. F. Morse, "Fiber Optic Electric Field Micro-Sensor", *Proc. SPIE on Fiber Optic and Laser Sensors X*, vol. **1795**, pp 153-164, (1992).

[11] T. S. Priest, G. B. Scelsi and G. A. Woolsey, "Optical fiber sensor for electric field and electric charge using low-coherence, Fabry-Perot interferometry", *Appl. Opt.*, vol. **36**, No. 19, pp. 4505-4508, (1997)

[12] P. Lorrain, D. Corson and F. Corson. *Electromagnetic Fields and Waves*,(W. H. Freeman and Company, New York, 1988) p. 110.

[13] Born M. and Wolf E., *Principles of Optics*, 7th Ed., (Pergamon Press, New York, 1984).

[14] Safa O. Kasap, *An illustrated dictionary of important terms and effects in optoelectronics an photonics*, first ed., (Mc Graw-Hill, Saskatchewan, Canada, 1999).

[15] Kee P. Koo and G. H. Sigel, "An Electric Field Sensor Utilizing a Piezoelectric Polyvinylidene Fluoride (PVF_2) Film in a Single-Mode Fiber Interferometer", *J. Quantum Electron.*, vol. **QE-18** No. 4, pp. 670-675, (1982).

[16] Pat D. De Souza and Marc D. Mermelstein, "Electric Field Detection with a Piezoelectric Polymer-Jacketed Single-Mode Optical Fiber", *Appl. Opt.*, vol. **21** No. 23, pp. 4214-4218, (1982).

[17] Marc D. Mermelstein, "Optical-Fiber Copolymer-Film Electric Field Sensor", *Appl. Opt.*, vol. **22**, No. 7, pp. 1006-1009, (1983).

[18] J. Jarzynski and R. P. De Paula, "Fiber Optic Electric Field Sensor Technology", *Proc. SPIE on Fiber Optic and Lasers Sensors IV*, vol. **718**, pp. 48-55, (1986).

[19] M. Imai, H. Tanizawa, Y. Ohtsuka, Y. Takase and A. Odajima, "Piezoelectric Copolymer Jacketed Single Mode Fibers for Electric Field Sensor Application", *J. Appl. Phys*., vol. **60**, No. 6, pp. 1916-1918, (1986).

[20] V. B. Baglikov, R. Yu. Dolinin, E. M. Zolotov, V. M. Pelekhatyi and R. F. Tavlykaev, "Investigation of an electric field sensor based on an integrated optical Mach-Zehnder modulator", *Sov. J. Quantum Electron*., vol. **18**, No. 10, pp. 1353-1355, (1988),

[21] Klaus M. Bohnert and J. Nehring, "Fiber Optic Sensig of Electric Field Components", *Appl. Opt*., vol. **27**, No.23, pp.4814-4818, (1988).

[22] Klaus M. Bohnert and J. Nehring, "Fiber-Optic Sensing of Voltages by Line Integration of the Electric Field", *Opt. Soc. Am*., vol. **14**, No. 5, pp. 290-292, (1989).

[23] N. Rajkumar, V.Jagadeesh Kumar and P. Sankaran, "Fiber sensor for the simultaneous measurement of current and voltage in a high-voltage system", *Appl. Opt*., vol. **32**, No. 7, pp. 1225-1228, (1993).

[24] Klaus M. Bohnert, H. Brändle and G. Frosio, "Field Test Interferometric Optical Fiber High Voltage and Current Sensors", *Proc. of SPIE on "Tenth Optical Fiber Sensors Conference"*, vol. **2360**, pp. 16-19, (1994).

[25] Bong Kyu Kim, Man Sik Kim and Byoung Yoon Kim, "Fiber-Optic Voltage Sensor", *Proc. of SPIE on "Optics for Science and New Technology"*, vol. **2778**, pp. 1139-1140, (1996).

[26] Yongkwan Lee, Ilryyong Kim and Soonchil Lee, "A nondisturbing electric-field sensor using piezoelectric and converse piezoelectric resonances", *Rev. of Sci. Inst*., vol. **68**, No 12, pp. 4427-4430, (1997).

[27] Klaus M. Bohnert and P. Pequignot, "Inherent Temperature Compensation of a Dual-Mode Fiber Voltage Sensor with Coherence-Tuned Interrogation", *J. Lightwave Technol*., vol. **16**, No. 4, pp. 598-604, (1998).

[28] Klaus M. Bohnert, Mathias Ingold and Jadran Kostovic, "Fiber-Optic Voltage Sensor for SF_6 insulated High-Voltage Switchgear", *Appl. Opt*., vol. **38**, No. 10, pp. 1926-1933, (1999).

[29] Mario Pacheco, Fernando Mendoza Santoyo, A. Méndez and Luis A. Zenteno, "Piezoelectric-Modulated Optical Fiber Bragg Grating High-Voltage Sensor", *Meas. Sci. Technol*., vol. **10**, pp. 777-782, (1999).

[30] Klaus M. Bohnert, Jadran Kostovic and Pascal Pequignot, “Fiber Optic Voltage Sensor for 420 kV electric power systems”, *Opt. Eng*, vol. **39**, No. 11, pp. 3060-3067, (2000).

[31] Hoseong Kim and Jinwoo Jun, “Fiber optic voltage sensor based on the photoelastic effect in a single-mode optical fiber”, *Opt. Eng*., vol. **39**, No. 12, pp. 3281-3284, (2000).

[32] Huang Yongling, Feng Dejung, Xu Zhaowen, Tong Zhengrong, Kai Guiyun and Dong Xiaoyi, “A voltage sensor utilizing all-fiber Mach-Zehnder interferometer”, *Proc. SPIE on “Fiber Optics and Optoelectronics for Network Applications”*, vol. **4603**, pp. 188-191, (2001).

[33] Sandeep T. Vohra, Frank Bucholtz and Alan D. Kersey, “Fiber Optic de and Low-Frequency Electric Field Sensor”, *Opt. Lett*., vol. **16**, No. 18, pp. 1445-1447, (1991)

[34] Sandeep T. Vohra and Frank Bucholtz, “Fiber Optic ac Electric Field Sensor Based on The Electrostrictive Effect”, *Opt. Lett.*, vol. **17**, No. 5, pp. 372-374, (1992).

[35] Larry Fabiny, Sandeep T. Vohra and Frank Bucholtz,, “High Resolution Fiber Optic Low Frequency Voltage Sensor Based on the Electrostrictive Effect”, *IEEE Photon. Technol. Lett*., vol. **5**, No.8, pp. 952-953, (1993).

[36] Larry Fabiny, Sandeep T. Vohra, Frank Bucholtz and Anthony D. Dandridge, “Three Channel Low-Frequency Fiber Optic Voltage Sensor”, *Opt. Soc. Am. (Opt. Lett.)*, vol. **19**, No. 3, pp. 228-230, (1994).

[37] Larry Fabiny, Sandeep T. Vohra and Frank Bucholtz, “Ultra Low Drift, Sub Microvolt Low Frequency Fiber Optic Voltage Sensor*”, Proc. SPIE on “Tenth Optical Fiber Sensors Conference”*, vol. **2360**, pp. 45-48, (1994).

[38] Thomas G. Giallorenzi, Joseph A. Bucaro, Anthony Dandridge, G.H.Siegel, James H. Cole, Scott C. Rashleifh and Richard G. Priest, “Optical Fiber Sensor Technology”, *IEEE J. Quantum Electron*., vol. **QE-18**, No. 4, pp. 626-665, (1982).

[39] Toshihico Yoshino, “Optical Fiber Sensors for Electric Industry”, *Proc. SPIE on Fiber Optic Sensors II*, vol. **798**, pp. 258-265, (1987).

[40] Tadeusz Pustelny, “Photoelectroluminescent Electric Field Intensity Sensor”, *Proc. SPIE*, vol. **2998**, pp. 348-353, (1997).

[41] Tadeusz Pustelny, B. Pustelny, “Electroluminiscent fiber optic sensor of electric field intensity”, *Proc. SPIE*, vol. **3054**, pp. 18-23, (1997).

[42] Catherine H. Bulmer, W. K. Burns and R. P. Moeller, "Linear Interferometric Waveguide Modulator for Electromagnetic-Field Detection", *Opt. Lett*., vol. **5**, No. 5, pp. 176-178, (1980).

[43] Kunhiko Hidaka and Hiroyuki Fujita, "A New Method of Electric Field Measurements in Corona Discharge Using Pockels Device", *J. Appl. Phys*., vol. **53** No. 9, pp. 5999-6003, (1982).

[44] Christian Duchet, "Integrated Electro-Optic Modulators With High Sensitivity For Remote Voltage Sensing", *Proc. SPIE on Fiber Optic Sensors*, vol. **586**, pp. 45-50, (1985).

[45] Christian Duchet, P. Fabre, M. DiMaggio, "Thermal Stability of $LiNbO_3$ Electro-Optic Waveguide Modulators for Remote Voltage Sensing", *Proc. SPIE on Fiber Optic and Laser Sensors V*, vol. **838**, pp. 39-43, (1987).

[46] Catherine H. Bulmer, "Sensitive, Highly Linear Litium Niobate Interferometers for Electromagnetic Field Sensing", *Appl. Phys. Lett*., vol. **53** No. 24, pp. 2368-2370, (1988).

[47] Sang Shin Lee, Min Chel Oh, Sang Yung Shing and Kwang Hee Keh, "Integrated Optical High Voltage Sensor Using a Z-Cut $LiNbO_3$ Cutoff Modulator", *IEEE Photon. Technol. Lett*., vol. **5**, No. 9, pp. 996-999, (1993).

[48] Nicolas A. F. Jaeger and Farnoosh Rahmatian, "Bias Integratred Optics Pockels Cell High-Voltage Sensors", *Proc. SPIE,* vol. **2072**, pp. 87-95, (1994).

[49] David H. Naghski, Joseph T. Boyd, Howard E. Jackson, S. Sriram Stuart A. Kingsley and J. Latess, "An Integrated Photonic Mach-Zehnder Interferometer with No Electrodes for Sensing Electric Fields", *J. Lightwave Technol*., vol. **12** No. 6, pp. 1092-1098, (1994)

[50] Yong-Sik Yim and Sang Yung Shin, "Lithium Niobate Integrated-Optic Voltage Sensor with Variable Sensing Ranges", *Opt. Soc. Am., from the 12th International Conference on Optical Fiber Sensors*, vol. **16**, pp. 108-110, (1997).

[51] Osamu Ogawa, Tomohiro Sowa and Shinichi Ichizono, "A Guided-Wave Optical Electric Field Sensor with Improved Temperature Stability", *J. Lightwave Technol.*, vol. **17**, No. 5, pp.823-830, (1999).

[52] H. J. M. Hulshof, W. R. Rutgers, A.H. v.d. Wey, "Optical Voltage Sensors: Aplications in Electric Power Systems", *SPIE on Fiber Optic Sensors II*, vol. **798,** pp. 266-269, (1987).

[53] Allen H. Rose and Gordon W. Day, "Optical fiber voltage sensors for broad temperature ranges", *Proc. SPIE*, vol. **1580**, pp. 95-103, (1992).

[54] Osamu Kamada and Kazuhiko Kakishita, "Electro-Optical Effect of $Bi_4Ge_3O_{12}$ Crystals for Optical Voltage Sensors", *Jpn. J. Appl. Phys*., vol. **32**, No. 9B, pp. 4288-4291, (1993).

[55] Josemir Coelho Santos, Muslum Cengiz Taplamacioglu and Kunhiko Hidaka "Optical High Voltage Measurement Using Pockels Microsingle Crystal", *Rev. Sci. Inst*., vol. **70**, No. 8, pp. 3271-3276, (1999).

[56] Xiaojun Zeng and Haiqing Chen, "Electro-optical measurement of highly intense electric field with high frequency", in Optical Sensing, Imaging and Manipulation for Biological and Biomedical Applications", *Proceedings of SPIE*, vol. **4082**, pp. 298-304, (2000).

[57] Kazuo Kyuma, Shuichi Tai, Masahiro Nunoshita, Noboru Mikami and Yoshiaki Ida, "Fiber-Optic current and voltage sensor using a $Bi_{12}GeO_{20}$ single crystal", *J. Lightwave Technol*., vol. **LT-1(1)**, pp. 93-97, (1983)

[58] Y. Koruda, Y. Abe, H. Kuwahara and K. Yoshinaga, "Field Test of Fiber-Optic Voltage and Current Sensors Applied to Gas Insulated Substation", *Proc. SPIE on Fiber Optic Sensors*, vol. **586**, pp. 30-37, (1985).

[59] Y. Kuhara, Y. Hamasaki, A. Kawakami, Y. Murakami, M. Tatsumi, H. Takimoto, K. Tada and T. Mitsui, "BSO/Fiber-Optic Voltmeter with Excellent Temperature Stability", *Electron. Lett.*, vol. **18**, No. 24, pp. 1055-1056, (1982).

[60] John P. Dakin and M. C. Holliday, "A Passive All Dielectric Field Probe for R.F. Measurement Using the Electro-Optic Effect", *Proc. SPIE on Fiber Optics '84*, vol. **468**, pp. 237-240, (1984).

[61] M. Norimatsu and M. Shirasaki, "$Bi_{12}SiO_{20}$ crystal application for voltage sensor in optical fibers", Ferroelectrics, vol. **75**, pp. 189-196, (1987).

[62] J. Niewisch, Peter Menke, P. Krammer, Thomas Bosselmann, "Temperature Drift Compensation of a Potential Transformer using a BSO Pockels Cell", *Eleventh*

International Conference on Optical Fiber Sensors, Jpn. Soc. Appl. Phys., vol.**WE 1-5**, pp. 152-155, (1996).

[63] Valery N. Filippov, Andrey N. Starodumov, Yuri O. Barmenkov and Vladim V. Makarov, "Fiber Optic Voltage Sensor Based on a $Bi_{12}TiO_{20}$ crystal", *Appl. Opt.*, vol. **39**, No. 9, pp. 1389-1393, (2000).

[64] Valery N. Filippov, Andrey N. Starodumov, Alexsander V. Kir'yanov, Yuri O. Barmenkov and Vladimir P. Minkovich, "Optical voltage sensing: The influence of photoconductivity on a sensor parameters", In applications of Optical Fiber Sensors, *Proceedings of SPIE*, vol. **4074**, pp. 412-418, (2000).

[65] Valery N. Filippov, Andrey N. Starodumov, Vladimir P. Minkovich and Francisco G. Peña Lecona, "Fiber Sensor for Simultaneous Measurement of Voltage and Temperature", *IEEE Photon. Technol. Lett.*, vol. **12**, No 11, pp. 1543-1545, (2000)

[66] Francisco G. Peña Lecona, Valery N. Filippov, Andrei N. Starodumov and Alexander V. Kir'yanov, "Fiber Optic Voltaje Sensor with Optically Controlled Sensitivity", *Opt. Comm.*, vol. **1**, No. 187, pp. 135-140, (2001).

[67] Francisco G. Peña Lecona, Juan Francisco Mosiño, Valery N. Filippov, René A. Martínez Celorio and Oracio C. Barbosa García, "An electro-optic fiber sensor with double pass configuration for measuring high AC voltage", *Meas. Sci. Technol*., to be published, (2004)

[68] G. R. Allen, H. P. Davis, B. T. Neyer, D. J. Muron and J. Chang, "Electro-Optical Kerr Effect Voltage Measurements On Multi-Megavolt Pulsed Power Acelerators", *SPIE on Fiber Optic and Laser Sensors III*, vol. **566**, pp. 223-226, (1985).

[69] Wang Zhaobing, Liao Yanbiao, Lai Shurong, Zhao Huafeng, "Fiber Sensor for Simultaneous Measurement of Current and Voltage by single Lo-Bi fiber", *Proc. SPIE*, vol. **2895**, pp. 26-32, (1996).

[70] Kyung Shik Lee and Gordon W. Day, "Effect of Multiple Internal Reflections on the Stability of Electrooptic and Magnetooptic Sensors", *Appl. Opt*., vol. **27** No. 22, pp. 4609-4611, (1988).

[71] Kyung Shik Lee, "New Compensation Method for Bulk Optical Sensors with Multiple Birefringences", *Appl. Opt.*, vol. **28**, No. 11, pp. 2001-2011, (1989).

[72] Kyung Shik Lee, “Electrooptic Voltage Sensors: Birrefringence Effects and Compensation Methods”, *Appl. Opt*., vol. **39**, No 30, pp. 4453-4461, (1990).

[73] Andreas Koch, Christian Helmig and Hartwig Senftleben, “Experimental Studies on a Temperature Compensation for Optical Voltage Sensing”, *12th International Conference on Optical Fiber Sensors*, pp.257-260, (1997)

[74] Klaus M. Bohnert and P. Pequignot, “Inherent Temperature Compensation of a Dual-Mode Fiber Voltage Sensor with Coherence-Tuned Interrogation”, *J. of Lightwave Technol*., vol. **16**, No. 4, pp. 598-604, (1998).

[75] Xiaoping Zheng and Yanbiao Liao, “A Technique for Fiber Optic Voltage Sensor to Realice Temperature Compensation”, *IEICE Trans. Electron Special Issue on Optical Fiber Sensors*, vol. **E83-C**, No. 3, pp.342-346, (2000).

[76] Hidenobu Hamada, “Investigation of the beam dependence of a fiber-optic voltage sensor by use of a $LiNbO_3$ crystal”, *J. Opt. Soc. Am. B*, vol. **18**, No. 4, pp. 444-456, (2001).

[77] S. I. Stepanov, “Applications of Photorefractive Crystals”, *Rep. Prog. Phys*., pp. 39-116, (1994).

Chapter Two:

Basis of fiber optic voltage sensors

§2.1 Introduction

A sensor system based on optical fiber and an electro-optic crystal can be treated as the application of a modulator of luminous intensity that uses the optical fiber as a guide of light and a crystal as an element that possesses an electrophysical property (either Pockels effect or Kerr effect). It is known that the electromagnetic characteristics and behavior of light that is propagating along the optical fiber are governed by Maxwell's equations.

Bulk and waveguide optical devices used as modulators, deflectors switches, sensors, etc., are constructed using isotropic, uniaxial or biaxial media. In active devices, isotropic and uniaxial media generally become biaxial via electro-optic effect and thus have three distinct principal indices of refraction (n_x, n_y, and n_z), the new principal dielectric axes may have some arbitrary orientation relative to the device reference coordinate system. Arbitrary orientations of the axes also occur in passive devices that have light propagating in a direction other than along a principal axis or in a principal plane of the crystal. Therefore, in designing and analyzing devices, it is necessary to understand the directional optical properties (polarization orientations, ray directions, phase velocity indices, ray velocity indices, etc.) of crystals and the effect of birefringence level on these properties.

The present chapter explains the fundamental concepts related to the electric field sensors based on the electro-optic effect. Related to these concepts we have the crystal optics, in which we will study the index ellipsoid as application to the analysis of the light propagation in crystals media. Together with the Jones matrix formalism and the amplitude modulation, we will extend our study in the following Chapter to electric field sensors, the materials used for it and the different configurations.

§2.2 Crystal optics and the index ellipsoid

A crystal is a three-dimensional periodic arrangement of atoms, molecules or ions. A characteristic property of the crystal structure is its periodicity and a degree of symmetry. For each atom the number of neighbors and their exact orientations are well defined, otherwise the periodicity will be lost. If the molecules are organized in space according to regular periodic patterns and are oriented in the same direction, the medium is in general anisotropic [1].

For any anisotropic (optically inactive) crystal class there are two allowed orthogonal linearly polarized waves propagating with different phase velocities for a given wave vector $\boldsymbol{k}$. Biaxial crystals represent the general case of anisotropy. Generally, the allowed waves exhibit *extraordinary-like* behavior, that is, the wave vector $\boldsymbol{k}$ and Poynting vector $\boldsymbol{S}$ directions differ. In addition, the phase velocity, polarization orientation and Poynting vector of each wave change distinctly with wave vector direction and the two waves have different directional characteristics. For each allowed wave, the electric field $\boldsymbol{E}$ is not parallel to the displacement vector $\boldsymbol{D}$ (which defines polarization orientation) and therefore the ray (Poynting) vector $\boldsymbol{S}$ is not parallel to the wave vector $\boldsymbol{k}$. Figure 2.1 depicts the geometrical relationship of these vectors for two *extraordinary-like* waves, also showing that $\boldsymbol{D}$ is perpendicular to $\boldsymbol{k}$ and that $\boldsymbol{E}$ is perpendicular to $\boldsymbol{S}$. Only for propagation in the (x,y) and (y,z) principal planes of a biaxial crystal will one of the waves exhibit *ordinary-like* behavior, that is, its optical properties are independent of direction within these planes. As shown in Figure 2.1 the angle α between $\boldsymbol{D}$ and $\boldsymbol{E}$ is the same as the angle between $\boldsymbol{k}$ and $\boldsymbol{S}$, but for a given $\boldsymbol{k}$, $\alpha_1 \neq \alpha_2$. Furthermore, for each wave $\boldsymbol{D}\perp\boldsymbol{k}\perp\boldsymbol{H}$ and $\boldsymbol{E}\perp\boldsymbol{S}\perp\boldsymbol{H}$ (where $\perp$ reads perpendicular), forming orthogonal sets of vectors. The vectors $\boldsymbol{D}$, $\boldsymbol{E}$, $\boldsymbol{K}$ and $\boldsymbol{S}$ are coplanar for each wave [2]. An important conclusion is that, in general, the energy in an anisotropic crystal does not propagate parallel to the wave normal direction, except when propagation is along a principal axis. Also, for any direction of phase propagation there are two phase velocities, corresponding to two allowed monochromatic plane waves with differing directions of linear polarization ($\boldsymbol{D}$).

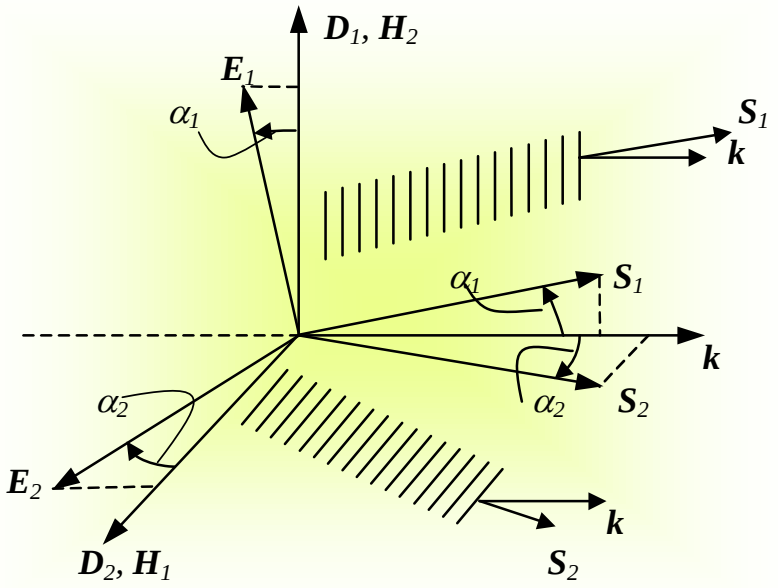

Figure 2.1 The geometric relationships of the electric quantities ***D*** and ***E*** and the magnetic quantities ***B*** and ***H*** to the wave vector ***k*** and the ray vector ***S*** are shown for the two allowed extraordinary-like waves propagating in an anisotropic medium [3].

The propagation characteristics of the two allowed orthogonal waves are directly related to the fact that the optical properties of an anisotropic material depend on direction. These properties are represented by the constitutive relation $\boldsymbol{D}=\bar{\varepsilon}\,\boldsymbol{E}$, where $\bar{\varepsilon}$ is the relative permittivity tensor of the medium and ***E*** is the corresponding optical electric field vector. For a homogeneous, nonmagnetic, loss less, optically inactive and non-conducting medium, the relative permittivity tensor has only real components. Moreover, the relative permittivity tensor and its inverse $\bar{\varepsilon}^{-1}=1/\varepsilon_0\left(1/n^2\right)$, where n is the refractive index, are symmetric for all crystal classes and for any orientation of the dielectric axes [3-5]. On the other hand, the relative permittivity tensor is useful in the study of the directional optical properties of crystals with the wavevector surface. The unit vectors $\hat{x},\hat{y},\hat{z}$ identify the principal dielectric axes of the crystal. The principal relative permittivities ε_x, ε_y, and ε_z correspond to the permittivities for polarization oriented along $\hat{x}$, $\hat{y}$ and $\hat{z}$, respectively. A device reference coordinate system with axes $\hat{x}_r$, $\hat{y}_r$ and $\hat{z}_r$ that can have any arbitrary orientation with respect to $\hat{x}$, $\hat{y}$ and $\hat{z}$ is defined for displaying the resulting optical properties.

The permittivity tensor $\bar{\varepsilon}$ is represented by a matrix that is real, nonsingular, positive definite and symmetric. Therefore, all three eigenvalues (principal relative permittivities ε_x, ε_y, and ε_z) are positive, all three eigenvectors (principal axes $\hat{x}, \hat{y}, \hat{z}$) are real and orthogonal and the determinant of $\bar{\varepsilon}$ is strictly positive. Therefore, the matrix representation of the permittivity tensor can be diagonalized, and in principal coordinates, the constitutive equation has the form:

$$\begin{pmatrix} D_x \\ D_y \\ D_z \end{pmatrix} = \begin{pmatrix} \varepsilon_x & 0 & 0 \\ 0 & \varepsilon_y & 0 \\ 0 & 0 & \varepsilon_z \end{pmatrix} \begin{pmatrix} E_x \\ E_y \\ E_z \end{pmatrix} \tag{2.1}$$

where reduced subscript for the permittivity tensor notation is used. The principal permittivities lie on the diagonal of $\bar{\varepsilon}$ and the principal refractive indices are $n_x = \sqrt{\varepsilon_x}$, $n_y = \sqrt{\varepsilon_y}$ and $n_z = \sqrt{\varepsilon_z}$. The symmetry of $\bar{\varepsilon}$ guarantees that its diagonal form exists as in Equation 2.1, given a correct choice of three perpendicular principal axes oriented in a specific manner with respect to the crystallographic axes.

Therefore, the index ellipsoid is a construct with geometric characteristics representing the phase velocities and the vibration directions of $\boldsymbol{D}$ of the two allowed plane waves corresponding to a given optical wave-normal direction $\boldsymbol{k}$ in a crystal. The material properties (principal permittivities or refractive indices) of the crystal at optical frequencies must be known to develop this construct. This index ellipsoid can represent a quadratic surface of the stored electric energy density ω_e of a dielectric [5].

$$\omega_e = \tfrac{1}{2}\, \boldsymbol{E} \cdot \boldsymbol{D} = \tfrac{1}{2} \sum_i \sum_j E_i \varepsilon_{ij} E_j = \tfrac{1}{2}\, \varepsilon_0\, \boldsymbol{E}^T \bar{\varepsilon}\, \boldsymbol{E} \qquad i,j = x,y,z \tag{2.2}$$

or

$$\omega_e = \tfrac{1}{2}\, \varepsilon_0\, (E^2_x \varepsilon_x + E^2_y \varepsilon_y + E^2_z \varepsilon_z) \tag{2.3}$$

in principal coordinates. Here *T* indicates transpose. The stored energy density is positive for any value of electric field and thus it has positive eigenvalues (permittivities). Therefore, the quadratic surface is always given by an ellipsoid [3, 6].

With the Equation (2.1), Equation (2.3) assumes the form:

$$\left(\frac{D_x^2}{\varepsilon_x}\right) + \left(\frac{D_y^2}{\varepsilon_y}\right) + \left(\frac{D_z^2}{\varepsilon_z}\right) = 2\omega_e\varepsilon_0. \tag{2.4}$$

By substituting $x = \dfrac{D_x}{\sqrt{2\omega_e\varepsilon_0}}$ and $n_x^2 = \varepsilon_x$, and similarly for y and z, the ellipsoid is expressed in Cartesian principal coordinates as:

$$\frac{x^2}{n_x^2} + \frac{y^2}{n_y^2} + \frac{z^2}{n_z^2} = 1 \tag{2.5}$$

Equation (2.5) is the general index ellipsoid for an optically biaxial crystal. If $n_x = n_y$, the surface becomes an ellipsoid of revolution, representing a uniaxial crystal. In this crystal, one of the two allowed eigenpolarizations will always be an ordinary wave with its Poynting vector parallel to the wave vector and ***E*** parallel to ***D*** for any direction of propagation. An isotropic crystal ($n_x = n_y = n_z$) is represented by a sphere with the principal axes having equal length. Any wave propagating in this crystal will exhibit ordinary characteristics. The index ellipsoid for each of these three optical symmetries is shown in Figure 2.2.

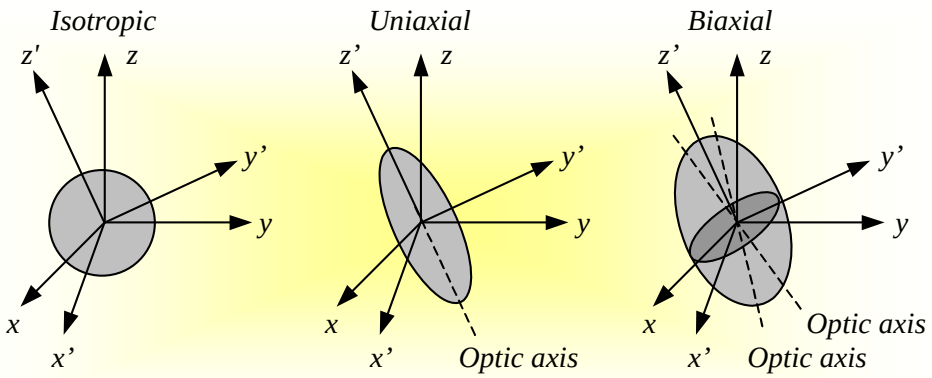

Figure 2.2 The index ellipsoid for the three crystal symmetries are shown in nonprincipal coordinates (x', y', z') relative to the principal coordinates (x, y, z). For isotropic crystals, the surface is a sphere. For uniaxial crystals, it is an ellipsoid of revolution. For biaxial crystals it is a general ellipsoid [7].

For a general direction of propagation, the section of the ellipsoid through the origin perpendicular to this direction is an ellipse, as shown in Figure 2.3a. The major and minor axes of the ellipse represent the orthogonal vibration directions of $\boldsymbol{D}$ (eigenpolarizations) for that particular direction of propagation. The lengths of these axes correspond to the principal refractive indices and therefore give the respective phase velocities of the allowed polarizations. They are therefore, referred to as the fast and the slow axes. Figure 2.3b illustrates the field relationships with respect to the index ellipsoid. The line in the ($\boldsymbol{k}$,$\boldsymbol{D}_i$) plane (i=1 or 2) that is tangent to the ellipsoid at $\boldsymbol{D}_i$ is parallel to the ray vector $\boldsymbol{S}_i$. The line length denoted by n_{si} gives the ray velocity as $v_{si} = \boldsymbol{C}/n_{si}$ for $\boldsymbol{S}_i$. The same relationships hold for vibration, $\boldsymbol{D}_1$ or $\boldsymbol{D}_2$.

In the general ellipsoid for a biaxial crystal there are two cross sections passing through the center that are a circle. The normals to these cross sections are called the optic axes (denoted in Figure 2.2 in a non-principal coordinate system), and they are coplanar and symmetric about the z principal axis in the x,z plane. The angle ϑ of an optic axis with respect to the z-axis in the x, z plane is

$$\tan\vartheta = \frac{n_z}{n_x}\sqrt{\frac{n_y^2 - n_x^2}{n_z^2 - n_y^2}} \tag{2.6}$$

The phase velocities for $\boldsymbol{D}_1$ and $\boldsymbol{D}_2$ are equal for these two directions: $v_1 = v_2 = c/n_y$. In an ellipsoid of revolution for a uniaxial crystal there is one circular cross section perpendicular to the z principal axis. Therefore, the z-axis is the optic axis, and $\vartheta = 0^\circ$ in this case.

Several surfaces exist which may be used to represent the various optical properties of crystals. For example, in many cases the index ellipsoid, shown in Figure 2.3, is useful for device analysis [7]. Given a direction of phase propagation $\boldsymbol{k}$, the two-phase velocity indices of refraction (n_1 and n_2), the corresponding eigenpolarizations ($\boldsymbol{D}_1$, $\boldsymbol{D}_2$), ray velocity indices (n_{S1}, n_{S2}) and ray directions ($\boldsymbol{S}_1$, $\boldsymbol{S}_2$) are readily determined from the index ellipsoid. The three distinct principal indices of refraction for natural biaxial crystals are ordered in magnitudes as $n_z > n_y > n_x$, and they identify the three semiaxis lengths (principal axes) of the biaxial ellipsoid. For propagation directions not coinciding with these axes, the phase velocity index for one wave (n_1) will always lie between n_x and n_y and for the other wave (n_2) between n_y and n_z. These intermediate indices are the lengths of the semiaxis of the cross-sectional ellipse perpendicular to $\boldsymbol{k}$.

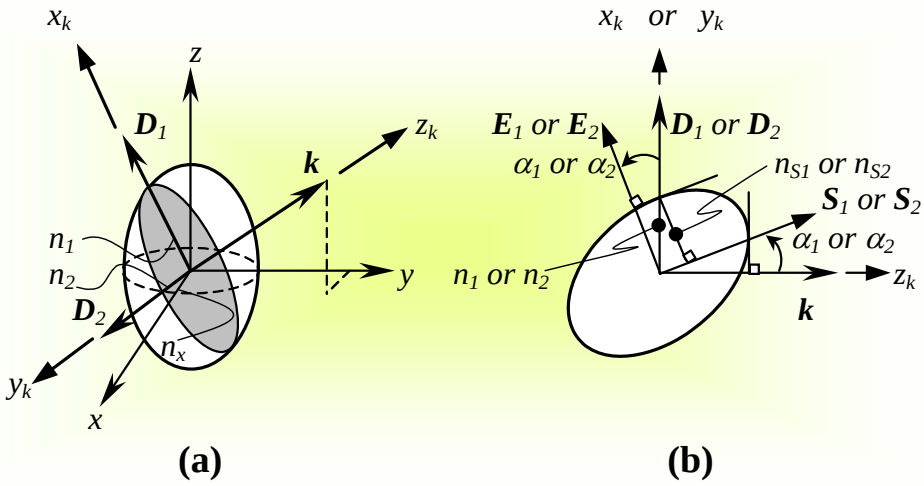

Figure 2.3 (a) The index ellipsoid cross section that is normal to the wave vector $\boldsymbol{k}$ has the shape of an ellipse. The major and minor axes of this ellipse represent the directions of the allowed polarizations $\boldsymbol{D}_1$ and $\boldsymbol{D}_2$; (b) for each eigenpolarization (1 or 2) the vectors $\boldsymbol{D}$, $\boldsymbol{E}$, $\boldsymbol{S}$ and $\boldsymbol{k}$ are coplanar [7].

The two sheeted wave-vector surface, on the other hand, is useful for examining, in wave-vector space, the directional characteristics of light propagating in crystals [3-5]. The sheets of the surface depict the dispersive nature of the phase velocity indices for the two

allowed linearly orthogonally polarized waves as the direction of propagation changes. For isotropic crystals, the wave-vector surface is a sphere, since both indices are the same and are independent of direction. For uniaxial crystals, the sheets consist of two quadratic surfaces, a sphere and an ellipsoid of revolution, one inside the other and intersecting at two points along the optic axis; one index is constant with direction (sphere) and the other has directional dependence (ellipsoid of revolution). For biaxial crystals, however, the wave-vector surface is more complicated; each sheet is a higher-order surface, one inside the other and intersecting at only four points that lie in the (*x*, *z*) principal plane. These points identify the orientations of the two optic axes in the (*x*, *z*) principal plane, which is referred as the optic plane.

§2.3 The electro-optic effect in cubic crystals

The *electro-optic effect* is the change in the refractive index resulting from the application of a dc or low-frequency electric field. A field applied to an anisotropic electro-optic material modifies its refractive indices and thereby its effect on polarized light.

The dependence of the refractive index on the applied electric field takes one of two forms:

- The refractive index changes in proportion to the applied electric field, in which case the effect is known as *the linear electro-optic effect* or the *Pockels effect*.
- The refractive index changes in proportion to the square of the applied electric field, in which case the effect is known as the *quadratic electro-optic effect* or the *Kerr effect*.

The basic idea behind electro-optic devices is to alter the optical properties of a material with an applied voltage in a controlled way. The changes in the optical properties, particularly the permittivity tensor, translate into a modification of some parameters of a light

wave carrier, such as phase, amplitude, frequency, polarization or position, as it propagates through the device.

At an atomic level, an electric field applied to certain crystals causes a redistribution of bond charges and possibly a slight deformation of the crystal lattice [5]. In general, these alterations are not isotropic; that is, the changes vary with the direction in the crystal. Therefore, the inverse dielectric constant (impermeability) tensor changes accordingly. Crystals lacking a center of symmetry are noncentrosymmetric and exhibit a linear (Pockels) electro-optic effect. The changes in the impermeability tensor elements are linear in the applied electric field. On the other hand, all crystals exhibit a quadratic (Kerr) electro-optic effect. The changes in the impermeability tensor elements are quadratic in the applied field. When the linear effect is present, it generally dominates over the quadratic effect.

The linear electro-optic effect is represented by a third rank tensor $\mathbf{r}_{ijk}$. The permutation symmetry of this tensor is $\mathbf{r}_{ijk} = \mathbf{r}_{jik}$, i, j, k = 1,2,3. Therefore the tensor can be represented by a 6×3 matrix; i.e., $\mathbf{r}_{ijk} \Rightarrow \mathbf{r}_{ij}$, i=1,...,6 and j=1,2,3. Generally, the $\mathbf{r}_{ij}$ coefficients have very little dispersion in the optical transparent region of a crystal. The quadratic electro-optic effect is represented by a fourth rank tensor $\mathbf{s}_{ijkl}$. The permutation symmetry of this tensor is $\mathbf{s}_{ijkl} = \mathbf{s}_{jikl} = \mathbf{s}_{ijlk}$, $i, j, k, l = 1,2,3$. The tensor can be represented by a 6×6 matrix; i.e., $\mathbf{s}_{ijkl} \Rightarrow \mathbf{s}_{kl}$, $k, l = 1,...,6$.

2.3.1 The linear electro-optic effect or Pockels effect

An electric field applied in a general direction to a non-centrosymmetric crystal produces a linear change in the constants $(1/n^2)_i$ due to the linear electro-optic effect according to

$$\Delta(1/n^2)_i = \sum_j r_{ij} E_j \qquad i= 1,...6 \; ; \; j=x,y,z = 1, 2, 3 \tag{2.7}$$

where r_{ij} is the *ij*th element of the linear electro-optic tensor in contracted notation. In matrix form Equation (2.7) is

$$\begin{pmatrix} \Delta(1/n^2)_1 \\ \Delta(1/n^2)_2 \\ \Delta(1/n^2)_3 \\ \Delta(1/n^2)_4 \\ \Delta(1/n^2)_5 \\ \Delta(1/n^2)_6 \end{pmatrix} = \begin{pmatrix} r_{11} & r_{12} & r_{13} \\ r_{21} & r_{22} & r_{23} \\ r_{31} & r_{32} & r_{33} \\ r_{41} & r_{42} & r_{43} \\ r_{51} & r_{52} & r_{53} \\ r_{61} & r_{62} & r_{63} \end{pmatrix} \begin{pmatrix} E_x \\ E_y \\ E_z \end{pmatrix} \tag{2.8}$$

E_x, E_y, and E_z are the components of the applied electric field in principal coordinates. The magnitude of $\Delta(1/n^2)_i$ is typically on the order of less than 10^{-5}. Therefore, these changes are mathematically referred to as perturbations. The new impermeability tensor $\overline{1/n^2}'$ in the presence of an applied electric field is no longer diagonal in the reference principal dielectric axes system. It is given by

$$\overline{1/n^2}' = \begin{pmatrix} 1/n_x^2 + \Delta(1/n^2)_1 & \Delta(1/n^2)_6 & \Delta(1/n^2)_5 \\ \Delta(1/n^2)_6 & 1/n_y^2 + \Delta(1/n^2)_2 & \Delta(1/n^2)_4 \\ \Delta(1/n^2)_5 & \Delta(1/n^2)_4 & 1/n_z^2 + \Delta(1/n^2)_3 \end{pmatrix} \tag{2.9}$$

However, the field-induced perturbations are symmetric, so the symmetry of the tensor is not disturbed. The new index ellipsoid is now represented by

$$(1/n^2)'_1 x^2 + (1/n^2)'_2 y^2 + (1/n^2)'_3 z^2 + 2(1/n^2)'_4 y z + 2(1/n^2)'_5 x z + 2(1/n^2)'_6 x y = 1 \tag{2.10}$$

or equivalently, $\boldsymbol{X}^T \overline{1/n^2}' \boldsymbol{X} = 1$, where $\boldsymbol{X} = [x\ y\ z]^T$ [6, 8]. The presence of cross terms indicates that the ellipsoid is rotated and the lengths of the principal dielectric axes are changed. Determining the new orientation and shape of the ellipsoid requires that $\overline{1/\boldsymbol{n}^2}'$ be

diagonalized, thus determining its eigenvalues and eigenvectors. The perturbed ellipsoid will then be represented by a square sum:

$$\frac{x'^2}{n_{x'}^2}+\frac{y'^2}{n_{y'}^2}+\frac{z'^2}{n_{z'}^2}=1 \tag{2.11}$$

The eigenvalues of $\overline{1/n^2}'$ are $1/n^2_{x'}$, $1/n^2_{y'}$, $1/n^2_{z'}$. The corresponding eigenvectors are $\boldsymbol{x}'=[x_{x'}, y_{x'}, z_{x'}]^T$, $\boldsymbol{y}'=[x_{y'}, y_{y'}, z_{y'}]^T$ and $\boldsymbol{z}'=[x_{z'}, y_{z'}, z_{z'}]^T$, respectively.

2.3.2 The quadratic electro-optic effect or Kerr effect

An electric field applied in a general direction to any crystal, centrosymmetric or noncentrosymmetric, produces a quadratic change in the constants $(1/n^2)_i$ due to the quadratic electro-optic effect according to

$$\begin{pmatrix}\Delta(1/n^2)_1\\ \Delta(1/n^2)_2\\ \Delta(1/n^2)_3\\ \Delta(1/n^2)_4\\ \Delta(1/n^2)_5\\ \Delta(1/n^2)_6\end{pmatrix}=\begin{pmatrix}S_{11} & S_{12} & S_{13} & S_{14} & S_{15} & S_{16}\\ S_{21} & S_{22} & S_{23} & S_{24} & S_{25} & S_{26}\\ S_{31} & S_{32} & S_{33} & S_{34} & S_{35} & S_{36}\\ S_{41} & S_{42} & S_{43} & S_{44} & S_{45} & S_{46}\\ S_{51} & S_{52} & S_{53} & S_{54} & S_{55} & S_{56}\\ S_{61} & S_{62} & S_{63} & S_{64} & S_{65} & S_{66}\end{pmatrix}\begin{pmatrix}E_x^2\\ E_y^2\\ E_z^2\\ E_xE_y\\ E_xE_z\\ E_xE_y\end{pmatrix} \tag{2.12}$$

E_x, E_y, and E_z are the components of the applied electric field in principal coordinates. The perturbed impermeability tensor and the new index ellipsoid have the same form as Equations (2.9) and (2.10).

2.3.3 Mathematical approaches

A number of formalisms are suggested in the literature to address the specific problem of finding the new set of principal dielectric axes relative to the zero-field principal dielectric axes. Most approaches, nevertheless, do not provide a consistent means of labeling the new axes. Also, some methods are highly susceptible to numerical instabilities when dealing with very small off-diagonal elements as in the case of the linear electrooptic effect.

The usual approach is to obtain the eigenvalues λ of the impermeability tensor by solving the cubic secular equation, $|[1/n^2] - \lambda[I]| = 0$, where |*| denotes determinant and $[I]$ is the identity matrix. These solutions are then substituted one at time into the eigenvalues equation to determine the corresponding eigenvectors [9]. This method has the disadvantages of being numerically unstable and arbitrary in determining the eigenvectors.

A second approach is the method of successive approximations that is based on the radius-normal property of an ellipse [9]. This iterative process produces radials vectors that eventually converge to the major axis of the ellipse corresponding to greatest value. Some difficulties with this method include the following: (1) the inverse of the impermeability matrix must be found to determine the smallest principal value; (2) each eigenvector must be accurately determined before calculating the next one; (3) the third eigenvector is found by the cross product of the two eigenvectors. Thus the orthogonality property of eigenvectors is the basis of this method and hence, this property cannot be used as a check on the principal axes obtained.

A third approach, the Richardson purification process for eigenvectors, has the advantage of calculating the eigenvectors independently of one another, so the orthogonality property can be used as a check. However, there must be some prior knowledge of the eigenvalues in order to use this method, since it uses approximations of these values to find the corresponding eigenvectors.

A fourth approach, the method of Lagrange multipliers, has been suggested as a method for finding the allowed vibration directions $\boldsymbol{D}$ for a given direction of phase propagation [3]. The procedure utilizes the following facts: (1) $\boldsymbol{D} \cdot \boldsymbol{k} = 0$, (2) $\omega_e = \frac{1}{2} \boldsymbol{E} \cdot \boldsymbol{D}$ and (3) the principal axes of an ellipse are the shortest an the longest radial distances, the extreme

of $r^2 = x^2 + y^2 + z^2$ are found subject to these conditions. This formalism requires the solution of a secular equation, therefore, has the limitations noted previously.

A fifth approach is a geometric method using the Mohr circle. It was used originally in the analysis of stress and strain tensors. This method has also been suggested for general second-rank tensors describing the physical properties of crystals [9]. The zero-field principal dielectric axes of the tensor are transformed to another set of axes (closer to the principal dielectric axes) by a simple rotation about one of the zero-field axes. The principal values are found by the use of a circle construction in the rotation plane. These values are extracted from points on the circle. In practice this method is used primarily to develop the approximate formulas for relating the components in the zero-field frame of reference to those in the transformed axes and to determine how rapidly a specific element of a tensor changes as a function of rotation angle. However, this method is difficult to apply to tensors with repeated principal values or with small off-diagonal elements.

In contrast to these methods, has been proposed an attractive approach for diagonalizing a symmetric matrix for the purpose of determining its eigenvalues and eigenvectors [10, 11]. This method is suggested in the literature for electrooptic effect calculations but is introduced only for very simple cases [12]. A symmetric matrix $[A]$ can be reduced to a diagonal form by the transformation $[a][A][a]^T = [\lambda]$, where $[\lambda]$ is a 3×3 diagonal matrix and $[a]$ is the transformation matrix. Since the eigenvalues of $[A]$ are preserved under similarity transformation, they lie on the diagonal of $[\lambda]$. This approach is always possible for symmetric matrices regardless of the multiplicity of the eigenvalues. The transformation matrix $[a]$ is real and orthogonal ($[a]^T = [a]^{-1}$) and, therefore, non-singular. Thus the columns of $[a]^T$ (or rows of $[a]$) are independent, and they represent the right eigenvectors (or left eigenvectors for $[a]$) of the corresponding eigenvalues of the matrix. The ordering of the eigenvalues and corresponding eigenvectors is apparent if the transformation is expressed as an eigenvalues equation, $[A][a]^T = [a]^T[\lambda]$. The first column of $[a]^T$ corresponds to the eigenvector whose eigenvalues is the firth diagonal element of $[\lambda]$ and similarly for the other two columns. In the event of repeated eigenvalues, the associated eigenvectors are arbitrary and span a characteristic plane, yet a set of orthogonal eigenvectors is obtained.

The problem of determining the new principal axes and the indices of refraction of the index ellipsoid in the presence of an external electric field is analogous to the problem of finding the transformation matrix *[a]* that will diagonalize the perturbed impermeability tensor. The lengths of the semiaxes are the reciprocals of the square roots of the eigenvalues of $\overline{1/n^2}'$. Generally, this matrix reduction requires a sequence of similarity transformations. Since similarity is a transitive property, several transformation matrices can be multiplied to generate the desired cumulative matrix [7].

There are a number of numerical techniques that perform the similarity transformation for the eigensystem problem of symmetric matrices, including the Givens rotation method, Householder's method, QR algorithm and Jacobi method. The first three approaches have the advantages of speed and accuracy of determining the eigenvalues, but they are tedious and sometimes unreliable in the calculation of accurate eigenvectors, especially for repeated or nearly equal eigenvalues. Small perturbations in the elements of $[1/n^2]$ necessarily give rise to small perturbations in the eigenvalues and nearly equal eigenvalues may lead to the inaccurate determination of the associated eigenvectors

The Jacobi method is a form of similarity transformation that has been shown to provide both accurate eigenvalues and orthogonal eigenvectors. On the other hand, the Jacobi method is the only approach of the four that can provide both accurate eigenvalues and orthogonal eigenvectors and furthermore, it is the simplest to execute. Moreover, it produces reliable results for matrices with very small off-diagonal elements [10].

§2.4 Jones Matrix formalism

In an electro-optic modulator, a beam of polarized light is propagated through a succession of optical devices, each of that produces a specific change in the state of polarization that can be easily modeled with the aid of the Jones calculus.

The Jones calculus was invented in 1941 by Robert Clark Jones and is a powerful method in which the state of polarization of the input luminous wave is represented by a two-

component vector while each optical element is represented by a 2 × 2 matrix. The overall matrix for the whole system is obtained by multiplying all the matrices, and the state of polarization of the transmitted light is computed by multiplying the vector representing the input beam by the overall matrix [13].

The Jones vector representation of a light beam contains information not only the state of polarization but also the intensity of light. Its electric vector can be written as Jones vector:

$$\mathbf{E} = \begin{pmatrix} E_x \\ E_y \end{pmatrix} \tag{2.13}$$

And the intensity is given by:

$$I = \mathbf{E}^{\dagger} \cdot \mathbf{E} = |E_x|^2 + |E_y|^2 \tag{2.14}$$

where the symbol (†) signifies the Hermitian conjugate. The Jones vector of the emerging beam after it passes through all the optical elements is written as:

$$\mathbf{E'} = \begin{pmatrix} E_x \\ E_y \end{pmatrix} \tag{2.15}$$

In many cases, we need to determine the transmission function of the optical system. For this case, the ratio of the output intensity to the input intensity in an optical system is defined as the transmission function (or simply *transmission*) and it is given by:

$$T = \frac{I_0}{I_i} = \frac{\left|E_x'\right|^2 + \left|E_y'\right|^2}{\left|E_x\right|^2 + \left|E_y\right|^2} \tag{2.16}$$

An electro-optic crystal, which forms the voltage sensitive element in a Pockels' cell, can be approximate to an elliptic retarder (with an optical activity ρ) and a voltage induced linear birefringence Γ. Its Jones Matrix is given by [14]:

$$\mathbf{M}(\Gamma,\rho)=\begin{bmatrix} \cos\frac{\delta}{2}+i\frac{\Gamma}{2}\frac{\sin\frac{\delta}{2}}{\frac{\delta}{2}} & -\rho\frac{\sin\frac{\delta}{2}}{\frac{\delta}{2}} \\ \rho\frac{\sin\frac{\delta}{2}}{\frac{\delta}{2}} & \cos\frac{\delta}{2}-i\frac{\delta}{2}\frac{\sin\frac{\delta}{2}}{\frac{\delta}{2}} \end{bmatrix} \tag{2.17}$$

where:

$\delta=\sqrt{\Gamma^2+(2\rho)^2}$ is the elliptical birefringence

ρ is the optical activity

Γ is the induced linear birefringence

To describe the complete Pockels cell we need the Jones matrices of the remaining optical components. They are given as follows:

1) Quarter wave plate with linear birefringence Γ: $\mathbf{Q}(\Gamma)=\begin{bmatrix} e^{-i\frac{\Gamma}{2}} & 0 \\ 0 & e^{i\frac{\Gamma}{2}} \end{bmatrix}$

2) Polarizer at azimuth θ: $\mathbf{P}(\theta)=\begin{bmatrix} \cos^2\theta & \sin\theta\cos\theta \\ \sin\theta\cos\theta & \sin^2\theta \end{bmatrix}$

3) Input polarization at azimuth η: $\mathbf{J}(\eta)=\begin{bmatrix} \cos\eta \\ \sin\eta \end{bmatrix}$

The coordinate system of the matrices **M** and **Q** is aligned with the eigenaxes of their birefringence. To allow an arbitrary orientation a coordinate transformation using a rotational matrix **R** is necessary, where the orientation of the crystal is γ and the one of the wave plate is φ:

4) Rotational matrix at any angle ψ: $$\mathbf{R}(\psi) = \begin{bmatrix} \cos\psi & \sin\psi \\ -\sin\psi & \cos\psi \end{bmatrix}$$

Therefore, to obtain the intensity of the output beam in a Pockels cell, we have to multiply the matrices above exposed as shows:

$$I_0 = |\mathbf{A}(\theta)\ \mathbf{R}(\gamma)\ \mathbf{M}(\Gamma,\rho)\ \mathbf{R}(-\gamma)\ \mathbf{R}(\varphi)\ \mathbf{Q}(\Gamma)\ \mathbf{R}(-\varphi)\ \mathbf{J}(\eta)\ |^2 \qquad (2.18)$$

§2.5 Amplitude Modulation

An electro-optic modulator can be classified as one of two types, *longitudinal* or *transverse*, depending how the voltage is applied relative to the direction of light propagation in the device. A bulk modulator consists of an electro-optic crystal sandwiched between a pair of electrodes and, therefore, can be modeled as a capacitor. In general, the input and output faces are parallel for the beam to undergo a uniform phase shift over the beam cross section [5].

In the longitudinal configuration, the voltage is applied parallel to the wave vector direction as shown in Figure 2.4a [1, 5, 15 and 16]. The electrodes must be transparent to the light by the choice of material used either for them (metal-oxide coatings of SnO, InO or CdO) or by leaving a small aperture at their center at each end of the electro-optic crystal [1 and 15]. The ratio of the crystal length L to the electrode separation b is defined as the *aspect ratio*. For this configuration $L=b$ and therefore the aspect ratio is always unity. The magnitude of the applied electric field inside the crystal is $E=V/L$. The induced phase shift is proportional to V and the wavelength λ of the light but not the physical dimensions of the device. Therefore for longitudinal modulators, changing the aspect ratio cannot reduce the required magnitude of the applied electric field for a desired degree of modulation. Moreover, the degree of modulation

increases with wavelength. However, these modulators can have a large acceptance area and are useful if the light beam has a large cross-sectional area.

In the transverse configuration, the voltage is applied perpendicular to the direction of light propagation as shown in Figure 2.4b [1, 5, 15 and 16]. The electrodes do not obstruct the light as it passes through the crystal. For this case, the aspect ratio can be very large. The magnitude of the applied electric field is $E=V/d$ (where the electrode separation b is equal to d), and d can be reduced to increase E for a given applied voltage, thereby increasing the aspect ratio L/b. The induced phase shift is inversely proportional to the aspect ratio; therefore, the voltage necessary to achieve a desired degree of modulation can be greatly reduced. Furthermore, the interaction length can be long for a given field strength. Nevertheless, the transverse dimension d is limited by the increase in capacitance, which affects the modulation bandwidth or the speed of the device and by diffraction for a given length L, since a beam with finite cross section diverges as it propagates [5, 15].

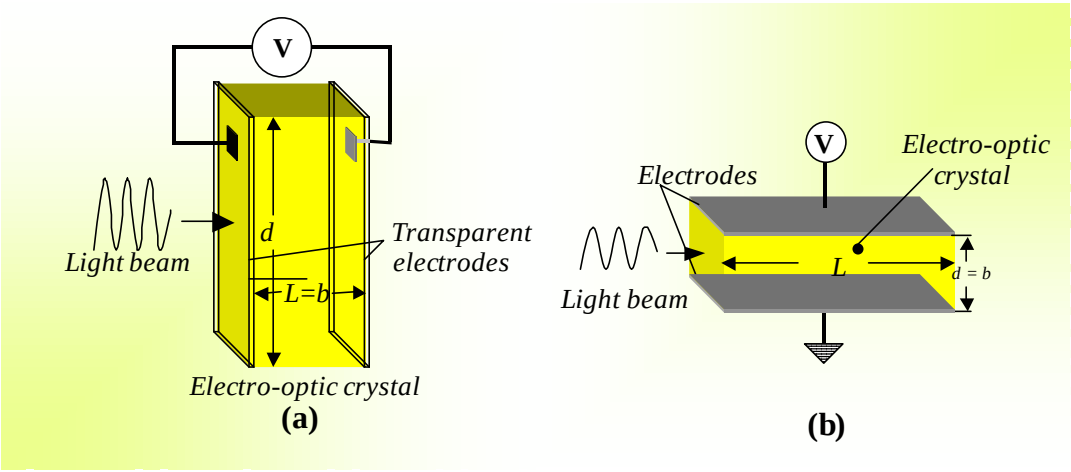

Figure 2.4 (a) A longitudinal electro-optic modulator has the voltage applied parallel to the direction of light propagation and the length L is equal to the electrodes' separation b; (b) a transverse modulator has the voltage applied perpendicular to the direction of light propagation and the width d is equal to the electrodes' separation b [5].

The modulation of amplitude can be implemented using an electro-optic bulk modulator with polarizers and passive birefringent elements. Three assumptions are made:

1) The modulating field is uniform throughout the length of the crystal; the change in index or birefringence is uniform unless otherwise stated.
2) The modulation voltage is dc or very low frequency ($\omega_m << 2\pi/\tau$); the light experiences the same induced Δn during its transit time τ through the crystal of length L, and the capacitance is negligible.
3) Light propagation is taken to be along a principal axis, before and after the voltage is applied; therefore, the equations are presented in terms of the optical electric field $\boldsymbol{E}$, rather than the displacement vector $\boldsymbol{D}$, which is common practice in various optical references. For other general configurations the equations should be expressed in terms of the eigenpolarizations $\boldsymbol{D_1}$ and $\boldsymbol{D_2}$**.** However, the electric field will determine the direction of energy flow.

An example of a longitudinal device is shown in Figure 2.5. In general, an applied voltage V will rotate the principal axes in the crystal cross-section. For amplitude modulation, Figure 2.5 indicates a polarizer along x with an input optical electric field $E_o(t) = E_i \cos \omega t$.

For intensity (optical energy) modulation of a light wave, some possibilities include using:

- A dynamic retarder configuration with a crossed polarizer at the output
- A dynamic retarder configuration with a parallel polarizer at the output
- A phase modulator configuration in a branch of a Mach-Zehnder interferometer
- A dynamic retarder with push-pull electrodes.

The intensity modulator parameter of interest is the *transmission* $T=I_0/I_i$, as we mentioned before, is the ratio of output to input intensity.

As the two polarizations propagate at different speeds through the crystal, a phase difference (relative phase) or retardation Γ evolves between them as a function of length:

$$\Gamma = \frac{2\pi}{\lambda}(n_{x'} - n_{y'})L = \frac{2\pi}{\lambda}(n_x - n_y)L - \frac{\pi}{\lambda}(r_x n_x^3 - r_y n_y^3)EL = \Gamma_0 - \Gamma_i \qquad (2.19)$$

where Γ_0 is the natural phase retardation in the absence of an applied voltage and Γ_i is the induced retardation linearly related to V.

For a longitudinal modulator, the applied electric field is $E = V/L$, and the induced retardation is:

$$\Gamma_i = \left(\frac{\pi}{\lambda}\right)\left(r_y n_y^3 - r_x n_x^3\right)V \tag{2.20}$$

which is independent of L and linearly related to V.

For a transverse modulator $E = V/d$ and the induced retardation is:

$$\Gamma_i = \left(\frac{\pi}{\lambda}\right)\left(r_y n_y^3 - r_x n_x^3\right)\frac{L}{d} \tag{2.21}$$

The optical fields at the output can be expressed in terms of Γ:

$$E_{x'} = \cos\ \omega t$$
$$E_{y'} = \cos\ (\omega t - \Gamma)$$

Therefore, the desired output polarization is obtained by applying the appropriate voltage magnitude. The eigenpolarizations $E_{x'}$ and $E_{y'}$ are in phase at $z = 0$. They have the same frequency but different wavelengths. Light from one polarization gradually couples into the other. In the absence of natural birefringence, $n_x - n_y = 0$, the voltage that would produce a retardation of $\Gamma = \Gamma_i = \pi$, such that a vertical polarization input becomes a horizontal polarization output, is known as the *half – wave voltage* V_π and it is given by:

$$V_\pi = \frac{\lambda}{r_x n_x^3 - r_y n_y^3} \quad \text{for longitudinal modulator}$$

$$V_\pi = \frac{\lambda}{r_x n_x^3 - r_y n_y^3}\left(\frac{d}{L}\right) \quad \text{for transversal modulator} \qquad (2.22)$$

The total retardation in terms of V_π (assuming no birefringence) is

$$\Gamma = \Gamma_0 + \pi\left(\frac{V}{V_\pi}\right) \qquad (2.23)$$

To cancel the effect of natural birefringence, the phase retardation Γ_0 can be made a multiple of 2π by slightly polishing the crystal to adjust the length or by applying a bias voltage. If birefringence is present, an effective V_π can be calculated that would give a total retardation of $\Gamma = \pi$.

An intensity modulator constructed using a dynamic retarder with crossed polarizers is shown in Figure 2.5.

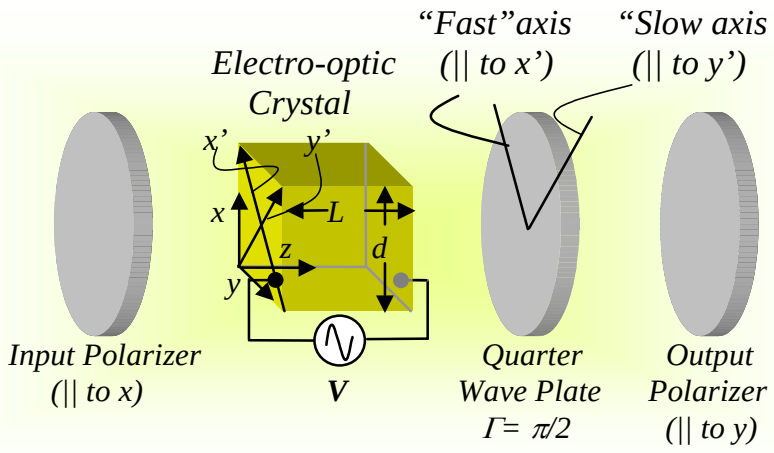

Figure 2.5 A longitudinal intensity modulator is shown using crossed polarizers with the input polarization along the x principal axis [5].

The *transmission* for this modulator is

$$T(V) = \sin^2\left(\frac{\Gamma}{2}\right) = \sin^2\left(\frac{\Gamma_0}{2} + \frac{\pi V}{2V_\pi}\right) \tag{2.24}$$

using (2.14). For linear modulation, where the output is a replica of the modulating voltage signal, a fixed bias of $\Gamma_0 = \pi / 2$ must be introduced either by placing an additional phase retarder, a $\lambda / 4$ wave plate (Fig 2.5), at the output of the electro-optic crystal or by applying an additional dc voltage of $V_\pi / 2$ (Fig. 2.6). This bias produces a transmission of $T=0.5$ in the absence of modulating voltage. If the crystal cross section has natural birefringence, then a variable compensator (Babinet-Soleil) or a voltage less than $V_\pi / 2$ must be used to tune the birefringence to give a fixed retardation of $\pi/2$.

For a sinusoidal modulation voltage $V=V_m sin\ \varpi_m t$, the retardation at the output of the crystal, including the bias, is

$$\Gamma = \Gamma_0 + \Gamma_i = \frac{\pi}{2} + \Gamma_m \sin \omega_m t \tag{2.25}$$

where $\Gamma_m = \pi V_m / V_\pi$ is the amplitude modulation index or depth-of-amplitude modulation

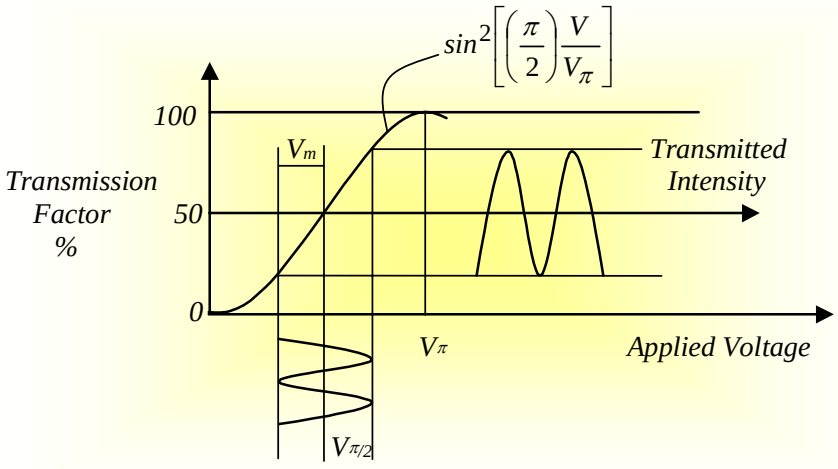

Figure 2.6 A λ/4 wave plate is used as a bias to produce linear modulation [5].

The *transmission* becomes

$$T(V) = \sin^2\left(\frac{\pi}{4} + \frac{\Gamma_m}{2}\sin\omega_m t\right) = \frac{1}{2}\left[1 - \cos\left(\frac{\pi}{2} + \Gamma_m \sin\omega_m t\right)\right] \tag{2.26}$$

If the modulation voltage is small *($V_m << 1$)*, then the modulation depth is small *($\Gamma_m << 1$)* and

$$T(V) = \frac{1}{2}\left[1 + \Gamma_m \sin\omega_m t\right] \tag{2.27}$$

Therefore, the *transmission* or output intensity is nearly related to the modulating voltage. If the signal is large, then the output intensity becomes distorted, and higher-order odd harmonics appear [5].

The dynamic retarder with parallel polarizers has a *transmission* of [5]:

$$T = \cos^2\left(\frac{\Gamma}{2}\right) = \cos^2\left(\frac{\pi}{4} + \frac{\Gamma_m}{2}\sin\omega_m t\right) = \frac{1}{2}\left[1 + \cos\left(\frac{\pi}{2} + \Gamma_m \sin\omega_m t\right)\right] \tag{2.28}$$

For small modulation, *$T(V) = (1/2)[1-\Gamma_m \sin \omega_m t]$*, and again, the output is a replica of the modulating voltage.

Similarly, the output of a Mach-Zehnder interferometer is given by

$$I_0 = I_1 + I_2 = \frac{1}{2}\left[I_i \cos\Gamma_0 + I_i\right] = I_i \cos^2\left(\frac{\Gamma_0}{2}\right) \tag{2.29}$$

where Γ_0 is the relative phase shift between the two branches. An intensity modulator is produced by placing a phase modulator in one branch [1] as shown in Figure 2.7.

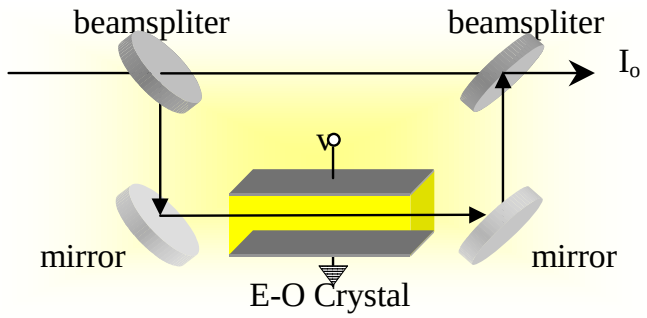

Figure 2.7 An intensity modulator is shown implementing a Mach-Zehnder interferometer configuration with a phase modulator in one branch [1].

The total retardation is $\Gamma = \Gamma_0 + \Gamma_i$, as before. The *transmission* is

$$T = \frac{I_0}{I_i} = \cos^2\left(\frac{\Gamma}{2}\right) \tag{2.30}$$

The push-pull modulator is based on the Mach-Zehnder interferometer. In this case, a phase modulator is placed in each branch with opposite polarity voltages applied to the arms; the phase modulators are driven 180^0 out of phase. This configuration requires lower drive voltages and provides a shorter transit time for the light for a defined degree of modulation [17, 18].

References

[1] Bahaa E. A. Saleh and Melvin Carl Teich, *Fundamentals of Phtonics*, 1st Ed. (Wiley, New York, 1991), chapter 18.

[2] Maldonado T. A. and Gaylord T. K., "Light Propagation Characteristics for Arbitrary Wavevector Directions in Biaxial Crystals by a Coordinate-free Approach", *Appl. Opt.*, vol. **30**, No. 18, 20, 2465-2480, (1991).

[3] Max Born and Emil Wolf, *Principles of Optics*, 6th ed., Pergamon Press, Oxford, UK, 1980.

[4] L. D. Landau y E. M. Lifshitz, *Electrodinámica de los medios contínuos*, ed. Reverté.

[5] Amnon Yariv and P. Yeh, *Optical Waves in Crystals*, 1st Ed., (John Wiley & Sons, New York, 1984), Chaps. 1-8.

[6] Ivan P. Kaminow, *An Introduction to Electrooptic Devices*, (Academic Press, New York, 1974), pp. 40-53.

[7] T. A. Maldonado and Thomas Gaylord, "Electro-Optic Effect Calculations: Simplified Procedure for Arbitrary Cases", *Appl. Opt.*, vol. **27,** No. 24, pp. 5051-5066, (1988).

[8] Amnon Yariv, *Optical Electronics*, (Holt Rinehart and Winston, New York, 1976).

[9] J. F. Nye, *Physical Properties of Crystals*, (Oxford Science Publications, London, 1985).

[10] Gene H. Golub, Charles F. Van Loan, *Matrix Computations*, (The Johns Hopkins University Press, 1990).

[11] William H. Press, Brian P. Flannery, Saul A. Teukolsky and William T. Vetterling, *Numerical Recipes*, (Cambridge University Press, 1986).

[12] Frederic A. Hopf and George I. A. Stegeman, *Applied Classical Electrodynamics*, (Volume 1: Linear Optics, 1985).

[13] R. C. Jones, "A new calculus for the treatment of optical systems", *J. Opt. Soc. Am.*., vol. **31**, 488-493, (1941).

[14] W. J. Tabor and F. S. Chen, "Electromagnetic propagation through materials possessing both Faraday rotation and birefringence: experiments with Ytterbium Orthoferrite", *J. Appl Phys.*, vol. **40**, No. 7, pp. 2760-2765, (1969).

[15] A. Ghatak and K Thyagarajan, *Optical Electronics*, (Springer-Verlag, New York, 1990), Chapter 4.

[16] E. Hecht, *Optics*, (Addison Wesley, 1990).

[17] W. H. Steier, "A Push-Pull Optical Amplitude Modulator", *IEEE J. Quantum Electron.*, vol. **QE-3**, No. 12, 664-667, (1967).

[18] Allen H. Rose and Gordon W. Day, "Optical fiber voltage sensors for broad temperature ranges", Proc. SPIE vol. **1580**, pp. 95-103, (1992).

Chapter Three:

Optical Voltage Sensors

§3.1 Introduction

The measurement of DC and extra low frequency (up to 60 Hz) electric fields is essential within the process industry, to assess the health hazard and electromagnetic compatibility of electronic devices. The conventional measurement systems used at present are based on active, metallic and bulky probes which disturb the measured field [1]. In addition, interpretation of the results using the traditional techniques is often complex.

The optical measurement of electrical voltage is more advantageous than other methods from the viewpoints of safety and influence on measured objects. One such method is to use an electro-optic crystal that exhibits the Pockels effect. We have seen in the previous section that an electro-optic crystal has induced birefringence with magnitude proportional to the applied electric field. This effect is used to measure electric fields in terms of the optical power and there are two varieties of these measurements: the longitudinal type and the transversal type. In the longitudinal type, the propagation directions of the ray and the electric field in the crystal are the same; in the transversal type, they are orthogonal.

Pockels electro-optic effect application to sensing electric field was demonstrated long time ago [2]. From then on, other authors have proposed several configurations for electric field sensor based on the Pockels effect. The electric field optical probe utilizing linear electro-optic effect can be manufactured in such a way that it is all dielectric, passive and immune to electromagnetic interference. It also enables direct measurement of the electric field intensity.

In this Section, we will demonstrate that the sensor sensitivity to electric fields is one of the most important characteristics and can be influenced by geometry and the photoconductivity of the crystal.

At extra low frequencies the conductivity of the materials must be considered as it can quench the electro-optic effect and thus cause malfunction of the sensor. Also, we will extend our study to the voltage sensors based on the electrophysical phenomena reported up to now in the literature, considering properties such as the temperature dependence and the response against the voltage presence.

§3.2 Materials for electro-optic voltage sensors

Many types of materials have been proposed for voltage sensors. However, our discussion is restricted here to those materials with electro-optic properties that have been reported in sensors of bulky type. Finally, we will make a comparative study among these sensors concerning in their dimensions.

3.2.1 Pockels effect materials for voltage sensors

Cubic crystals are the most appropriate for sensors applications. They do not possess natural birefringence and pyroelectricity. Crystals, which are birefringent and pyroelectric, may exhibit temperature instabilities and are highly sensitive to the optical alignment. Among the cubic crystals, only those with 23 and $\bar{4}3m$ crystallographic point group symmetry exhibit linear electro-optic effect.

The matrix of electro-optic coefficients for these crystals are given by

$$\begin{pmatrix} 0 & 0 & 0 \\ 0 & 0 & 0 \\ 0 & 0 & 0 \\ r_{41} & 0 & 0 \\ 0 & r_{41} & 0 \\ 0 & 0 & r_{41} \end{pmatrix} \tag{3.1}$$

for both crystal groups.

Using matrix (3.1) and Equation (2.10), the index ellipsoid in the presence of the electric field is [3]

$$\frac{x^2 + y^2 + z^2}{n^2} + 2r_{41}\left(yzE_x + zxE_y + xyE_z\right) = 1 \tag{3.2}$$

In the cubic crystal system, the crystallographic point group $\bar{4}3\mathrm{m}$ is the only point group with a Pockels effect that does not have inherent optical activity. Crystals in this group are GaAs, CdTe, ZnS, ZnSe, GaP and $Bi_4Ge_3O_{12}$ [3-5]. Bismuth germanate's most common use is as scintillation material.

In the $\bar{4}3\mathrm{m}$ point group the crystal orientation that gives the largest induced linear retardance is obtained when the electric field is normal to the (110) crystal plane and the optical path is normal to the $(\bar{1}10)$ plane (Figure 3.1) [3].

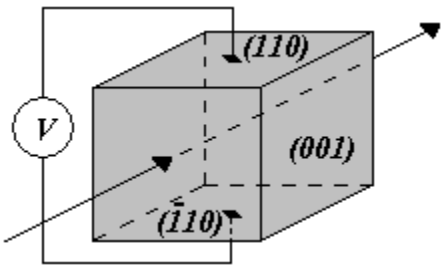

Figure 3.1 Orientation that gives the largest induced linear retardance for $\bar{4}3\mathrm{m}$ point group.

The other optical paths through the crystal, normal to the (110) and (001) planes will remain isotropic in the electric field [3]. The axes of the induced birefringence in the crystal will be 45° to the normal of the (110) plane [3]. The magnitude of the induced linear birefringence Γ is:

$$\Gamma = \frac{2\pi}{\lambda}\frac{l}{d}n_0^3 r_{41} V \tag{3.3}$$

where λ is the optical wavelength in air, l is the length of the optical path through the crystal, d is the distance between electrodes, V is the applied voltage, n_0 is the refractive index and r_{41} is the electro-optic coefficient [3].

The value of the product $n_0^3\ r_{41}$ for $Bi_4Ge_3O_{12}$ has only small wavelength dependence and is approximately 8.8 pm/V [4]. The r_{41} coefficient is linear up to a field of at least 20 kV/cm [4]. The normalized temperature dependence of $n_0^3\ r_{41}$ is $(1.54 \pm 0.16) \times 10^{-4}$ / ^{o}C [4]. The voltage necessary for 0.174 rad of retardance, is about 600 V for a $Bi_4Ge_3O_{12}$ crystal $5 \times 5 \times 20$ mm and $\lambda = 780$ nm.

Another point group in the cubic crystal system used for voltage and electric field sensing is the 23 point group. The 23 point group has no inherent linear birefringence, but does have optical activity [3]. Useful crystals in this group are $Bi_{12}GeO_{20}$ (BGO), $Bi_{12}SiO_{20}$ (BSO) and $Bi_{12}TiO_{20}$ [3]. The temperature dependence of the optical activity can be used to compensate for the temperature dependence of the Pockels effect in the crystal [6].

Equation (3.3) also applies to the 23 point group for transverse orientations. For BSO at 780 nm the product $n_0^3 r_{41}$ is about 82 pm/V and the optical activity ρ/l is about 200 mrad/mm [6,7]. The normalized temperature dependence of $n_0^3 r_{41}$ in BSO is about -3.19×10^{-4} / ^{o}C. The normalized temperature dependence of the optical activity is about -2.33×10^{-4} / ^{o}C [6,7].

For BTO at 780 nm the product $n_0^3 r_{41}$ is about 87 pm/V and the optical activity ρ/l is about 30 mrad/mm [8, 9]. The temperature dependence of these coefficients has not been reported.

Lithium niobate $LiNbO_3$ is a material used extensively in integrated-optic electro-optic modulators, usually in a Mach-Zehnder interferometer configuration. Waveguides can be made in $LiNbO_3$ by in-diffusing titanium at temperatures above 1000 ^oC [10]. $LiNbO_3$ is in the trigonal system, 3 m point group, which has natural linear birefringence [3]. Typically in $LiNbO_3$ voltage sensors the crystal is cut so that the optical path is on the *z*-axis and the electric field is parallel to the *y*-axis. This is done so the optical path is not affected by $LiNbO_3$'s natural birefringence; however, the crystal must be cut precisely so that no linear birefringence accumulates along the optical path. The voltage-induced retardance is

$$\Gamma = \frac{2\pi}{\lambda}\frac{l}{d}n_0^3 r_{22} V \tag{3.4}$$

with $n_0^3 r_{22}$ is about 38 pm/V, with a normalized temperature dependence of about 1.3×10^{-5} / ^oC [10]

3.2.2 Kerr effect materials for voltage sensors

The electro-optic Kerr effect is an electric field-induced linear birefringence that occurs in all materials. The electric field alters the polarizability of the material, creating a linear birefringence proportional to the field squared.

The electro-optic Kerr effect has been used for many years to measure high voltages and electric fields [11-13]. Most applications are with liquids that have a large temperature dependence, due to the nonlinear polarizability of the molecules in the liquid or glass and require the proximity of electrodes [11]. In fibers, the electro-optic Kerr effect has been used for voltage sensing and modulating the polarization state [14, 15]. Nevertheless, because of the temperature dependence of the electro-optic Kerr effect in fibers and the difficulty of making a stable sensor with low stress sensitivity its use have been discouraged [15]. The retardance due to the electro-optic Kerr effect has the functional form:

$$\Gamma = 2\pi L \beta_K E^2 \tag{3.5}$$

where β_K is the electro-optic Kerr constant and E is the electric field strength . For silica β_K is equal to 5.3 ($\pm$ 0.2) $\times$ 10^{-16} m/V at 23 ^{o}C [15]. The temperature dependence of β_K for silica, is 5.6 ($\pm$ 0.2) $\times$ 10^{-3} / ^{o}C [15].

§3.3 Crystal dimensions and photoconductivity considerations for operation of bulky-type voltage sensors

A schematic diagram of the electric field sensor based on the electro-optic effect is shown in Figure 3.2. Light from a monochromatic source (a laser diode for example) is polarized using a polarizer. Then it is launched into the electro-optic crystal in such a way that it excites two propagation modes. The two eigenmodes are linearly polarized waves with the plane of polarization perpendicular to each other. They propagate with different phase velocities depending on the electric field intensity. Thus the polarization of the light emerging from the crystal is changed proportionally to the applied electric field. This change is then converted by the polarizing beamsplitter into a change in the light intensity and detected by two photodetectors. The quarter-wave plate inserted between the polarizer and the crystal produces an additional phase shift between the eigenmodes, so the sensor works well within the linear region of its transfer characteristic.

With the assumption that the optical components are ideal and the crystal does not exhibit natural birefringence (there is no phase shift between the eigenwaves without electric field). Then, light intensities I_1 and I_2 at the photodetectors are [16]

$$I_1 = I_0\left(1 + \sin\left(\Gamma\right)\right) \tag{3.6}$$

$$I_1 = I_0\left(1-\sin\left(\Gamma\right)\right) \tag{3.7}$$

where I_0 is the light intensity at the photodetectors without the measured electric field and Γ is the relative phase retardation induced by the electric field.

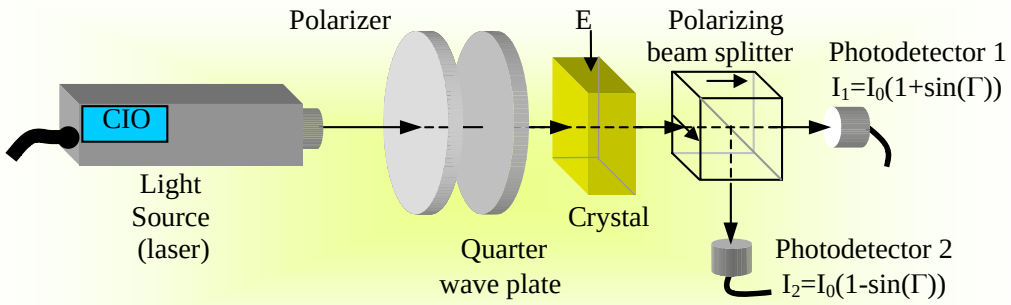

Figure 3.2 A schematic diagram of the electric field sensor based on linear electro-optic (Pockel's) effect and polarimetric optical scheme.

The phase shift Γ is directly proportional to the measured electric field and for transversal and longitudinal modulation, can be expressed as

$$\Gamma = \frac{2\pi}{\lambda} n^3 r_{41} E_m L \tag{3.8}$$

where λ is the wavelength of the light, n the refractive index, r_{41} the electro-optic coefficient, L is the length of the crystal transversed by the light and E_m is the macroscopic electric field intensity inside the crystal. In contrast to electro-optic modulators the internal electric field is no longer uniform as the crystal is exposed to an electric field without electrodes.

For small Γ, which is usually the case, the output can be considered as a linear function of the intensity of the electric field E. It is apparent that the sensor can be operational with only one of the outputs. In practice, however, both outputs are used to increase sensor sensitivity and to reduce the laser power fluctuation noise employing a suitable detection scheme (e.g. $(I_1-I_2) / (I_1+I_2)$).

Before comparing numerical values of the material's constants more used for voltage sensors, it is useful to express applied electric field E in terms of a field E_m that would exist in the absence of the sensor crystal or does exist at a considerable distance from the crystal. Because the fields induced in a cylindrical or rectangular crystal have complicated spatial variations, we can make the simplifying approximation that the crystal shape resembles an ellipsoid of revolution about the optical propagation direction which we have chosen parallel to z and make use of the depolarization factors that have been calculated for ellipsoids from static electric and magnetic field theory [16, 17]. From such an approximate calculation we can obtain for the field components along the *ith* semimajor ellipsoid axis:

$$\frac{E_{mi}}{E_{io}} = \frac{D_i^{-1}}{1 + \varepsilon_{ri} - D_i^{-1}} \tag{3.9}$$

where E_{io} is the ith external field component, and ε_{ri} is the relative permittivity for the internal field component E_i,

The depolarization factors for ellipsoids of revolution about the $i = z$ axis are [16, 17]:

$$\left.\begin{aligned} D_1 = D_2 &= \tfrac{1}{2} a\left(a^2 - 1\right)^{-1}\left\{a - \tfrac{1}{2}\left(a^2 - 1\right)^{-1/2} \ln\left[\frac{a + \left(a^2 - 1\right)^{1/2}}{a - \left(a^2 - 1\right)^{1/2}}\right]\right\} \\ D_3 &= \left(a^2 - 1\right)^{-1}\left\{\tfrac{1}{2} a\left(a^2 - 1\right)^{-1/2} \ln\left[\frac{a + \left(a^2 - 1\right)^{1/2}}{a - \left(a^2 - 1\right)^{1/2}}\right] - 1\right\} \end{aligned}\right\} \tag{3.10}$$

where a is the length/width ratio as shown in Figure 3.3.

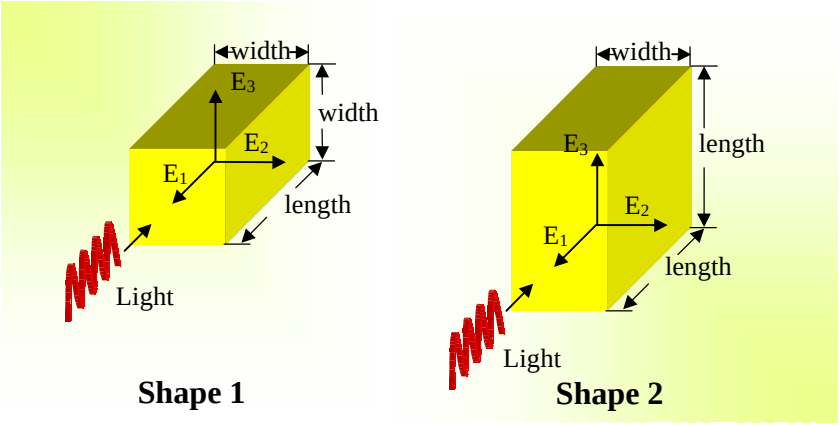

Figure 3.3 Shapes of the electro-optic crystals.

3.3.1 Dimensions considerations

The effect of the crystal shape on the sensor sensitivity is demonstrated in Figure 3.4. Two crystal shapes for both perpendicular and longitudinal electro-optic effects are examined. The shape 1 of Figure 3.3, where two dimensions denoted with *width* are the same, was substituted by an ellipsoid of revolution with its major axis along the direction of E_1 and major to minor axes ratio equal to *length/width* ratio. The quantity $1/(1+\varepsilon_{ri}D_i-D_i)$, expressing the attenuation of the external field, is calculated for different ratios for the crystals $Bi_4Ge_3O_{12}$, BGO, BSO and BTO and plotted in Figure 3.4. Also, the figure 3.4 shows that for a longitudinal modulator, $Bi_4Ge_3O_{12}$ has the slope of K value bigger than the other crystals compared. The graph shows that in a prolonged crystal (length/width > 1) the transverse field (E_2, E_3) is attenuated more than the longitudinal field (E_1). For example with the length width ratio of 2.5, the attenuation of the transverse field is more than a twice higher compared to the attenuation of the longitudinal field. Thus when designing the sensor using the longitudinal effect, crystal shape should be similar to shape 1 with the length width ratio as high as possible to maximize sensor sensitivity. Nevertheless, the shape 1 is not the best choice for the transverse electro-optic effect. One can argue that the same attenuation of the transverse external field can be achieved with the ratio less than 1.

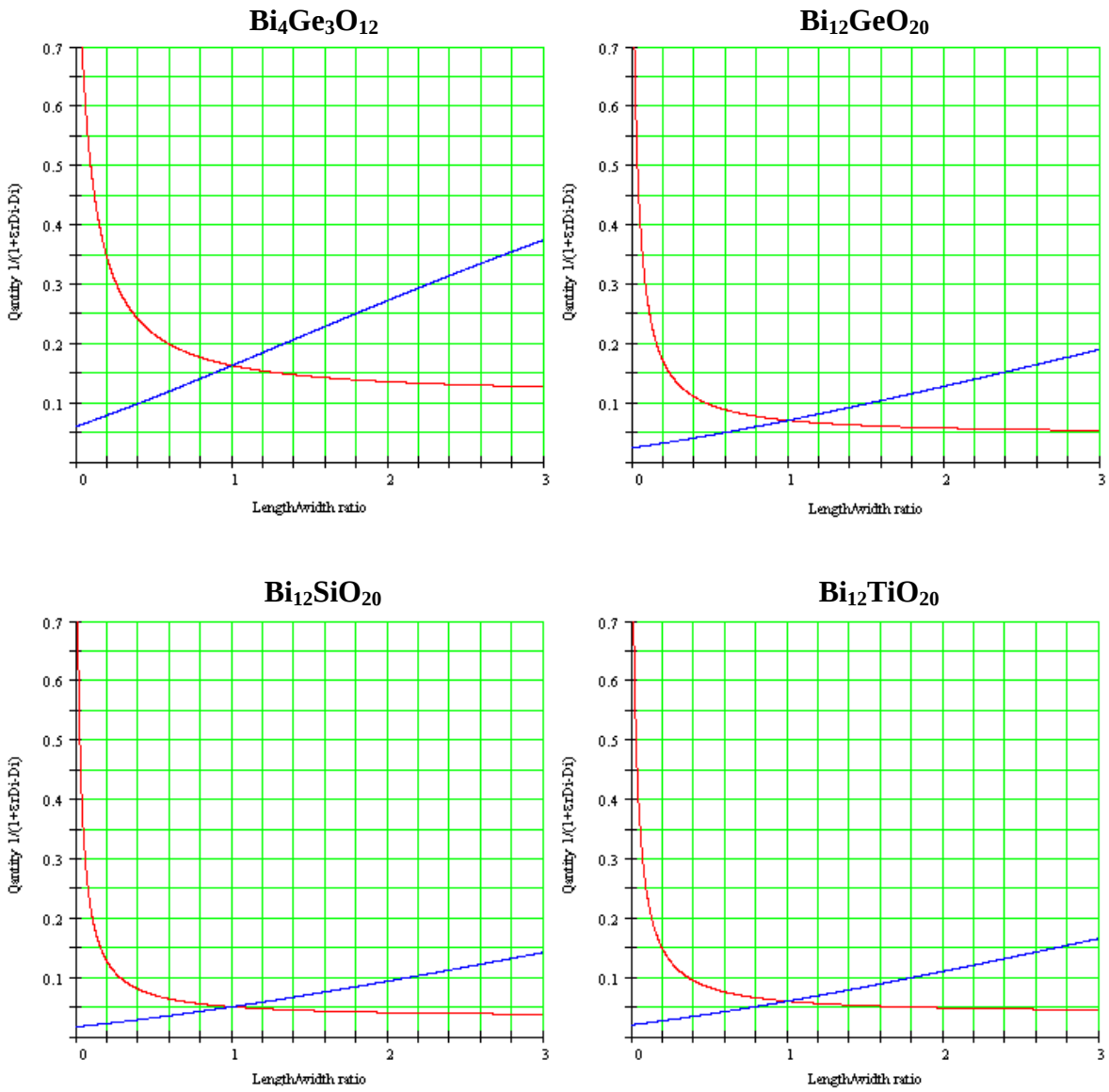

Figure 3.4 Graphic of the quantity $1/(1+\varepsilon_{ri}Di - Di)$ vs. length-width ratio for the values of $Bi_4Ge_3O_{12}$, BGO, BSO and BTO crystals; The curved graph is for $D_1 = D_2$ transversal effect, and the linear graph is for D_3 longitudinal effect, using shape 1.

To get the same sensitivity as in the case of longitudinal effect (the same attenuation for the same length) crystal width must be larger compared with the crystal length. Therefore, for the transverse effect it is suggested to use the shape 2. Figure 3.4 shows that in this case the external transverse field E_3 is attenuated more than in the case of the longitudinal effect in shape 1, but less than in the case of the transverse effect in shape 1. Hence for measurement of

one component of the electric field the dimension of the crystal along the measured field should be much higher than the dimension perpendicular to it for the same optical path.

The figure of merit $n^3 r_{41}/\lambda$, which has been used for optical modulators is plotted to compare several crystals used for electro-optic voltage sensors in Figure 3.5. Nevertheless, this figure of merit is not appropriate for electro-optic sensors, as it does not take into account the electric field attenuation discussed previously.

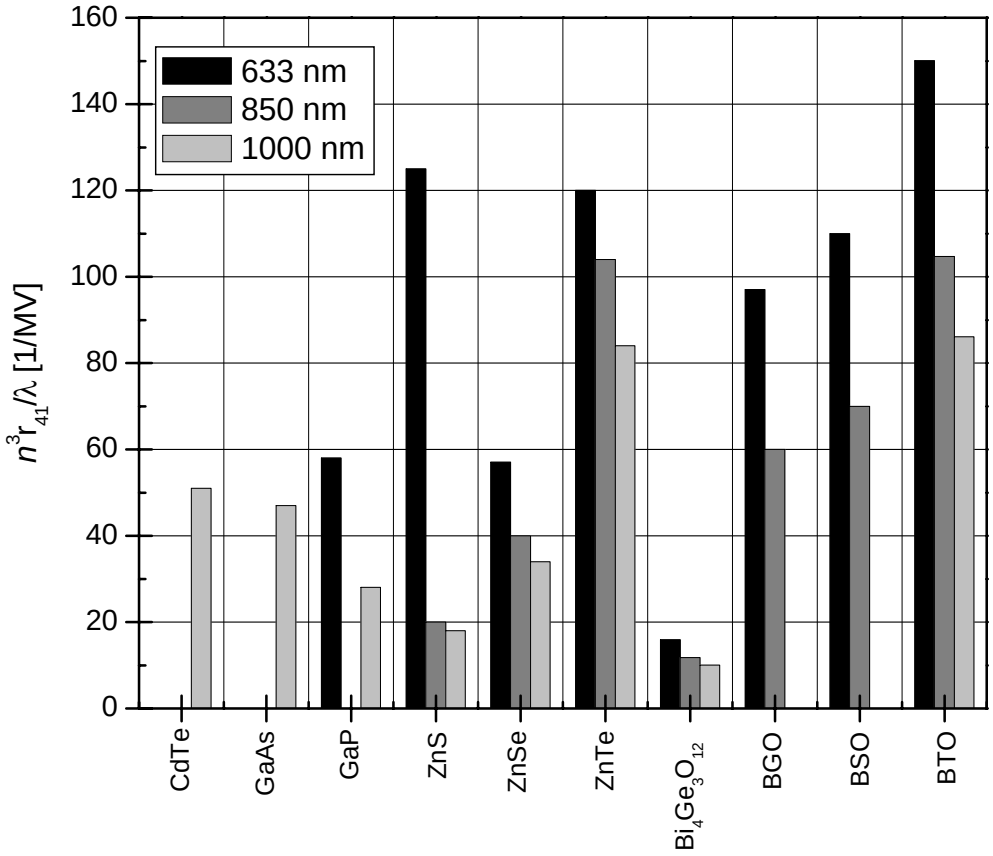

Figure 3.5 Quantity n^3 r_{41} as a figure of merit for cubic crystals [2-5 , 8, 16, 18-26]

Therefore, the figure of merit more appropriate for electro-optic sensors is [16]:

$$K = \frac{2\pi}{\lambda} \frac{n^3 r_{41}}{1 + \varepsilon_{ri} D_i - D_i} \tag{3.11}$$

This figure was calculated using available crystal data for $Bi_4Ge_3O_{12}$, BGO, BSO and BTO, simplifying crystal shape as an ellipsoid. The values of *K* shown in Figure 3.6 were calculated for the longitudinal effect in shape 1 and for aspect ratio $a = 0.4$.

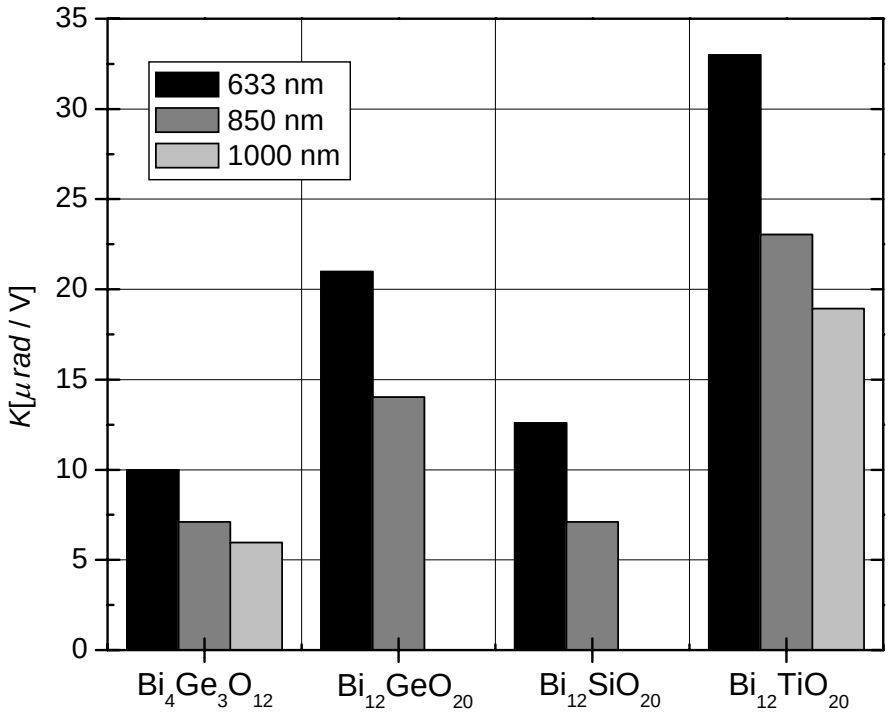

Figure 3.6 Figure of merit *K* calculated for crystals with shape of index of revolution, aspect ratio equal to 0.4 and in longitudinal electro-optic effect considered [4, 5, 8, 23-27].

Apart from the electro-optic effect that plays an important part in designing a sensor, the conductivity of the crystal becomes a dominant feature at DC and very low frequencies. After being exposed to a DC electric field, free charges in the crystal drift to the opposite sides where they accumulate and create a field of their own. This field acts against the external electric field and the electric field inside the crystal decreases with a rate depending on the crystal conductivity. Thus, when a step function external field is applied, it produces a transient internal field in the crystal, which can be described by

$$E_m(t) = E_{mo} e^{-1/\tau} \tag{3.12}$$

where E_{m0} is the internal macroscopic field in the crystal immediately after switching on the external, τ is the charge relaxation time given by [28]

$$\tau = \frac{\varepsilon_0 \varepsilon_r}{\sigma} \tag{3.13}$$

Here σ is the specific conductivity of the crystal, ε_0 and ε_r are the permitivity of vacuum and relative permitivity of the crystal respectively.

The relaxation time constant τ can be used to estimate the effect of crystal conductivity on an electro-optic sensor at DC and low frequency. Application of the Laplace transformation on a system characterized by the time constant τ gives a limit frequency of $f_{3dB} = 1/(2\pi\tau)$, at which the sensor response is decreased by 3 dB. Table 3.1 and Table 3.2 shows the limit frequency and some characteristics of the crystals considered here.

3.3.2 Photoconductivity considerations

In general, conductivity of the crystal comprises of two parts: the intrinsic conductivity and the photoconductivity. Therefore, another potential source of free charge inside the crystal is the photoconductivity effect. To create a pair of charge carriers (hole and electron), the electron in the valence band has to be excited into the conduction band. In the case of photoconductivity, the excitation energy is supplied by a flux of photons with energy $h\nu$, where ν is the frequency of light and h is Planck's constant. When considering crystals without impurities, the band gap of the material is of primary interest. It determines the absorption edge, which can be defined as the largest wavelength at which the absorption and thus the charge carrier generation occurs. This wavelength is shown as the critical wavelength in Table 3.1. To avoid the generation of free charge carriers and deterioration of the sensor frequency response, the laser source wavelength should be chosen well above its critical value.

		$Bi_4Ge_3O_{12}$	$Bi_{12}GeO_{20}$	$Bi_{12}SiO_{20}$	$Bi_{12}TiO_{20}$
Point Group		$\bar{4}3m$	23	23	23
Lattice constant [Å]		10.527	10.145	10.103	10.177
Band gap [eV]		-	3.25	3.25	3.25
E O coefficient r_{41} [m/V]		1.09×10^{-12}	3.4×10^{-12}	5×10^{-12}	5.61×10^{-12}
Transparency Range [μm]		0.3 – 6	0.4 – 7	0.4 – 6	0.5 – 6
Transmittance [633 nm]		-	67%	69%	-
Refractive Index [nm]	633	2.0975	2.55	2.54	2.5678
	850	2.066	2.46	2.283	2.513
	1000	2.058	-	-	2.485
Relative Permitivity (ε_r)		16.3	40	56	-
Resistivity [Ω·m]		2.5×10^{10}	5×10^{15}	5×10^{15}	-
Conductivity σ [S/m]		10^{-13}	10^{-9}	2×10^{-12}	-
f_{3dB} [Hz]		10^{-4}	0.56	6×10^{-4}	7.65×10^{-7}
Relaxation time τ [s]		1380	0.28	248	207975
Critical wavelength λ [nm]		-	394	394	394
Half Wave V 633 nm [kV]		33.26	-	3.85	3.3
Density [g/cm^3]		7.13	9.22	9.20	9.07
Piezoelectric d_{14} [C/N]		0.0376 C/m^2	3.44×10^{11}	4.01×10^{11}	3.72×10^{11}

Table [3.1] Properties of some crystals using for electric field sensor.

		$Bi_{12}GeO_{20}$	$Bi_{12}SiO_{20}$	$Bi_{12}TiO_{20}$
Optical activity [deg/mm]	500 nm	41.5	42	12
	600 nm	24	25	7.3
	633 nm	21	22	6.3
	870 nm	-	10.5	2.8
	1000 nm	-	7.5	2.0

Table [3.2] Optical activity of typical crystals used for electric field sensors

3.3.2.1 Space charge generation

The extensive literature is dedicated to investigation of sensors based on $Bi_{12}TiO_{20}$, $Bi_{12}GeO_{20}$, $Bi_4Ge_3O_{12}$ and $Bi_{12}TiO_{20}$ crystals [9, 26, 29, 30]. It is necessary to note that all these electro-optical crystals are well know as photosensitive materials applicable in dynamic holography and spatial modulators of light [31]. These applications are determined by the strong photosensitivity of the crystals, which is, in turn, the consequence of high photoconductivity. Authors of the majority of papers devoted to fiber sensors do not take into account the crystals' photoconductivity. This effect can impact the space charge of a crystal and therefore change its charge relaxation constant. It is supposed usually that if the wavelength exceeds the critical one determined by the forbidden band of a crystal, then the influence of the photoconductivity might be negligible. However, it is not the case. We have observed experimentally that characteristics of the sensor after electro-optic crystals vary across the light beam, as a result of the photoinduced effects in the near-infrared range[32]. Multiple traps and some of the observed effects due to the trapping mechanism in photorefractive oxide crystals $Bi_{12}MO_{20}$ (where M can be either Si, Ge or Ti) reveals that the charge transport processes could not be explained by the effective-mass approximation to the

nearly free electron in the conduction band model. However, this can be explained better by the two-center model [33].

Considering a typical configuration of an optical voltage sensor (as shown in Figure 3.2). Transparent electrodes are deposited on both working surfaces of the crystal in longitudinal modulation. Usually, the electrodes are made from In_2O_3 being the blocking ones. Therefore, electrodes do not inject electrons into the crystal.

The exposition of a crystal to light is virtually infinite during the sensor operation, resulting in appearance of photoinduced space charge in the illuminated part of the crystal. The distribution of the photoinduced part of space charge is non-uniform, corresponding to the light intensity pattern, as shows in Figure 3.7. When voltage is applied to the crystal electrodes, free charge carriers (electrons) in the crystal drift in direction opposite to the applied electric field. Such a drift leads to a space charge separation that screens the externally applied field, providing an external electric field. This field E_{int} and the total electric field inside the crystal decreases at the rate dependent on the crystal conductivity. The compensating electric field amplitude inside the crystal is determined by the concentration of free charge carriers, which is in turn, defined by the spatial distribution of the light beam. Therefore, this field has a non-uniform spatial distribution owing to photoconductivity of the crystal, leading to various modulation depths in different points throughout the light beam cross-section.

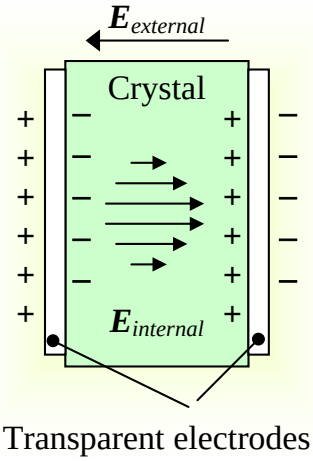

Figure 3.7. The light intensity and compensating field $\boldsymbol{E}_{\text{int}}$ distribution in the crystal.

3.3.2.2 Theory of the role of the photoconductive effect for operation of electro-optic voltage sensor

Let us consider the propagation of a symmetrical Gaussian beam through a crystal with the intensity being written as:

$$I(r) = I_0 \exp\left(\frac{-2r^2}{w^2}\right) \tag{3.14}$$

where r is the transverse coordinate and w is the Gaussian beam's spot size.

Assuming the density of the photoinduced charge being proportional to the light intensity of the compensating field being, in turn, proportional to this charge value, the internal amplitude is defined as:

$$E = E_0 \exp\left(\frac{-2r^2}{w^2}\right) \tag{3.15}$$

where E_0 is the internal field amplitude at the axis of the beam. Thus, the amplitude of the total electric field inside the crystal is given as follows:

$$E_{total} = E_{ext} - E_0 \exp\left(\frac{-2r^2}{w^2}\right) \tag{3.16}$$

According to (3.16), the total electric field varies across the crystal.

It should be noted that, as a rule, there is a spatial filtration of the light beam in a real sensor's head. This fact is the consequence of the divergence of the beam propagating and of the mismatch of the emitting and receiving apertures of the device. Therefore, the intensity of light passing through the sensor's head is given as [3]:

$$i = \int I_0 S \exp\left(\frac{-2r^2}{w^2}\right) \cos^2\left(\frac{\pi}{2} + A\left(E_{ext} - E_0 \exp\left(\frac{-2r^2}{w^2}\right)\right)\right) dS \qquad (3.17)$$

where S is the spatial filtration function, A is the factor accounting for a sensor's parameters. In particular, if a pinhole is used as a spatial filter with a transfer characteristic given by the Dirak's δ-function, Equation 3.17 is simplified resulting in:

$$i = I_0 \exp\left(\frac{-2r^2}{w^2}\right) \cos^2\left(\frac{\pi}{2} + A\left(E_{ext} - E_{\text{int}} \exp\left(\frac{-2r^2}{w^2}\right)\right)\right) \qquad (3.18)$$

The amplitude of the sensor's signal and its modulation depth are both plotted in Figure 3.8. As it follows from Figure 3.8, various points of the illuminated part of the crystal are characterized by the different modulation depth of the signal.

By the virtue of the fact that the sensor's signal is a product of the beam intensity and the modulation depth (which partially compensate each other, see curves *a* and *c* in Figure 3.8), the overall signal of the sensor is virtually constant in the central part of the beam, decreasing only to its edges (Figure 3.8 curve *b*).

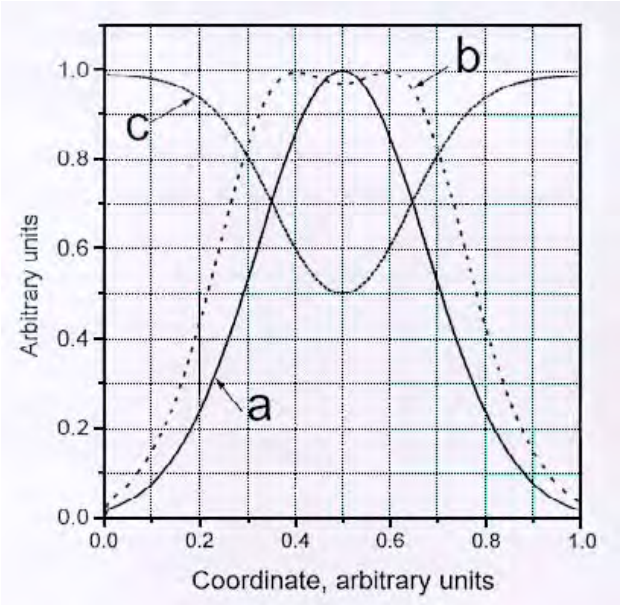

Figure 3.8. Spatial distribution in a cross section of the light beam of: (a) optical intensity, (b) sensor's signal and (c) modulation depth.

The result of the experimental studies demonstrated that the photoinduced space charge plays a significant role in optical voltage sensing, even when using an IR optical source. The crystals utilized in the sensors are never ideally pure, therefore the forbidden zone is usually filled by donor's levels. It makes possible the step-by-step absorption of IR radiation, wavelength of which essentially exceeds the critical one. Thus, the arising of the space charge could be, most probably, as a result of the step-by step absorption.

As far as impurities are believed to be the main reason for the photoinduced charge occurrence, the effects considered have to be depending strongly upon the purity of the crystal. Hence to reduce the influence of the photoinduced space charge on the sensor´s parameters, one needs to use extremely pure or specially doped crystals (e. g. doping with Ca, Al, Ga, Fe and Cr reduces the absorption and doping with Al and Fe reduces the photorefractive sensitivity [33].

The significant influence of the beam spatial function upon the light modulation depth has been testified experimentally [32]. An account of this point is crucially important for temperature stabilizing the voltage sensors' parameters. Usually, to avoid the influence of power fluctuations of the light source, the output signal of an optical voltage sensor is presented in terms of the AC/DC ratio, i. e. as the modulation depth [6,34,35]. In addition, the sensor's signal immunity to the temperature fluctuations is achieved by the combining of signals of two orthogonal polarizations in accordance with a certain algorithm [6,34]. In this case, one takes an assumption that the changes in the modulation depth versus temperature occur due to essentially internal reasons, i. e., birefringence phenomena in the phase plate used and/or the crystal, etc. Al, these features can be taken into account by developing a corresponding mathematical model of a sensor and an algorithm of the signal processing [34]. However, if the spatial filtration function of a beam S varies with temperature (owing to a particular sensitive element design), the modulation depth will vary as well (Equation 3.17). It can easy happen, for example, if some misalignment of the emitting and receiving apertures of ball lenses or Selfoc lenses takes place [32,34], resulted from the temperature changes.

Besides of this, the density of the photoinduced space charge itself significantly depends on temperature (as far as the recombination rate of an electron-hole pair is a function of temperature). Thus the modulation depth can vary, even though the changes in the spatial

filtration conditions do not occur, simply because of the changes in the internal compensating field amplitude, which is temperature dependent.

Has been found experimentally, that the modulation depth of the sensor is determined by the light intensity. At high optical powers (up to 100 mW), the variations of the modulation depth are saturated with the changes to be described by the exponential law (Figure 3.9). At low optical powers (0.5 – 3 mW), that is usually the case in the optical voltage sensors, the modulation depth varies much more rapidly. Hence, the widespread point of view, that the modulation depth does not depend on optical power, is not valid for photorefractive electro-optic crystals. It can be seen from Figure 3.9 that the modulation depth depends upon the probing beam power under the exponential law, with the characteristics constants being determined by the specific spatial filtration conditions. To remove this undesirable effect, one has the two principle opportunities. The first one is the use of weak opticals powers as well as far IR sources, which makes insufficient the space charge influence on a sensor's operation, since the modulation depth is independent of a probing point in the beam's cross-section. The second one is the use of high power optical sources (i. e. Exploiting the saturation part of curves in Figure 3.9), since in the last case the changes in the source's intensity do not lead to significant changes in the modulation depth of the sensor. This approach allows also enhancing the signal-to-noise ratio.

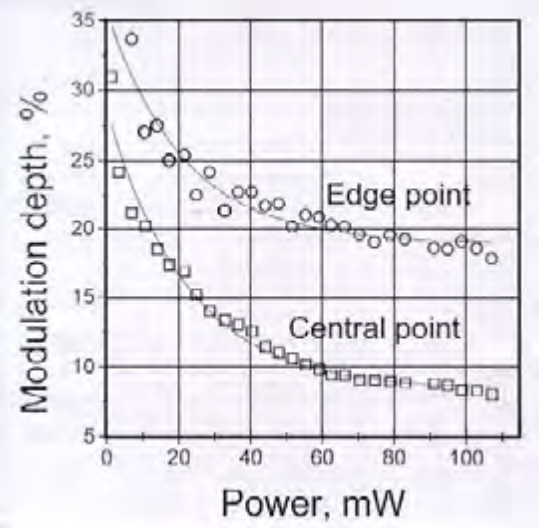

Figure 3.9. Light modulation depth as a function of optical power for central (squares) and edge (circles) pinhole position. Solid lines represent exponential approximation under the law $m = 8.4 + 20.5 \exp(-P/22)[\%]$ (central point) and $m = 18.86 + 16.89 \exp(-P/21.73)[\%]$ (edge point) as well [32].

The simple theoretical model proposed by Filippov et al. adequately describes the role of the photoconductive effect in a voltage sensor based on sillenite crystals. This model shows that the presence of the photoinduced space charge in the crystal makes the signal modulation depth to be dependent on a position across the optical beam and on the signal intensity.

§3.4 Polarimetric voltage sensors

Polarimetric voltage sensors either in bulk material, waveguides or fiber have a simple basic construction as seen in Figure 3.2. The input polarization state is oriented 45° to the Pockels induced birefringence. A quarter-waveplate biases the output so that the response is in the linear portion of the squared sinusoid function. Either an analyzer or polarizing beam splitter, oriented crossed to the input polarizer, is used to convert the change in polarization state into change in intensity. With a polarizing beam splitter, difference-over-sum signal processing can be carried out to reduce common-mode noise.

The response of a sensor in this arrangement is

$$R(V)_{\pm} = A_{\pm}(1 \pm \sin(\Gamma(V)) \tag{3.14}$$

where $A_{\pm}$ is the optical transmittance of the sensor and Γ (V) is the Pockels' retardance described in Equation 3.3 or Equation 3.4. The "±" refers to the orientation of the output polariser beam splitter. Equation 3.4 is the ideal response; if the crystal has some static retardance that is at 45° with respect to the Pockels' retardance, then the response can be expressed as:

$$R(V,\Gamma_s)_{\pm} = A_{\pm}\left(1 \pm \Gamma(V)\frac{\sin 2\phi}{2\phi}\right) \tag{3.15}$$

where Γ_s is the static retardance and $\phi = \frac{1}{2}\left(\Gamma_s^2 + \Gamma(V)^2\right)^{1/2}$ [8, 29]. Equation 3.15 applies to a BGO sensor configured as shown in Figure 3.2. The static retardance, the quarter-wave plate, and the temperature dependence of the Pockels effect all contribute to the instability of the sensor. In materials with optical activity, such as BTO, there will be added temperature-dependent terms. In some cases the optical activity can be used to compensate for the temperature dependence of the Pockels effect.

3.4.1 Bismuth germanate sensors

$Bi_4Ge_3O_{12}$ material is used for those applications of electro-optic effect, such as voltage and electric field sensors, in which precision (reproducibility or stability) is more important than sensitivity [26, 36-41]. It is a cubic crystal that does not exhibit natural linear birefringence, which is a major cause of instability in many electro-optic devices. Neither does exhibit circular birefringence (optical activity), which quenches the electro-optic effect and reduces its stability. Bismuth germanate is transparent from approximately 350 nm to 4 μm, which suggests that its optical properties in the 800-1500 nm spectral region (where most sensors operate) should be relatively stable with temperature.

A useful configuration is where the crystal is cut for longitudinal operation, with the electric field and optical beam propagation parallel, with the electrodes placed on the ends of the crystal. This design works well for high voltage applications, at 200 kV and up [26, 36-41]. The required cut of the crystal is different described in section 3.2.1; the electric field and optical are normal to the (001) crystal plane. The other crystal plane (100) remains isotropic. The longitudinal operation removes the dependence on crystal size from the Pockels retardance so that

$$\Gamma = \frac{2\pi}{\lambda} n_0^3 r_{41} V \tag{3.16}$$

where n_0 is the crystal's index of refraction, and r_{41} is the electro-optic coefficient [3, 4]. Because the dependence on l / d is removed, the sensitivity to the voltage is usually a factor of four to 10 smaller, but the design allows the sensor to be implemented in gas insulated high voltage switchgear (GIS) environments where small crystal sizes and breakdown would be a concern.

With the basic optical design and material selected, we can estimate the temperature dependence of a voltage sensor with a processed response function:

$$R(V,\Gamma_S)_{\Delta ac/dc} = \frac{R(V,\Gamma_S)_{\Delta ac}}{R(V,\Gamma_S)_{dc}} \tag{3.17}$$

where $V = V_0 \sin(\omega t)$ and $R(V,\Gamma_S)_{\Delta ac} = R(V,\Gamma_S)_{ac+} - R(V,\Gamma_S)_{ac-} \times R(V,\Gamma_S)_{dc}$ is the dc part of the 2.36 and ω is the angular frequency of the applied voltage. The normalized temperature dependence, using Equation 3.15 and Equation 3.3 or Equation 3.17 is: [36]

$$\frac{1}{R(V,\Gamma_S)_{\Delta ac/dc}} \frac{dR(V,\Gamma_S)_{\Delta ac/dc}}{dT} = \frac{1}{n_0^3 r_{41}} \frac{dn_0^3 r_{41}}{dT}\left(1 + X\Gamma(V)^2\right) + X\Gamma_S \frac{d\Gamma_S}{dT} \tag{3.18}$$

where X is

$$X = \frac{\cot 2\phi}{2\phi} - \frac{1}{4\phi^2} \tag{3.19}$$

When $\Gamma(V_0) = 0$ and Γ_S is greater than 1 ^{o} but less than 80 ^{o}, X has a value of about – 1/3. The first term in Equation 2.48 is the index and electro-optic coefficients's contribution to the normalized temperature dependence of the voltage sensor. The quantity $\frac{1}{n_0^3}\frac{dn_0^3 r_{41}}{dT}$ has been measured and is $(1.54 \pm 0.16) \times 10^{-4}$ / ^{o}C for Bismuth Germanate [36]. The temperature dependence of Γ_S can be positive or negative of the order of 10^{3} / ^{o}C to 10^{-2} / ^{o}C [40]. If

$\frac{1}{\Gamma_S}\frac{d\Gamma_S}{dT}$ is positive, temperature compensation can occur, since *X* is negative for crystals that are useful. In practice the size and sign of the temperature dependence of Γ_S are difficult to predict. A practical way to minimize the sensor's temperature dependence is to reduce Γ_S [40]. Equation 2.48 includes only the material-related sources of temperature dependence. Opto-mechanical instabilities can add to temperature dependence as well.

3.4.2 Bismuth Sillenite Sensors

Another popular material used in voltage sensing is BSO [29,34,41-43]. As mentioned earlier (see section §3.3) BSO is similar to $Bi_4Ge_3O_{12}$ except BSO has optical activity. A voltage sensor using BSO can be modeled in a form similar to that of a polarimetric current sensor with linear birefringence, except that now the rotation is due to optical activity ρ and not current or the Faraday rotation ρ_F. The difference-over-sum response of a BSO voltage sensor, assuming $\Gamma_S < \rho$, is

$$R_{\Delta/\Sigma}(V) = \frac{\Gamma_S}{\rho}\left(\cos(2\gamma) - \cos(2\gamma - 2\rho)\right) \tag{3.20}$$

where γ is the angle between the polarizer and the crystal birefringence Γ_S axis and $R_{\Delta/\Sigma}(V)$ is the ratio between the difference ($I_1 - I_2$) and the sum ($I_1 + I_2$) of the intensities in the photodetectors, processing the output signals in the polarimetric optical scheme shown in Figure 3.2 [6]. Normally the sensor would have $\gamma = 45^{\circ}$ so that $R_{\Delta/\Sigma}(V) = \Gamma_S \sin(2\rho)/\rho$.

The temperature dependence of this sensor can be modeled as:

$$\frac{1}{R_{\Delta/T}(V)}\frac{dR_{\Delta/\Sigma}(V)}{dT} = \frac{1}{\Gamma_S}\frac{d\Gamma_S}{dT} - \frac{1}{\rho}\frac{d\rho}{dT}\left(1 + 2\rho\tan(2\gamma - 2\rho)\right) \tag{3.21}$$

From Equation (3.21), it can be seen that the temperature dependence of the Pockel's term can be compensated by the temperature dependence of the optical activity by selecting the proper angle γ and the crystal length. Adjusting γ allows some range in the selection of the crystal [6].

In some cases the angle can not be easily adjusted because this procedure would add too much cost to the sensor. For the situation where $\gamma = 45^{\circ}$, the temperature dependence of the sensor is:

$$\frac{1}{R_{\Delta/\Sigma}(V)}\frac{dR_{\Delta/\Sigma}(V)}{dT} = \frac{1}{\Gamma_S}\frac{d\Gamma_S}{dT} - \frac{1}{\rho}\frac{d\rho}{dT}\left(1 + 2\rho\cot(2\rho)\right) \tag{3.22}$$

Now the proper length is needed to compensate for the temperature dependence of the Pockels effect [38]. For the temperature dependence of the output to be near zero we find that the crystal length should be approximately 4 mm, using the values given for the normalized temperature dependence of Γ_S and ρ, and the optical activity per unit length shown in Table 3.2 [6,38]. In some cases a 4 mm long crystal has a low voltage sensitivity. Another approach is to use the dc component of Equation 3.20 to compensate for the change in the ac response [34]. Recently a third approach was demonstrated that uses two detection arrangements to separate the temperature and voltage effects from the output of a voltage sensor [44].

Similar analysis is applicable to BGO and BTO crystals, considering the adequate optical activity for each case.

3.4.3 Integrated-optic sensors

Integrated-optic polarimetric voltage sensors (IOPV) typically use Y-cut $LiNbO_3$ crystals with titanium in-diffused waveguides [10, 45-51]. As mentioned earlier in sub-Section 2.6.1.1 if the crystal is cut properly, the Y-optical path will have no linear birefringence; however, because of the waveguide birefringence there is a static retardance in these devices.

The transverse electric (TE) and transverse magnetic (TM) modes have different propagation constants or indices of refraction. Typically the $LiNbO_3$ crystal is cut so that $\Gamma_{TE-TM} = \pi / 2 + 2 m\pi$, where m is an integer.

Waveguides cut in this fashion will acts as a multiple-order quarter-waveplate that biases the operation of the sensor into the linear portion of the transfer function. This requires cutting the waveguide to the proper length l with an uncertainty of about 100 μm for most titanium in-diffused waveguides [10,49]. The better waveguide will be with the lower Γ_{TE-TM} .

IOPV sensors launch linearly polarized light from a polarizing prism or polarization maintaining fiber into the waveguide at 45° to the TE and TM modes. The output polarizer can be fiber based on the chip or remotely located with PM fiber. Figure 3.10 shows a diagram of the sensor [10, 45-51]. Sensors built in this way have the potential for mass production and low cost, and are currently being produced.

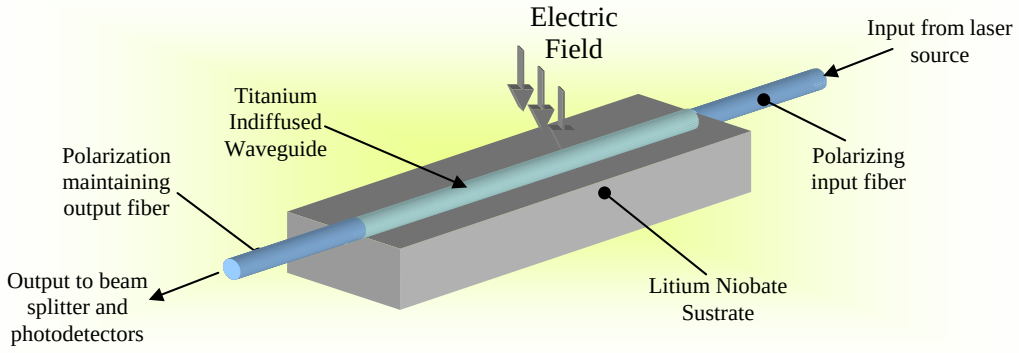

Figure 3.10. Schematic of a $LiNbO_3$ integrated-optic voltage sensor.

The temperature dependence of the sensors is potentially small because of the low temperature dependence of the Pockels effect in $LiNbO_3$. The normalized temperature dependence of the waveguide birefringence is about 2.5×10^{-4} /°C and dominates the temperature dependence of the response for an IOPV sensor [49]. If the waveguide is prepared well, the temperature dependence of a $LiNbO_3$ waveguide sensor can be less than that of a voltage sensor using BGO.

3.4.4 Optical fiber sensor

There are two effects that allow an optical fiber to measure an electric field or voltage. One is to artificially create linear electro-optic coefficient in the fiber by poling and the other is the electro-optic Kerr effect.

Optical fiber and glass waveguides can be poled to increase the linear electro-optic coefficient to levels as high as ~ 6 pm /V, but ~ 3 pm /V is more typical [52-54]. Poling a fiber involves a process where an extremely high electric field is placed on the glass fiber while the temperature is raised to nearly 300 ^{o}C, then reduced. This introduces a permanent electric polarization within the fiber. These poled fibers have high sensitivity, but the poling effect degrades with the time and temperature [52]. If high temperatures are required, > 100 ^{o}C, the poling effect quickly decays [52]. So far no practical utility applications have been found for these fibers. If a method for stabilizing the poling process is found then sensors using poled fibers may be commercialized.

A fiber voltage sensor can be also be made using the electro-optic Kerr effect. However, a long length, ~ 10 m, of fiber must be placed in an extremely high electric field, E_0 > 1 MV/m. Also, the electro-optic Kerr effect has a large temperature dependence [15]. For these reasons practical voltage sensors using the electro-optic Kerr effect have not been pursued.

§3.5 Interferometric voltage sensors

As mentioned earlier there are several interferometric voltage sensors designs [55–64]. Interferometric voltage sensors can be constructed in a Mach-Zehnder interferometer (MZI) arrangement shown in Figure 3.11 where one arm of the interferometer is sensitive to an electric field or voltage. Many electro-optic modulators use this format in $LiNbO_3$ waveguides. The response of the MZI is:

$$R(V)_{MZ} = \frac{A_{MZ}}{2}\left[1 + B_{MZ}\cos\left(\frac{2\pi}{\lambda}\frac{l}{d}n_0^3 r_{22}V + \phi_B\right)\right] \tag{3.23}$$

where A_{MZ} is the transmittance, B_{MZ} is a parameter that includes manufacturing imperfections, and ϕ_B is the intrinsic phase bias between the two interferometer paths [55].

Voltage sensors constructed in a $LiNbO_3$ waveguide have one of the arms of the interferometer shielded from the electric field, with or without electrodes, or have a domain inversion so that the electro-optic effect produces the opposite phase shift [56]. MZI sensors are not stable with temperature, having a large change in the ϕ_B bias with temperature of the order of $1^\circ / {}^\circ C$ [52]. For this reason there are few practical applications of these sensors.

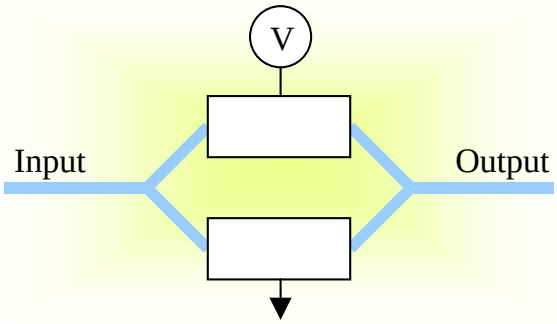

Figure 3.11. Schematic of a Mach-Zehnder interferometric voltage sensor.

Another type of interferometric voltage sensors uses a dual-mode white-light fiber interferometer [53,54]. A fiber operating at a wavelength such that two modes are supported, the LP_{01} and the LP_{11} modes, is wrapped on a quartz disk or rod [57-62]. A voltage is placed on the rod to change the diameter and stretch the dual mode fiber. The interferometer is formed by each of the two fiber modes accumulating different amounts of phase along the length of the fiber. The quartz expands with voltage and the two modes of the fiber experience different amounts of phase shift. A second dual mode interferometer with piezoelectric modulators is used to homodyne phase track the first interferometer [57].

The second interferometer compensates for temperature drift in the sensor, which is independent of temperature between – 10 to 45 $^\circ C$ [57]. This quartz rod sensor has been used in 400 kV GIS applications [58].

§3.6 Conclusions and remarks

For voltage sensors based on the electro-optic effect, we know that the most appropriate materials are the crystals of the group 23 and $\bar{4}3m$. We have made a comparative study from which we can emphasize the advantages that offers the crystal $Bi_{12}TiO_{20}$ of the crystallographic point 23 over the other crystals. This crystal, in particular shows a high sensitivity for different wavelength (in the near infrared). For measurements of periodic signals of voltage, it is required that the signal possesses a wavelength above the critical wavelength for the crystal.

Making use of the depolarization factors for ellipsoids in general, we have demonstrated that the dimensions of the crystal should be taken into account for the design and construction of voltage sensors based on the Pockels effect. Of this study, we conclude that the glass BTO conserves the advantages when the longitude of the crystal does not surpass certain value of approximately 4 mm. For crystals with more longitude, the attenuation in the sensitivity is considerable.

Taking into account the role of the photoconductivity effect in the sensitivity of the sensor, it is known that the presence of the photoinduced space charge in a crystal, produces that the modulation depth of the signal be dependent of the position across the optical beam and on the signal intensity, whenever a near infrared source is used. The parameters of the sensor are also affected due to the photoinduced space charge. To reduce this effect, the use of optical sources of high power (more than 10 mW) or doped crystals with extremely low photoconductivity is proposed.

Characteristics, advantages and disadvantages of the several configurations for voltage sensors based on the electro-optic effect reported up to now in the literature, has been established.

References

[1] Lucas J. R., *High Voltage Engineering*, revised edition, (Open University of Sri Lanka, 2001), Chap 6.

[2] Susumu Namba, "High voltage measurement by ADP crystal plate", *Rev. Sci. Instrum.*, vol. **27 A**, No. 5, 336, (1956).

[3] Amnon Yariv and P. Yeh, *Optical Waves in Crystals*, 1st Ed., (John Wiley & Sons, New York, 1984), Chaps. 1-8.

[4] P. A. Williams, A. H. Rose, K. S. Lee, D. C. Conrad, G. W. Day and P. H. Dale, "Optical, thermo-optic and photoelastic properties of bismuth germanate ($Bi_4Ge_3O_{12}$), *Appl. Opt.*, vol. **35**, No. 19, 3562-3569, (1996).

[5] Michael Bordovsky, Franjo Cecelja, Bala Balachandran, "Comparative study of cubic cristals performance in bulk electro-optic sensor for DC and extra low frequency measurements", SPIE vol. **2839**, pp.166-173, (1996).

[6] Andreas Koch, Christian Helmig and Hartwig Senftleben, "Experimental Studies on a Temperature Compensation for Optical Voltage Sensing", 12th International Conference on Optical Fiber Sensors, *OSA Tech. Digest*, vol. **16**, pp.257-260, (1997).

[7] P. Pella-Finet, "Measurement of the electro-optic coefficient of BSO crystals", *Opt. Comm* vol. **50**, pp. 275-280, (1984).

[8] D. G. Papazoglou, A. G. Aportolidis and E. D. Vanidhis, "Index of refraction, optical activity and electro-optic coefficient of bismuth titanium oxide ($Bi_{12}TiO_{20}$)", *Appl. Phys. B*, vol. **65**, pp. 499-503, (1997).

[9] Valery N. Filippov, Andrey N. Starodumov, Yuri O. Barmenkov and Vladim V.Makarov, "Fiber Optic Voltage Sensor Based on a $Bi_{12}TiO_{20}$ crystal", *Appl. Opt.*, vol **39**, No. 9, pp. 1389-1393. (2000).

[10] Osamu Ogawa, Tomohiro Sowa and Shinichi Ichizono, "A Guided-Wave Optical Electric Field Sensor with Improved Temperature Stability", *J. Lightwave Technol.*, vol. **17,** No. 5, pp.823-830, (1999).

[11] G. R. Allen, H. P. Davis, B. T. Neyer, D. J. Muron and J. Chang, “Electro-Optical Kerr Effect Voltage Measurements On Multi-Megavolt Pulsed Power Acelerators”, SPIE on Fiber Optic and Laser Sensors III, vol. **566**, pp. 223-226, (1985).

[12] M. Abd-Elsalam, M. Abdel-Salam, D. Wiitanen and W. Perger, “A new laser voltmeter”, *Meas. Sci. Technol.*, vol. **4**, pp. 311-320, (1993).

[13] Wang Zhaobing, Liao Yanbiao, Lai Shurong, Zhao Huafeng, “Fiber Sensor for Simultaneous Measurement of Current and Voltage by single Lo-Bi fiber”, SPIE vol. **2895**, pp. 26-32, (1996).

[14] S. Simon and R. Ulrich, “Evolution of polarization along a single-mode fiber”, *Appl. Phys. Lett.*, vol. **31**, pp. 517-520, (1977).

[15] M. C. Farries and A. J. Rogers, “Temperature dependence of the Kerr effect in a silica optical fiber”, *Electron. Lett.*, vol. **19**, 890-891, (1983).

[16] G. A. Massey, D. C. Erickson and R. A. Kadlec, “Electromagnetic Field Components: Their Measurement Using Linear Electrooptic and Magnetooptic Effects”, *Appl. Opt.* , vol. **14**, No. 11, pp. 2712-2719, (1975).

[17] J. A. Stratton, *Electromagnetic Theory*, (Mc Graw Hill, New York, 1941), Ch. 3.

[18] S. J. Czyzak, W. M. Baker, R. C. Crane and J. B. Howe, “Refractive indexes of single synthetic zinc sulfide and cadmium sulfide crystals”, *J. Opt. Soc. Am.*, vol. **47**, No. 3, pp. 240-243, (1957).

[19] D. T. F. Marple, “Refractive index of GaAs”, *J. Appl. Phys.*, vol. **35**, No. 4, pp. 1241-1242, (1962).

[20] D. T. F. Marple, “Refractive index of ZnSe, ZnTe and CdTe”, *J. Appl. Phys.*, vol. **35**, No. 3, pp. 539-542, (1964).

[21] T. R. Sliker, J. M. Jost, “Linear electro-optic effect and refractive indices of cubic ZnTe”, *J. Opt. Soc.*, vol. **35**, pp. 130-131, (1966).

[22] J. E. Kiefer and A. Yariv, “Electro-optic characteristics of Cd Te at 3.39 and 10.6 microns”, *Appl. Phys. Lett.*, vol **15**, No. 1, pp. 91-97, (1968).

[23] R. E. Aldrich, S. L. Hou and M. L. Harvill, “Electrical and optical properties of $Bi_{12}SiO_{20}$”, *J. Appl. Phys.*, vol. **42**, pp. 493-494, (1971).

[24] D. P. Bortfeld and H. Meier, “Refractive indices and electro-optic coefficients of the eulytites $Bi_4Ge_3O_{12}$ and $Bi_4Si_3O_{12}$”, *J. Appl. Phys.*, vol. **43**, pp. 5110-5111, (1972).

[25] R. A. Mullen and R. W. Hellwarth, "Optical measurement of the photorefractive parameters of $Bi_{12}SiO_{20}$", *J. Appl. Phys.*, vol. **58**, No. 1, pp.40-44, (1985).

[26] Osamu Kamada and Kazuhiko Kakishita, "Electro-Optical Effect of $Bi_4Ge_3O_{12}$ Crystals for Optical Voltage Sensors", *Jpn. J. Appl. Phys*., vol. **32** No. 9B, pp. 4288-4291, (1993).

[27] Institute of Solid State Physics, Russian Academy of Sciences, http://www.issp.ac.ru.

[28] P. Günter, "Electro-optic and Photorefractive Materials", Proceedings of the international school on material science and technology, Erice Italy, pp. 206-228, (1986).

[29] Y. Kuhara, Y. Hamasaki, A. Kawakami, Y. Murakami, M. Tatsumi, H. Takimoto, K. Tada and T. Mitsui, "BSO/Fibre-Optic Voltmeter with Excellent Temperature Stability", *Electron. Lett.*, vol. **18** No. 24, pp. 1055-1056, (1982).

[30] Kazuo Kyuma, Shuichi Tai, Masahiro Nunoshita, Noboru Mikami and Yoshiaki Ida, "Fiber-Optic current and voltage sensor using a $Bi_{12}GeO_{20}$ single crystal", Journal of Lightwave Technology, vol. **LT-1**(1), pp. 93-97, (1983).

[31] S. I. Stepanov, "Applications of Photorefractive Crystals", *Rep. Prog. Phys*., pp. 39-116, (1994).

[32] Valery N. Filippov, Andrei N. Starodumov, Alexander V. Kir'yanov and Alejandro Martínez-Rios, "The role of the photoconductive effect in operation of $Bi_{12}TiO_{20}$-based optical voltage sensor", *Opt. Quantum Electron.*, vol. **34**, pp. 867-875, (2002).

[33] K. Buse, "Light-induced charge transport processes in photorefractive crystals II:Materials", *Appl. Phys. B*, vol. **64**, pp. 391-407, (1997).

[34] J. Niewisch, Peter Menke, P. Krammer, Thomas Bosselmann, "Temperature Drift Compensation of a Potential Transformer using a BSO Pockels Cell", *Eleventh International Conference on Optical Fiber Sensors, Jpn. Soc. Appl. Phys.*, pp. 152-155, (1996).

[35] Thomas Bosselmann, "Magneto and Electrooptic Transformers meet espectations of Power Industry", from the 12th International Conference on Optical Fiber Sensors, *Opt. Soc. Am.*, vol. **16**, pp. 111-114, (1997).

[36] Allen H. Rose and Gordon W. Day, "Optical fiber voltage sensors for broad temperature ranges", Proc. SPIE vol. **1580**, pp. 95-103, (1992).

[37] Xiaojun Zeng and Haiqing Chen, “Electro-optical measurement of highly intense electric field with high frequency”, in Optical Sensing, Imaging and Manipulation for Biological and Biomedical Applications”, Proceedings of SPIE vol. 4082, 2000, pp. 298-304.

[38] Josemir Coelho Santos, Muslum Cengiz Taplamacioglu and Kunhiko Hidaka “Optical High Voltage Measurement Using Pockels Microsingle Crystal”, Review of Scientific Instruments vol 70 No. 8, August 1999, pp. 3271-3276.

[39] H. J. M. Hulshof, W. R. Rutgers, A.H. v.d. Wey, “Optical Voltage Sensors: Aplications in Electric Power Systems”, SPIE on Fiber Optic Sensors II, 1987, pp. 266-269.

[40] Kyung Shik Lee, “Electrooptic Voltage Sensors: Birrefringence Effects and Compensation Methods”, Applied Optics vol 39 No 30, 20 October 1990, pp. 4453-4461.

[41] Y. Koruda, Y. Abe, H. Kuwahara and K. Yoshinaga, “Field Test of Fiber-Optic Voltage and Current Sensors Applied to Gas Insulated Substation”, SPIE vol 586 on Fiber Optic Sensors, 1985, pp. 30-37.

[42] M. Norimatsu and M. Shirasaki, “$Bi_{12}SiO_{20}$ crystal application for voltage sensor in optical fibers”, Ferroelectrics, , vol **75**, pp. 189-196, (1987).

[43] Yuji Hamasaki, Hideo Gotoh, Masaaki Katoh, Seiichi Takeuchi, “OPSEF : An Optical Sensor for Measurement of High Electric Field Intensity”, Electronics Letters vol 16 No. 11, 22nd May 1980, pp. 406-407.

[43] Toshihico Yoshino, “Optical Fiber Sensors for Electric Industry”, *SPIE on Fiber Optic Sensors II*, vol. **798**, pp. 258-265, (1987).

[44] Xiaoping Zheng and Yanbiao Liao, “A Technique for Fiber Optic Voltage Sensor to Realize Temperature Compensation”, *IEICE Trans*. Electron., Special Issue on Optical Fiber Sensors, vol. **E83-C**, No. 3, pp.342-346, (2000).

[45] Catherine H. Bulmer, W. K. Burns and R. P. Moeller, “Linear Interferometric Waveguide Modulator for Electromagnetic-Field Detection”, *Opt. Lett*., vol. **5** No. 5, pp. 176-178, (1980).

[46] Christian Duchet, “Integrated Electro-Optic Modulators With High Sensitivity For Remote Voltage Sensing”, SPIE on Fiber Optic Sensors, vol. **586**, pp. 45-50, (1985).

[47] Christian Duchet, P. Fabre, M. DiMaggio, “Thermal Stability of $LiNbO_3$ Electro-Optic Waveguide Modulators for Remote Voltage Sensing”, SPIE on Fiber Optic and Laser Sensors V, vol. **838**, pp. 39-43, (1987).

[48] Catherine H. Bulmer, “Sensitive, Highly Linear Litium Niobate Interferometers for Electromagnetic Field Sensing”, *Appl. Phys. Lett*., vol. **53** No. 24, pp. 2368-2370. (1988).

[49] Nicolas A. F. Jaeger and Farnoosh Rahmatian, “Bias Integratred Optics Pockels Cell High-Voltage Sensors”, SPIE vol **2072**, pp. 87-95, (1994).

[50] David H. Naghski, Joseph T. Boyd, Howard E. Jackson, S. Sriram Stuart A. Kingsley and J. Latess, “An Integrated Photonic Mach-Zehnder Interferometer with No Electrodes for Sensing Electric Fields”, *J Lightwave Technol*., vol. **12**, No. 6, pp. 1092-1098, (1994).

[51] S. A. Kingsley and S. Sriram, “Parallel-Plate Integrated Optic High-Voltage Sensor”, *Electron. Lett*., vol. **31**, No. 13, pp. 1096-1097, (1995).

[52] X. C. Long and S. R. J. Brueck, “Large-Signal Phase Retardation with a Poled Electro-Optic Fiber”, *IEEE Photonics Technol. Lett.*, vol. **9**, pp. 767-769, 1997.

[53] P. G. Kazansky, P. St. J. Russell and H. Takebe, “Glass Fiber Poling and Applications”, *J Lightwave Technol.*, vol. **15**, pp. 1484-1493, (1997).

[54] D. Wong, W. Xu, S. Fleming, M. Janos and K. M. Lo, “Frozen-in Electrical Field in Thermally Poled Fibers”, *Opt Fiber Technol*, vol. **5**, pp. 235-241, (1999).

[55] Nicolas A. F. Jaeger and L. Young, “High Voltage Sensor Employing an Integrated Optics Mach-Zehnder Interferometer in Conjunction with a Capacitive Divider”, *J Lightwave Technol.*, vol. **7**, pp. 229-234, (1989).

[56] Nicolas A. F. Jaeger and L. Young, “Asymmetric Slab and Strip-Loaded Integrated Optic Devices for the Measurement of Large Electric Fields”, *J Lightwave Technol.*, vol. **LT-5**, pp. 745-750, (1987).

[57] Klaus M. Bohnert, H. Brändle and G. Frosio, “Field Test Interferometric Optical Fiber High Voltage and Current Sensors”, SPIE 2360 on “Tenth Optical Fibre Sensors Conference”, October 1994, pp. 16-19.

[58] Klaus M. Bohnert, Mathias Ingold and Jadran Kostovic, “Fiber-Optic Voltage Sensor for SF_6 insulated High-Voltage Switchgear”, Applied Optics, vol. 38 No. 10, 1 April 1999, pp. 1926-1933.

[59] Klaus M. Bohnert and J. Nehring, “Fiber Optic Sensig of Electric Field Components”, Applied Optics vol. 27 No.23, 1 December 1988, pp.4814-4818.

[60] Klaus M. Bohnert and J. Nehring, “Fiber-Optic Sensing of Voltages by Line Integration of the Electric Field”, Optical Society of America, Vol. 14, No. 5, March 1 1989, pp. 290-292.

[61] Klaus M. Bohnert and P. Pequignot, “Inherent Temperature Compensation of a Dual-Mode Fiber Voltage Sensor with Coherence-Tuned Interrogation”, Journal of Lightwave Technology, vol. 16 No. 4, April 1998, pp. 598-604.

[62] Klaus M. Bohnert, Jadran Kostovic and Pascal Pequignot, “Fiber Optic Voltage Sensor for 420 kV electric power systems”, Optical Engineering, vol. 39, No. 11, November 2000, pp. 3060-3067.

[63] Huang Yonglin, Feng Dejun, Xu Zhaowen, Tong Zhengrong, Kai Guiyun and Dong Xiaoyi, “A Voltage Sensor Utilizing All-Fiber Mach-Zehnder Interferometer”, *Proceedings of SPIE*, vol. **4603**, pp. 188-191, (2001).

[64] V. B. Baglikov, R. Yu. Dolinin, E. M. Zolotov, V. M. Pelekhatyi and R. F. Tavlykaev, “Investigation of an electric field sensor based on an integrated optical Mach-Zehnder modulator”, *Sov. J. Quantum Electron.*, vol. **18**, No 10, pp. 1353-1355, (1988).

Chapter Four:

Fiber optic optically controlled voltage sensor

§4.1 Introduction

Fiber-optics voltage sensors based on cubic crystals are currently widely used owing to a set of advantages the absence of conducting elements, small dimensions, and immunity to electrical interference. Their additional advantage is the possibility to create local nets allowing voltage control in locations at large distances.

Meanwhile, all the voltage sensors described to date in literature have a considerable disadvantage: Their sensitivity is constant being determined by the type of an electro-optical crystal and phase plate orientation used [1-4]. Nevertheless, in some applications, it is required to change the sensitivity of a primary transformer in order to vary the range of measurements, which is not possible to approach with the existing devices [4-6].

Recently, a fiber optical voltage sensor with variable optical sensitivity has been proposed [7]. The sensor operates at two widely separated wavelengths, one of which is correspond to a control signal. In this part we described in detail operation of this sensor. Modulation depth of the sensor is calculated as a function of the probe-to-control laser power ratio, orientation angle and thickness of a phase plate. The theoretical model is proved experimentally.

§4.2 General principles of the sensor operation

4.2.1 The sensor's architecture

The sensor's architecture is sketched in figure 4.1. Two laser beams at widely separated wavelengths, of 633 and 976nm, are mixed by a multiplexer in a single-mode optical fiber. The output radiation from the multiplexer is collimated by a Selfoc lens and the resultant one is launched into a sensitive element composed of a polarizer, a $Bi_{12}TiO_{20}$ crystal, a phase plate and an analyzer. The $Bi_{12}TiO_{20}$ (5 x 5 x 2 mm^3) crystal is cut in such a way that the light propagates in it normally to the [1 0 0] crystallographic plane. Transparent electrodes are deposited on the crystal facets. The longitudinal scheme of the electro-optical modulation is used in the sensor. The radiation transmitted by the sensing element is then focused by another Selfoc lens into a receiving fiber and is detected by a photodiode. Physically, the device is a composition of two sensors operating at the different wavelengths, whose signals are added (or subtracted) at the photodetector. It is essential that the measuring photodiode is simultaneously sensitive to radiation at the mentioned wavelengths, 633 and 976 nm.

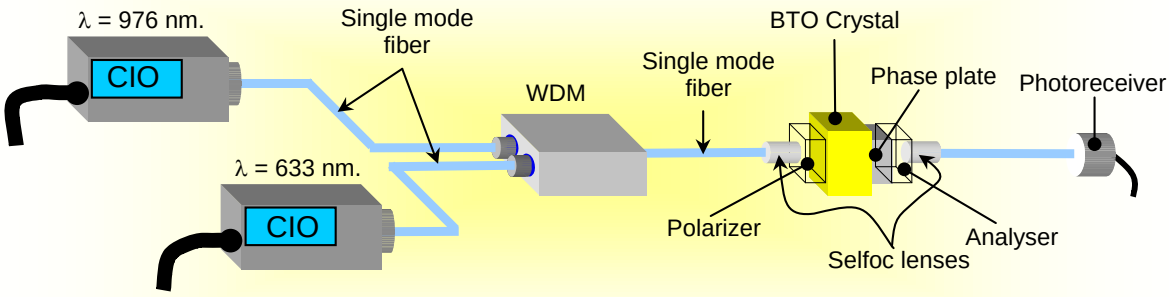

Figure 4.1 Sensor's architecture.

4.2.2 The sensor's transfer function

Exploiting the Jones matrix formalism, the transmittivity of the device T at one of the wavelengths can be written as [8]:

$$T = P \cdot R(-\psi) \cdot W \cdot R(\psi) \cdot R\left(\frac{\pi}{4}\right) \cdot V \cdot R\left(\frac{-\pi}{4}\right) \tag{4.1}$$

where P is the analyzer matrix, $R(...)$ is the rotation matrix, W is the matrix of the phase plate and V is the matrix of the electro-optical crystal subjected to voltage bias (ψ is the angle of the eigenaxes of the phase plate with respect to the reference system).

Assuming the polarizer orientation to be parallel to the axis X of the reference system, and multiplying Equation (4.1) by the vector $\begin{pmatrix} 1 \\ 0 \end{pmatrix}$, one can get the probe radiation intensity, I, at the photodiode as:

$$I = 0.5 + \left(0.5 - \sin^2(2\psi)\cos^2\left(\frac{\Delta}{2}\right)\right)\cos\delta - 0.5\sin(2\psi)\sin\Delta\sin\delta \tag{4.2}$$

where $\delta = \pi n^3 r_{41} U/\lambda$ is the phase shift between the fast and slow waves in the crystal, n is the refractive index of the crystal, $\Delta = 2\pi\Delta nL/\lambda$ and Δn are, respectively, the phase shift and birefringence of the phase plate (L is the phase plate thickness λ is the wavelength of the probe radiation and U is the applied voltage. Assuming a sinusoidal voltage with amplitude $\boldsymbol{U}$ at circular frequency ω one can write the expressions for the photodetector's current corresponding to the direct and first-harmonic components as follows:

$$I_{direct} = 0.5 + \left(0.5 - \sin^2(2\psi)\cos^2\left(\frac{\Delta}{2}\right)\right)J_0(\delta) \tag{4.3}$$

$$I_{\omega} = -\sin(2\psi)\sin(\Delta)J_1(\delta) \tag{4.4}$$

If the two spectral components (the control and the probe ones) are measured by the photodiode, the above formulas are generalized to give:

$$i_{direct} = 0.5 + \frac{\eta_1 P_1}{\eta_1 P_1 + \eta_2 P_2}\left(0.5 - \sin^2(2\psi) \times \cos^2\left(\frac{\Delta_1}{2}\right)\right) J_0(\delta_1) + \frac{\eta_2 P_2}{\eta_1 P_1 + \eta_2 P_2} \times \left(0.5 - \sin^2(2\psi)\cos^2\left(\frac{\Delta_2}{2}\right)\right) J_0(\delta_2) \tag{4.5}$$

$$i_{\omega} = -\frac{\eta_1 P_1}{\eta_1 P_1 + \eta_2 P_2}\sin(2\psi)\sin(\Delta_1) J_1(\delta_1) - \frac{\eta_1 P_1}{\eta_1 P_1 + \eta_2 P_2}\sin(2\psi)\sin(\Delta_2) J_1(\delta_2) \tag{4.6}$$

where η_1 and η_2 are the quantum efficiencies of the photodetector at the wavelengths λ_1 and λ_2, respectively, and P_1 and P_2 are the optical powers of the signals at these wavelengths.
To avoid the influence of the intensity fluctuations on the sensor's operation, one usually uses the modulation depth m as the measured parameter of a sensing device. In the case of two spectral components in the detected signal, this parameter is written as:

$$m = \frac{i_{\omega}}{i_{direct}} = \frac{AP_1 + BP_2}{CP_1 + DP_2} \tag{4.7}$$

where

$$A = \eta_1 \sin(2\psi)\sin(\Delta_1) J_1(\delta_1)$$

$$B = \eta_2 \sin(2\psi)\sin(\Delta_2) J_1(\delta_2)$$

$$C = 0.5\eta_1 + \eta_1\left(0.5 - \sin^2(2\psi)\cos^2\left(\frac{\Delta_1}{2}\right)\right) J_0(\delta_1)$$

$$D = 0.5\eta_2 + \eta_2\left(0.5 - \sin^2(2\psi)\cos^2\left(\frac{\Delta_2}{2}\right)\right)J_0(\delta_2)$$

The modulation depth m is a fractional linear function of the powers P_1 and P_2 (see Equation 4.7). In a single wavelength sensor, the sensitivity does not depend on optical power. In contrary, in the two-wavelength sensor the sensitivity is a function of optical power. Figure 4.2 shows the dependence of the normalized modulation depth on the probe-control power ratio. Varying the power of one of the laser sources, one can change the modulation depth of the useful signal, i.e. the sensor's sensitivity.

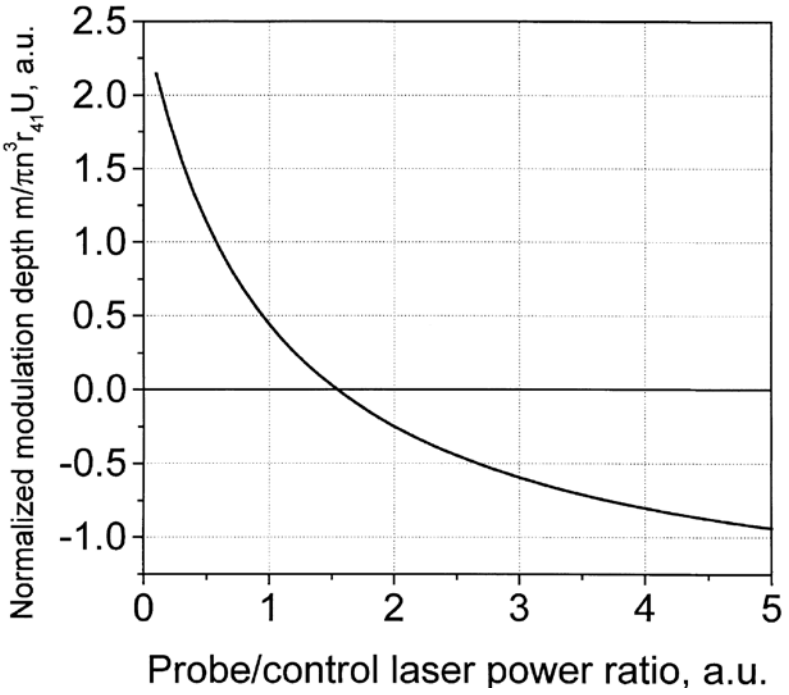

Figure 4.2 Normalized modulation depth as a function of probe-to-control laser ratio. The thickness of phase plate L = 160 μm, $\psi = 45^o$

The properly chosen operating wavelengths as well as the phase plate parameters permit an increase or decrease in sensitivity of the sensor by varying the power of the control signal. In particular, under the condition:

$$AP_1 = -BP_2 \tag{4.8}$$

The sensor's modulation depth is equal to zero (see Figure 4.2). This occurs when the signals at the probe and control wavelengths are counterphase.

4.2.3 The phase plate parameters

As it is seen from the above analysis, the orientation thickness of the phase plate determines the sensor operation features. Thus, the proper choice of these parameters provides a sensor's operation with increased or decreased sensitivity. Consider this problem in detail.

4.2.3.1 Orientation of the phase plate

Suppose that modulation is weak (i.e.,$J_1(\delta_1)\approx\delta_1, J_1(\delta_2) \approx \delta_2$ *and* $J_0(\delta_1)\approx 1$, $J_0(\delta_2)\approx 1$). In this case, Equation 4.7 is transformed to the following one:

$$m \propto \frac{\pi n^3 r_{41} U \sin(2\psi)\left(\frac{\eta_1 P_1}{\lambda_1}\sin\Delta_1 + \frac{\eta_2 P_2}{\lambda_2}\sin\Delta_2\right)}{\eta_1 P_1\left(1-\sin^2(2\psi)\cos^2\left(\frac{\Delta_1}{2}\right)\right)+\eta_2 P_2\left(1-\sin^2(2\psi)\cos^2\left(\frac{\Delta_2}{2}\right)\right)} \qquad (4.9)$$

The results of calculations of the normalized modulation depth $m/\pi n^3 r_{41} U$ as a function of the polarization azimuth ψ for the varying probe-to-control power ratio are shown in Figure 4.3. These data are not surprising: To achieve the maximum modulation depth of the output signal one needs to excite equally the fast and slow waves in the phase plate, providing the azimuth of the input polarization to make the angle of 45° with the phase plate axes.

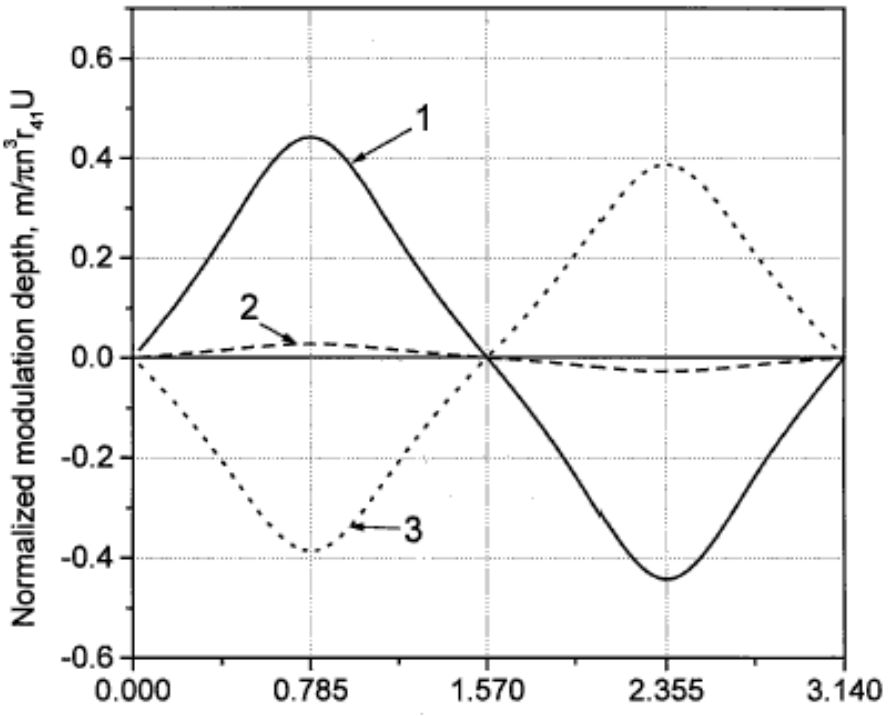

Figure 4.3 Normalized modulation depth as a function of phase plate orientation for different probe-to-control laser ratio: (1) $\eta_1 P_1 = 0.5$, $\eta_2 P_2 = 0.5$; (2) $\eta_1 P_1 = 0.4$, $\eta_2 P_2 = 0.6$; (3) $\eta_1 P_1 = 0.3$, $\eta_2 P_2 = 0.7$.

4.2.3.2. Thickness of the plate

The phase plate thickness is chosen to satisfy some important requirements. First of all, the plate should be as close as possible to a quarter wave plate for the both wavelengths. In addition, in order to decrease the sensor's sensitivity, one needs to full the condition (4.8) (i.e., to compensate the signals corresponding to the probe and control radiation). As it is clearly seen from Equation (4.9), such compensation is possible, if the product sin $\Delta 1 \times$ sin $\Delta 2$ is negative. Figure 5.4 gives an illustration how to choose properly thickness of a mica phase plate. One can conclude from Figure 4.4 that for some range of thickness (from 130 to 200 μm.), the product sin $\Delta 1$ sin $\Delta 2$ is negative. The phase shift between the fast and slow waves in the plate for radiation at the wavelengths of 633 and 976 nm is also shown in Figure 4.4.

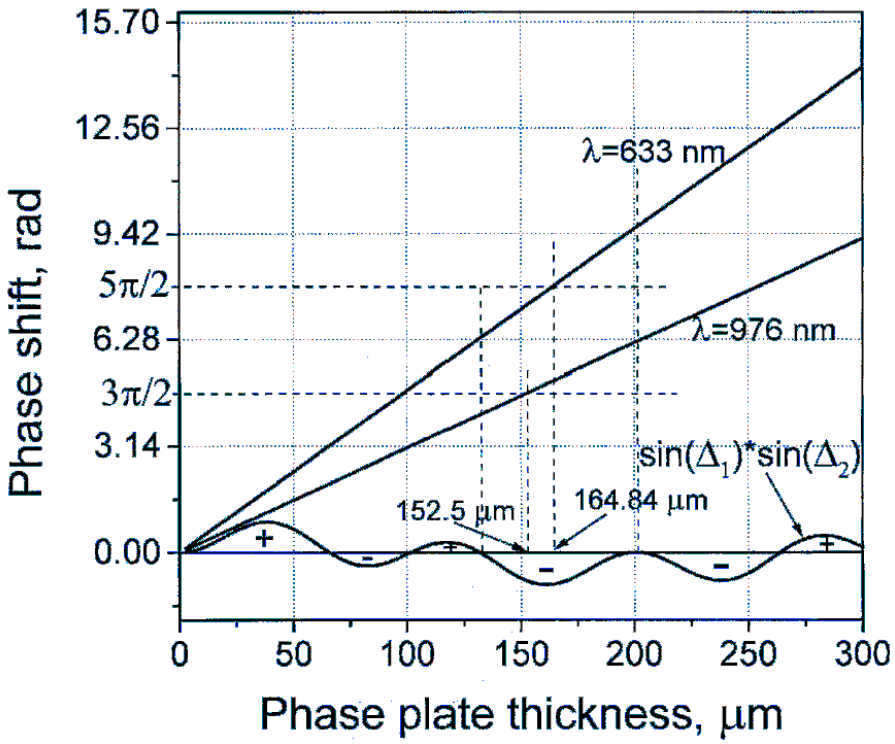

Figure 4.4 Phase shift between slow and fast waves in the phase plate as a function of thickness

The phase plate thickness corresponding to the phase shift of $3\pi=2$ at the wavelength of 976 nm. is about 152.5 μm, whereas that of $5\pi=2$ at the wavelength 633 nm is about 164.8 μm. Basing on these calculations, we used in the experiments (see below) a 160-μm thick mica phase plate. Note that once the probe-to-control power ratio is fixed, one may approach the signals' compensation by the proper changing of the phase plate thickness. Figure 4.5 gives the theoretical dependence of the normalized modulation depth versus the phase plate thickness. The change in sign of the curve corresponds to the change in the signal phase by π.

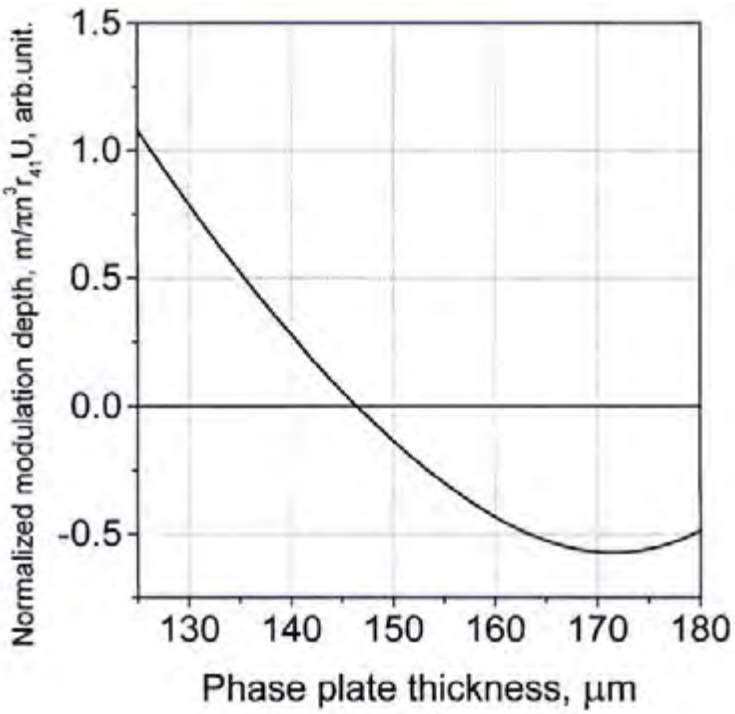

Figure 4.5 Normalized modulation depth as a function of the phase plate thickness.

§4.3 Experimental details

We used in experiments a semiconductor laser (976 nm, of variable output power) as a source of control radiation and a He-Ne laser (633 nm, output power of 55 mW) as a probe one. We studied the modulation depth of the measured signal as a function of the phase plate thickness and power of the control laser.

The first dependence is shown in Figure 4.6. We initially checked the control laser power to find the point of the sensor signals compensation. In these conditions, we were able to vary thickness of the phase plate simply by its tilt with respect to the light beam axis. As it is seen from Figs. 4.5 and 4.6, the theoretical and experimental results are in good qualitative agreement; some deviations could be explained by slight modification of the polarization eigenwaves exiting the biaxial crystal of mica (the phase plate) due to its tilt.

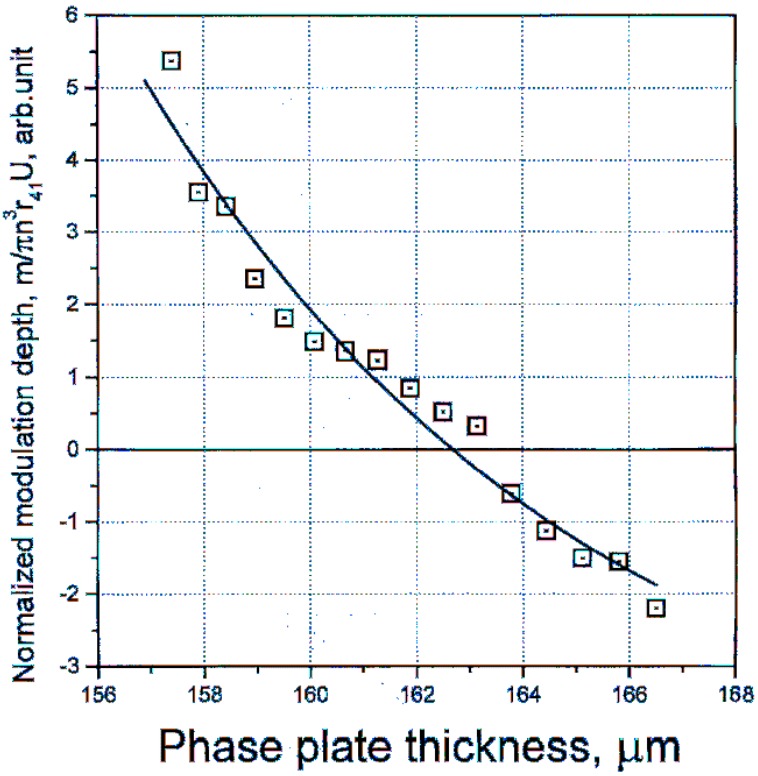

Figure 4.6 Experimental dependence of normalized modulation depth versus phase plate thickness

The dependence of the modulation depth on the power of the control radiation is shown in Figure 4.7. The whole compensation of the useful signal (where sensitivity of the sensor is null) corresponds to 7 μW of the input power. The negative values of the sensitivity in Figure 4.7 reflect the change in the signal phase by π. The experimental data in Figure 4.7 are fitted by a theoretical curve calculated with the use of formula (4.7). One can conclude that there is excellent agreement between the experiment and the theory developed in Section §4.2.

Therefore, varying the power of the controlling beam, one can change the sensitivity of the proposed sensor over wide ranges. The switching response time is determined by inertia of the control laser only.

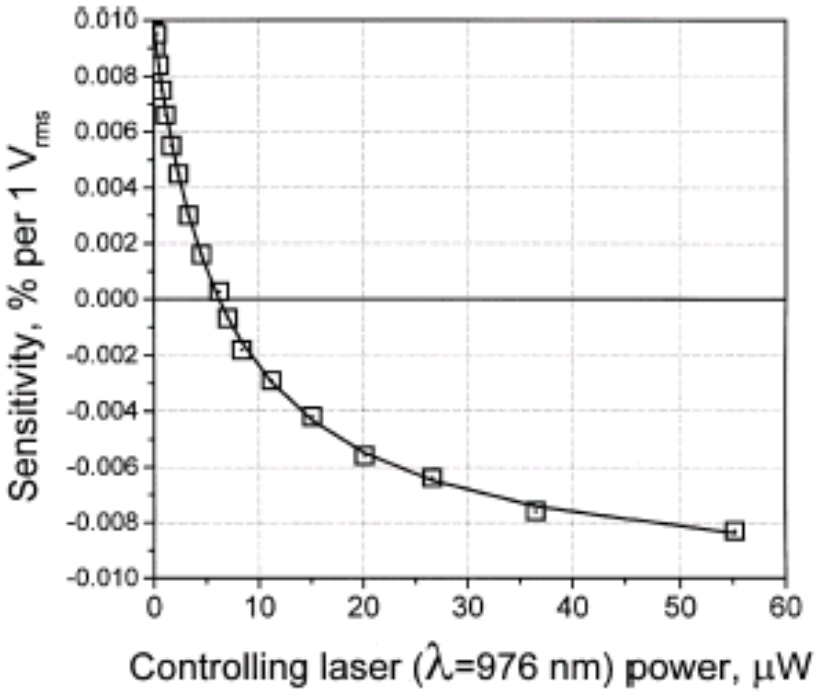

Figure 4.7 The sensitivity of the sensor as a function of the control laser optical power. The solid line approximates the sensitivity under the law $m = (17.56 - 2.84\ P_{976nm}) / (1802.6 + 268.14\ P_{976nm})$% per 1 V_{RMS}

§4.4 Conclusions and remarks

We have presented in detail a fiber-optic voltage sensor operating at the two widely separated wavelengths λ = 633 nm (probe radiation) and λ = 976 nm (control signal) with optically con trolled sensitivity. Modulation depth of the sensor has been calculated as a function of the probe-to-control laser power ratio, orientation angle, and thickness of the phase plate. We have shown that for the maximum modulation depth both waves must be polarised at the angle of π = 4 with respect to the axes of the phase plate. The sensor's sensitivity depends drastically on the phase shifts $\Delta_{1,2}$ introduced by the phase plate for the probe and control wave, respectively. To increase the sensor sensitivity the product sin Δ_1 sin Δ_2 must be positive, while its negative values correspond to the sensitivity decrease. Unlike a single wavelength sensor where the modulation depth does not depend on optical power, the two-

wavelength sensor allows to vary this parameter under the wave power control. We have demonstrated experimentally continuous change of the sensitivity from 0.01% to 0.008% per Vrms varying the control power from 0 to 55 μW (the negative values of sensitivity correspond to the change of p in phase of electric signal). The experimental data obtained are in agreement with the developed theoretical model. The main advantage of the device implemented is a possibility to tune rapidly the sensor's operating range using a weak control optical signal. We believe that the suggested sensor might be an elementary chain of distributed telemetry systems exploiting the fiber-optics architecture.

References

[1] Michael Bordovsky, Franjo Cecelja, Bala Balachandran, "Comparative study of cubic crystals performance in bulk electro-optic sensor for DC and extra low frequency measurements", SPIE vol. **2839**, pp.166-173, (1996).

[2] Yuji Hamasaki, Hideo Gotoh, Masaaki Katoh, Seiichi Takeuchi, "OPSEF : An Optical Sensor for Measurement of High Electric Field Intensity", Electronics Letters vol. **16**, No. 11, pp. 406-407, (1980).

[3] Y. Kuhara, Y. Hamasaki, A. Kawakami, Y. Murakami, M. Tatsumi, H. Takimoto, K. Tada and T. Mitsui, "BSO/Fiber-Optic Voltmeter with Excellent Temperature Stability", *Electron. Lett.*, vol. **18**, No. 24, pp. 1055-1056, (1982).

[4] J. Niewisch, Peter Menke, P. Krammer, Thomas Bosselmann, "Temperature Drift Compensation of a Potential Transformer using a BSO Pockels Cell", *Eleventh International Conference on Optical Fiber Sensors*, *Jpn. Soc. Appl. Phys.*, vol.**WE 1-5**, pp. 152-155, (1996).

[5] Andreas Koch, Christian Helmig and Hartwig Senftleben, "Experimental Studies on a Temperature Compensation for Optical Voltage Sensing", *12th International Conference on Optical Fiber Sensors*, pp.257-260, (1997)

[6] Thomas Bosselmann, “Magneto and Electrooptic Transformers meet expectations of Power Industry”, *from the 12th International Conference on Optical Fiber Sensors, Opt. Soc. Am.*, vol. **16**, pp. 111-114, (1997).

[7] Valery N. Filippov, Andrei N. Starodumov, Vladimir P. Minkovich and Yuri O. Barmenkov, “Optically Controlled Fiber Voltage Sensor”, *IEEE Photonics Technol. Lett.*, vol. **12**, No 7, pp. 870-872, (2000).

[8] Amnon Yariv and P. Yeh, *Optical Waves in Crystals*, 7th Ed.(John Wiley & Sons, New York, 1984).

Chapter Five:

Fiber optic voltage and temperature sensor

§5.1 Introduction

The modern fiber-optic sensors show a tendency to include additional channels for controlling variations of ambient parameters such as temperature and pressure, which often affect an accuracy of measurements. The optical fiber sensors, which can simultaneously measure temperature and mechanical stress [1–3], electrical current and voltage [4] have been reported. Rose and Day [5] have proposed to combine in one package simultaneously two sensors, with the purpose to use the data of the temperature sensor for correcting the signal of the voltage sensor. The plate of crystal quartz with temperature-dependent birefringence was used as a sensing head of the temperature sensor. It should be noted that all fiber-optic sensors of an electrical voltage include a crystal phase plate [6], which usually is the main reason of sensor's temperature instability [7].

In this chapter we propose a new configuration of the fiber optic voltage sensor based on the $Bi_{12}TiO_{20}$ crystal, which allows simultaneous measurement of both voltage and temperature. In contrast to previously reported sensor where a separate temperature sensor was added to the scheme, we use the quarter wave plate of the voltage sensor as a temperature sensitive element. In this case, the phase plate simultaneously provides two functions: serves as a phase shifting element in the voltage sensor and as a sensitive element of the temperature sensor. This permits to decrease the size of the sensing head and to avoid and additional temperature sensor.

§5.2 Basic principle of the sensor

The optical scheme of the sensor shown in Figure 5.1, in general is similar to that described earlier in Ref. 8, we used a thick (1.932 mm.) phase retarding plate, made of crystalline quartz (earlier we had used a thin mica-made plate). An additional WDM has been included in the scheme to separate output signals at two wavelengths. The $Bi_{12}TiO_{20}$ crystal and the phase plate were placed on a thermoelectric element to vary temperature of the sensor's head. After wavelength demultiplexing in a WDM, the signals at two wavelengths, being separated into two channels, are detected by photoreceivers. The two output signals from the photoreceivers are sent directly to an electronic processing unit. It should be noted that two output signals from the photoreceivers are proportional to the voltage applied to the crystal and depend on temperature of the sensor.

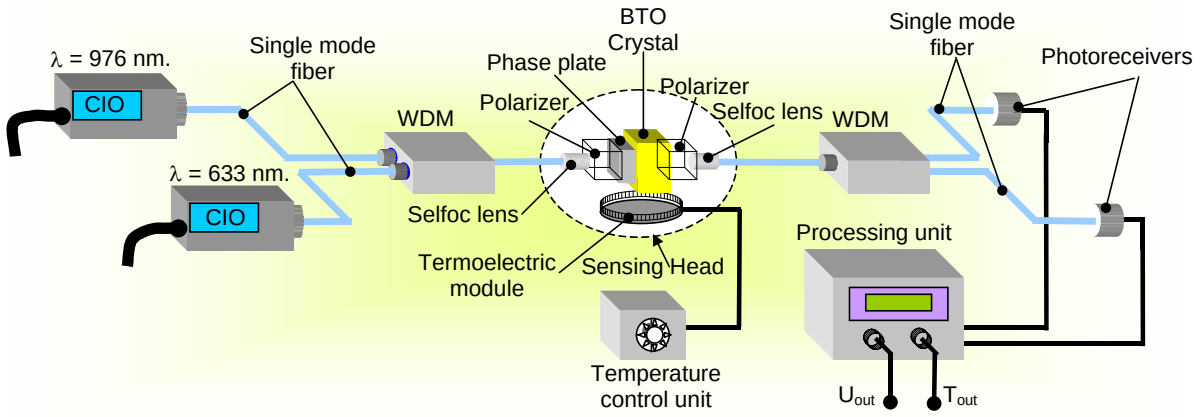

Figure 5.1 Schematic diagram of the sensor.

Let consider the operation of this sensor. Neglecting optical activity of a $Bi_{12}TiO_{20}$ crystal, it is easy to show that the current through the photoreceiver load corresponding to the power at wavelength λ_1 is given by [9]:

$$i \propto P_1 \cdot \sin^2\left(\frac{\pi n_1^3 (r_{41})_1 U}{\lambda_1} + \frac{2\pi \cdot \Delta n_1 \cdot L}{\lambda_1}\right) \qquad (5.1)$$

where P_1 is the optical power at λ_1; n_1 is the refractive index of the crystal at λ_1; Δn_1 is the difference between the refractive indices of the fast and slow axes at λ_1; $(r_{41})_1$ is the electrooptic constant at λ_1; L is the phase plate thickness; and U is the voltage applied to the crystal.

Assuming that the voltage applied to the crystal varies harmonically with amplitude U_0 and frequency Ω, and introduces small phase variations ($\ll \pi$), we can expand the Equation 5.1 into Fourier series. Then, the amplitudes of the first harmonic and of the direct component of a current I are described as:

$$I_{DC} \propto P_1 \cdot \left(1 - \cos\left(\frac{2\pi \cdot \Delta n_1 \cdot L}{\lambda_1}\right) \cdot J_0\left(\frac{\pi n_1^3 r_{41} U_0}{\lambda_1}\right)\right) \tag{5.2}$$

$$I_{\Omega} \propto P_1 \cdot \sin\left(\frac{2\pi \cdot \Delta n_1 \cdot L}{\lambda_1}\right) \cdot J_1\left(\frac{\pi n_1^3 r_{41} U_0}{\lambda_1}\right) \tag{5.3}$$

Modulation depth of an optical signal, which is usually measured as a sensor's signal [10], can be written as:

$$m_1 = \frac{I_{\Omega}}{I_{DC}} = \frac{\sin\left(\frac{2\pi \cdot \Delta n_1 \cdot L}{\lambda_1}\right) \cdot J_1\left(\frac{\pi n_1^3 r_{41} U_0}{\lambda_1}\right)}{1 - \cos\left(\frac{2\pi \cdot \Delta n_1 \cdot L}{\lambda_1}\right) \cdot J_0\left(\frac{\pi n_1^3 r_{41} U_0}{\lambda_1}\right)} \tag{5.4}$$

Using an approximation $J_0(x) \approx 1$ and $J_1(x) \approx x$ for $x << 1$, the expression (5.4) can be rewritten as

$$m_1 = \frac{\pi \cdot n_1^3 \cdot (r_{41})_1 \cdot U_0}{\lambda_1} \cdot c\tan\left(\frac{\pi \cdot \Delta n_1 \cdot L}{\lambda_1}\right) \tag{5.5}$$

The expression (5.5) is also valid for the second wavelength. We will analyze the ratio of the modulation depth at two wavelengths which is given by

$$\frac{m_1}{m_2} = \frac{(r_{41})}{(r_{41})} \cdot \left(\frac{n_1}{n_2}\right)^3 \cdot \frac{\lambda_2}{\lambda_1} \cdot \frac{c\tan\left(\frac{\pi \cdot \Delta n_1 \cdot L}{\lambda_1}\right)}{c\tan\left(\frac{\pi \cdot \Delta n_1 \cdot L}{\lambda_2}\right)} \tag{5.6}$$

As follows from Eq. (5.6), the ratio m_1/m_2 does not depend on voltage applied to the sensor, but depends on temperature. The temperature-dependent variations of the phase shift between fast and slow waves in the phase plate are given by [11]

$$\delta\left(\frac{\Delta n_{1,2} \cdot L}{\lambda_{1,2}}\right) = \frac{1}{\lambda_{1,2}} \cdot \left(L \cdot \frac{\partial \Delta n_{1,2}}{\partial T} + \Delta n_{1,2} \frac{\partial L}{\partial T}\right) \cdot \Delta T \tag{5.7}$$

Assuming $(\partial L/\partial T)$ = 13.37·10^{-6} C^{-1}, Δn_{633} = 0.00906, Δn_{976} =0.0088, $(\partial \Delta n_{1,2}/\partial T)$ = -1.04·10^{-6} C^{-1}[11], we have calculated the ratio of the modulation depths as a function of temperature (Figure 5.2). In this model, we neglected the temperature sensitivity of a $Bi_{12}TiO_{20}$ crystal, because the optical activity of $Bi_{12}TiO_{20}$ is insignificant (1.5° mm^{-1}) and rather stable (-2·10^{-4} K^{-1}) [10], and the temperature sensitivity of the electro-optical constant r_{41}(2·10^{-4} K^{-1}) is rather low [10].

As follows from Figure 5.2, the temperature dependence of the modulation depths ratio is uniquely determined, monotonous, weakly non-linear, providing a suitable gauging curve for the temperature sensor. Calculating temperature from this curve and taking into account Equation 5.5, one can easily determine a correct value of the applied voltage using the following equation:

$$U_0 = \frac{m_1(T) \cdot \lambda_1}{\pi \cdot n_1^3 \cdot (r_{41})} \cdot \tan\left(\frac{\pi \cdot \Delta n_1(T) \cdot L(T)}{\lambda_1}\right) \tag{5.8}$$

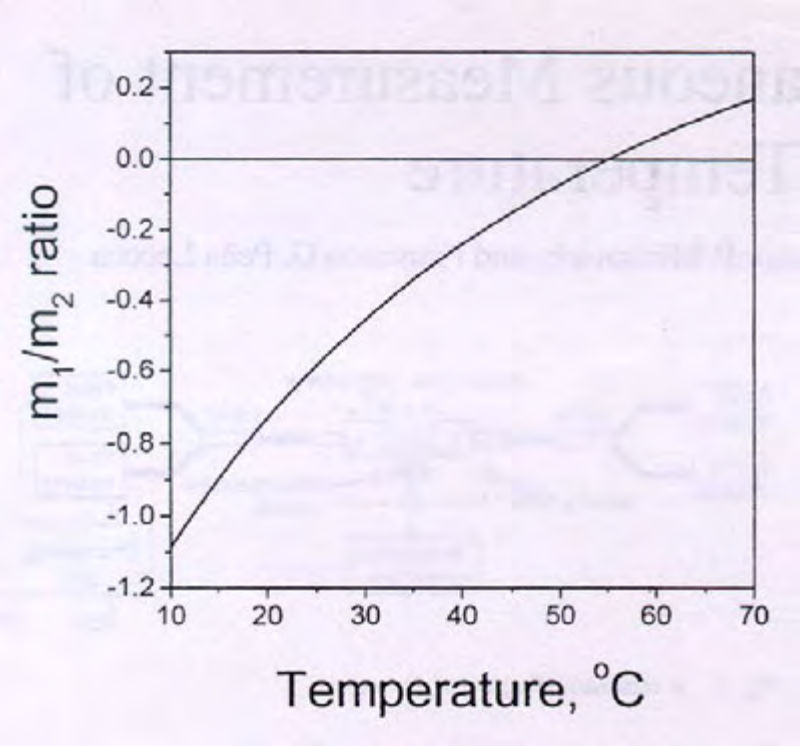

Figure 5.2 Modulation depth's ratio as a function of temperature. The thickness of the quartz phase plate is 1.932 mm.

The advantage of such a voltage sensor besides of compactness and multifunctionality is the high temperature stability. The reason is that the measured data correspond to the real temperature of the voltage sensor.

§5.3 Experimental details

The temperature dependence of the modulation depth was investigated experimentally for both channels. Figure 5.3 shows the results of the experiment. As follows from the experimental data, the modulation depth dependence on temperature has a ctang-like shape for both wavelengths that well agree with the theoretical model (see Eq. 5.5). The transition through the zero value corresponds to the change of π radian in the phase of a sensor's signal.

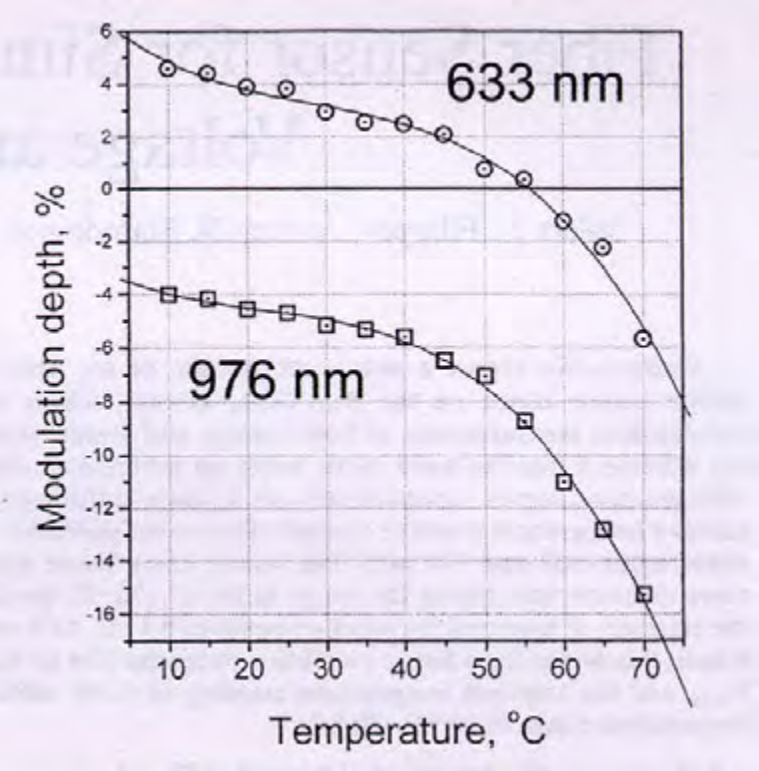

Figure 5.3 Experimental dependence of the modulation depth versus temperature for λ = 633 nm and λ = 976 nm

The temperature dependence of the ratio of modulation depths for two wavelengths is shown in Figure 5.4. As is seen, experimental results are in agreement with the theoretical model. A difference between theoretical and experimental curves (experiment-linear dependence, theoretical model-non linear function) could be explained by the simplifications accepted in the theoretical model. In particular, the contribution of the first harmonic is only taken into account in the Equation 5.4. The temperature dependence of the electrooptic coefficient may also change the theoretical curve.

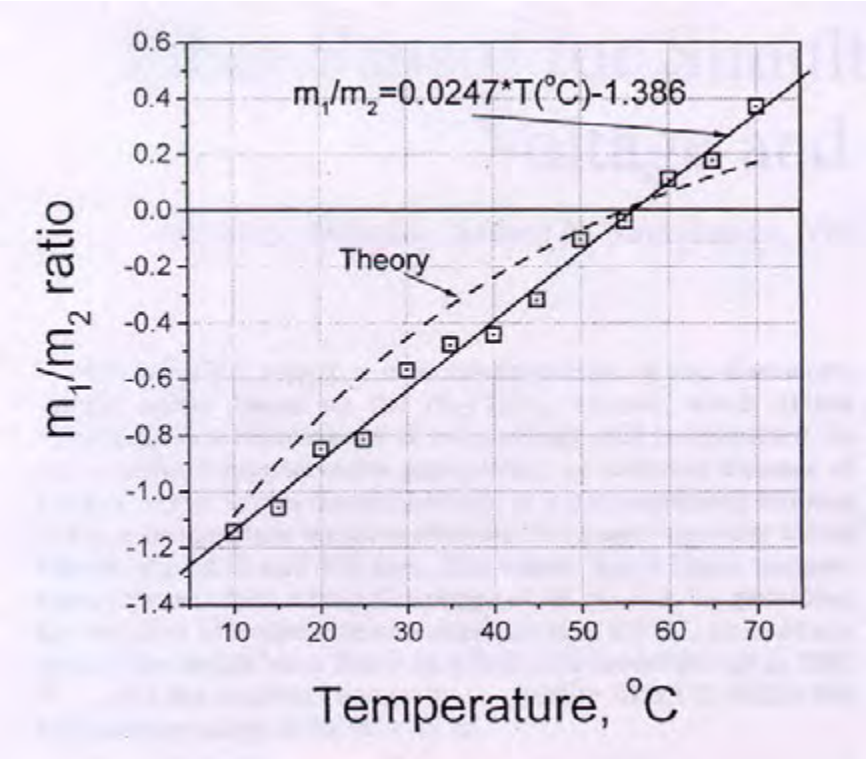

Figure 5.4 Modulation depth's ratio as a function of temperature. Experimental results.

We have estimated an accuracy of temperature measurements in the range of 10 °C – 70 °C. Since the sensor's temperature is calculated from the measured ratio of modulation depths, the error of measurements of four voltages $U_{633/DC}$, $U_{633/AC}$, $U_{976/DC}$, U_{976AC}, was 10^{-4} will determine the total error of measurement. In its turn, the accuracy of voltage measurements is determined by the noise of optical sources and photoreceivers. The relative error of the voltage measurements $U_{633/DC}$, $U_{633/AC}$, $U_{976/DC}$, U_{976AC} was 10^{-4} in our experiments. The relative error of the temperature measurement was calculated to be 10^{-3}. As a result, the absolute error of temperature measurement is approximately 0.3 °C (within 10 °C – 70 °C). The absolute error of the voltage measurement was 1 V_{rms} (within 20 – 1000 V_{rms}), providing the accuracy of the voltage measurements of about 0.1 % within the temperature range of 10 °C – 70 °C.

The sensitivity of the voltage sensor was measured to be 0.008 % per 1 V_{rms} at 20 °C. This is a little less, than the sensitivities reported before in the literature [5,10,12]. It could be explained by the fact, that the phase plate is not precisely a quarter wave for both wavelengths.

The thickness of the phase plate was chosen to supply a sufficient accuracy of the temperature sensor. The amplitude characteristic of the voltage sensor is linear up to 1000 V_{rms}. Minimally detecting voltage is 20 V_{rms} with the resolution about 1 V_{rms}.

§5.4 Conclusions and remarks

The $Bi_{12}TiO_{20}$-based fiber-optic sensor of an electrical voltage and temperature has been demonstrated experimentally. We have proposed to use a thick phase plate of the voltage sensor as a temperature sensitive element. Such a scheme of the sensor allows us, first, to solve a problem of temperature stability of the voltage sensor; second, to decrease the size of the sensing head; and third, to avoid an additional temperature sensor. The sensor has a linear temperature characteristic within the range of 10 °C – 70 °C, providing the accuracy of temperature measurements of 0.3 °C. As a voltage sensor, this device has a linear amplitude characteristic up to 1000 V_{rms} and the excellent temperature stability of 0.1% within the temperature range of 10 °C – 70 °C.

References

[1] A. Frank, P. Nellen, and U. Sennhauser, “Novel methods for simultaneous strain and temperature measurements with optical fiber Bragg gratings”, *in Proc. SPIE Fiber Optic Sensor Technology and applications*, vol. **3860**, M. Marcus and B. Culshaw, Eds., pp 89-97, (1999)

[2] P. M. Cavaleiro, F. M. Araujo, L. A. Ferreira, J. L. Santos, and F. Farahi, “Simultaneous measurements of strain and temperature using Bragg gratings written in germanosilicate and boron-doped germanosilicate fibers”, *IEEE Photonics Technol. Lett.*, vol. **11** pp. 1635-1637, (1999).

[3] J. Tapia-Mercado, A. V. Khomenko, R. Cortes-Martínez, and M. A. García-Zarate, "High accurate fiber sensor with two-LED light source", *Opt. Comm*., vol. **177**, pp. 219-223, (2000).

[4] Wang Zhaobing, Liao Yanbiao, Lai Shurong, Zhao Huafeng, "Fiber Sensor for Simultaneous Measurement of Current and Voltage by single Lo-Bi fiber", in Fiber Optic Sensors V, *Proceedings SPIE*, vol. **2895**, pp. 26-32, (1996).

[5] Allen H. Rose and Gordon W. Day, "Optical fiber voltage sensors for broad temperature ranges", in Fiber Optic Components and Reliability, *Proceedings SPIE*, vol. **1580**, pp. 95-103, (1992).

[6] Michael Bordovsky, Franjo Cecelja, Bala Balachandran, "Comparative study of cubic crystals performance in bulk electro-optic sensor for DC and extra low frequency measurements", *in Fiber Optic and Laser Sensors – XIV, Proceedings SPIE,* vol. **2839**, pp.166-173, (1996).

[7] P. D. Hale and G. W. Day, "Stability of birefringent linear retarders (waveplates)", *Appl. Opt*., vol. **27**, pp. 5146-5153, (1988).

[8] Francisco G. Peña-Lecona, Valery N. Filippov, Andrei N. Starodumov and Alexander V. Kir'yanov, "Fiber Optic Voltage Sensor with Optically Controlled Sensitivity", *Opt. Comm*., vol. **1**, No. 187, pp. 135-140, (2001).

[9] Amnon Yariv and Pochi Yeh, *Optical Waves in Crystals*. (John Wiley and Sons, New York, 1984).

[10] J. Niewisch, Peter Menke, P. Krammer, Thomas Bosselmann, "Temperature Drift Compensation of a Potential Transformer using a BSO Pockels Cell", Eleventh International Conference on Optical Fiber Sensors, *Jpn Soc. Appl. Phys*., 1996, pp. 152-155.

[11] W. G. Driscoll and W. Vaughan, Editors, *Handbook of Optics*. (McGraw-Hill, New York, 1978).

[12] Valery N. Filippov, Andrey N. Starodumov, Yuri O. Barmenkov and Vladim V. Makarov, "Fiber Optic Voltage Sensor Based on a $Bi_{12}TiO_{20}$ crystal", *Appl. Opt*., vol **39**, No. 9, pp. 1389-1393, (2000).

Chapter Six:

Electro-optic fiber optic sensor for high a.c. voltage measurements

§6.1 Introduction

Traditional techniques for high voltage measurements include electrostatic voltmeters, sphere gaps, transformer and potential divider methods. Electrostatic voltmeters have the inconvenient of the difficult to design because they will be free from errors due to corona effects, within the instrument and to the external electrostatic fields. On the other hand, sphere gaps are reliable only for calibration purposes because they need a high accuracy in the gap distance between spheres used and are not suitable for routine measurements. Finally, transformer and potential divider methods are rough and with low accuracy due the undesirable currents [1].

Fiber optic electric field sensors based on electro-optic modulators are attractive for high voltage measurement applications because they offer great advantages with respect of traditional techniques [2,3]. The absence of any conducting element let us obtain advantages like electrical isolation for example, and immunity to electromagnetic interference and electrical and thermal noise.

Pockels electro-optic effect application to sensing electric field was demonstrated long time ago [4]. The first voltage sensor using fiber-optic technology was proposed many years ago [5-12]. Since then, other authors have been proposed several configurations for electric field sensor based on the longitudinal Pockels effect but they do not offer good sensitivity without the use of an additional temperature control channel (0.039% per 1 V_{rms} and 0.051% per 1 V_{rms} [8,12]). Moreover, for industrial applications, temperature stability of the crystal

parameters is not meet at all. For this case, we develop a voltage sensor without temperature control described below.

A fiber optic voltage sensor based on the longitudinal Pockels effect using a $Bi_{12}TiO_{20}$ crystal has been proposed, with good sensitivity (0.145% per 1 V_{rms}) and temperature stability (±1.5% from –20 ^{o}C to 60 ^{o}C) [13, 14]. This electric field sensor showed in Figure 1, was implemented and inserted in a cylindrical non-conductive cover with dimensions of 39 millimeters of length and 13 millimeters of diameter, coupling 100 meters of multimode fiber to it. We report on the application and the response of this sensor for high voltage measurements using two possible forms available of high electric field: continuos electric wave and pulsed electric wave. Our aim is to show that the sensor behavior is linear and that this sensor can be useful for high voltage sensing for industrial applications.

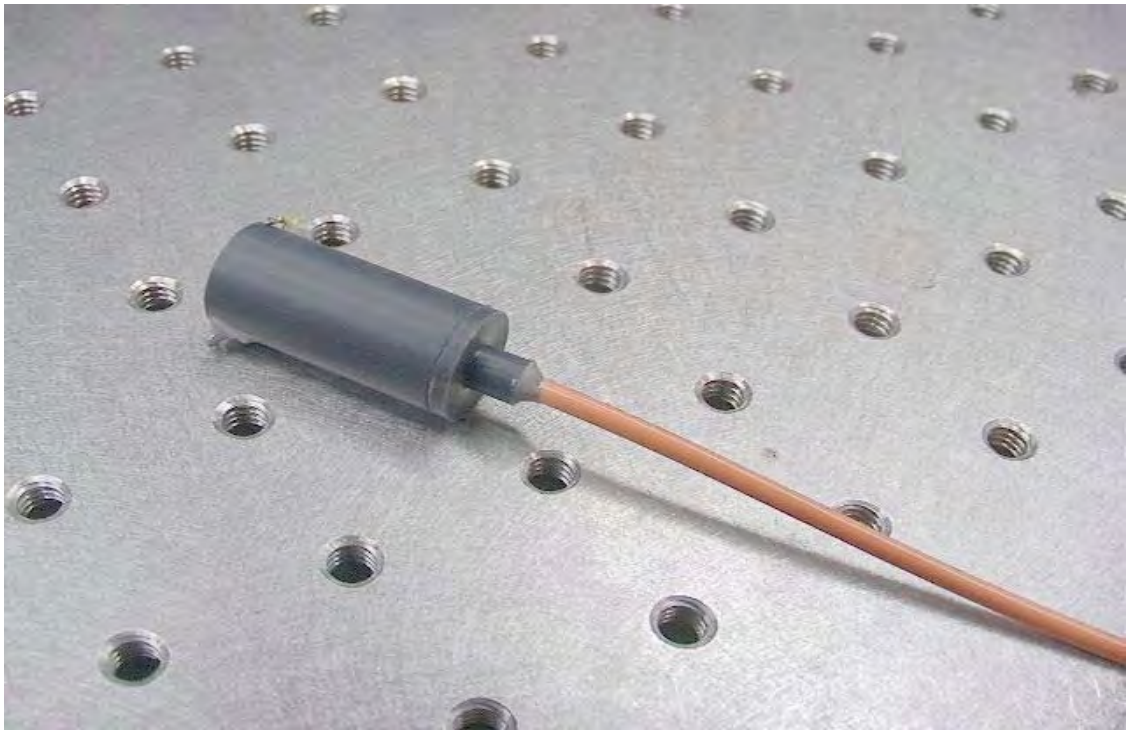

Figure 6.1 Fiber optic electric field sensor.

§6.2 Sensor's Scheme

Figure 6.2 shows an experimental arrangement of the remote sensor proposed to measure high voltage in electric transmission lines. An optical beam from a 670-nm non-polarized superluminiscent light emitting diode (SLED SUPERLUM^{TM} SLD-26-HP with FHWM 30 nm and 5mW was used as the illumination source with a temperature and current controller PILOT-2^{TM} both placed in the processing unit. The SLED's beam is guided through a multimodal fiber (100 m of length and 62.5 / 125 μm) with a Selfoc lens at the end to couple it to the sensor head. The output irradiance is guided backward by means of an identical system (Selfoc-fibre optic) to the processing unit. The sensor head is divided into thre main parts. The first one is a polarizing prism, which has two functions inside the sensor, i. e. , it acts as the polarizer (when the light wave gets in in the sensor head) and as analyser (when the light gets out of it). When the light wave enters into the sensor head, the polarizing prism polarizes the light lineally with an angle of 45 degrees with respect to the BTO's transmission axes and the output irradiance decreases in half. When the light wave leaves the sensor head, the polarizing prism transforms the polarization modulation into amplitude modulation. The second part of the sensor head is composed of a BTO ($5 \times 5 \times 2$ mm^3) photorefractive crystal. This crystal shows isotropic optical properties in the absence of an external electric field. However, the BTO changes its dielectric properties in the presence of an external electric field, that is, it becomes anisotropic showing an induced birefringence[14]. Therefore, a phase diference that is lineally proportional to the external electric field is introduced between the two components of the light that spreads inside the crystal. This phenomenon is the Pockels effect [14]. The third element of the sensor head is a back reflecting prism. The back reflecting prismhas three functions inside the sensor head: (1) to make a double pass through the BTO crystal thereby increasing the sensitivity of the voltage measurement [14]; (2) to introduce a $\pi/2$ rad phase difference, by double reflection to generate a linear response; (3) to avoid a phase shift of the wavelength due to variations of the environmental temperature, the back reflecting prism is made of BF-7 russian glass [15].

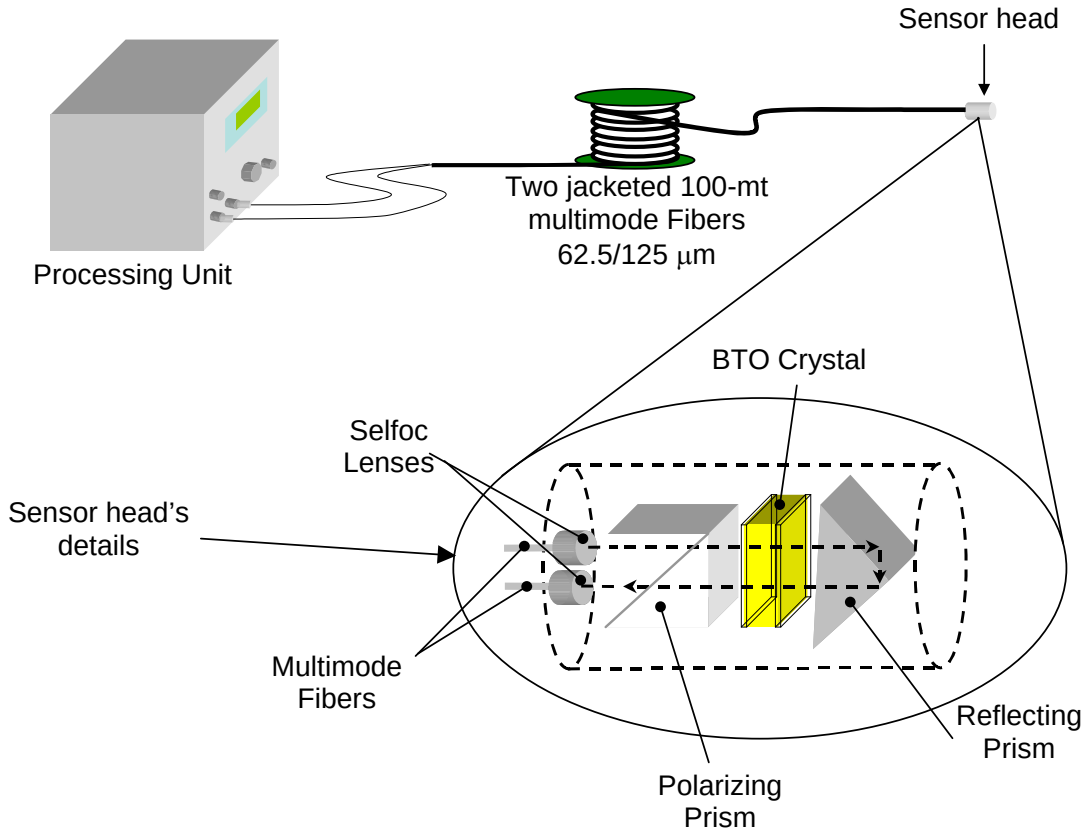

Figure 6.2 Scheme of the fiber optic voltage sensor.

The transmission function of the sensor can be obtained from the 2×2 Jones matrix formalism of each element of the sensor head as [15],

$$I = \left| P \times R(-45^o) \times C_{ref} \times R(45^o) \times R(-45^o - \vartheta) \right.$$
$$\times W \times R(45^o + \vartheta) \times R(-45^o) \times C_{inc}$$
$$\left. \times R(45^o) \times E \right|^2 \qquad (6.1)$$

where, E denotes the Jones vector of light at the input of the crystal after the polarizer, $R(...)$ is the rotation matrix, C_{inc} is the Jones matrix of the BTO crystal for the incident light, W is the Jones matrix of the back-reflecting prism, C_{ref} is the Jones matrix of the BTO crystal for back-reflected light and P is the Jones matrix of the analyzer.

Figure 6.3 shows the sensor's transmission function and the phase shift due the back-reflecting prism. Notice that this is necessary to work the sensor in the linear part of the transmission function. Therefore, we obtain a good linear behavior in the sensor response. It is shown in Figure 6.3, where the intensity of light is being modulated by the electric field imposed to the crystal in the linear part of the transmission function. We used the double pass configuration for high sensitivity proposed in Ref. 13.

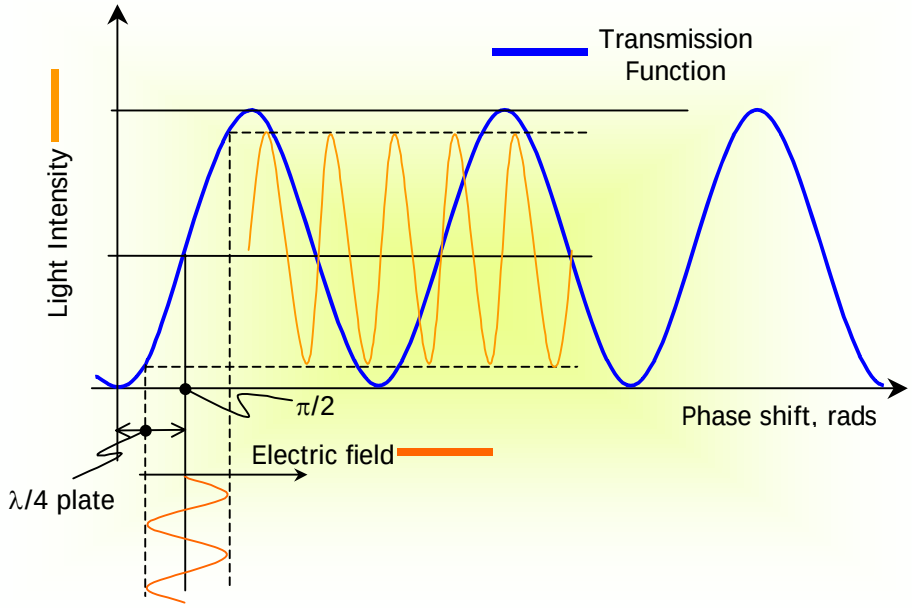

Figure 6.3 Sensor's transmission function.

§6.3 Experimental details

To demonstrate the feasibility of our fiber optic voltage sensor for measuring high voltage, two experiments were performed. The experiments were directed to calculate the sensitivity, linearity and speed of the response of the sensor. Sensor head's response depends of the orientation inside the electric field (Figure 6.4), having the highest sensitivity when the electric field vector is normal to the circular surface of the sensor head (*x*-*y* plane in Figure 6.4).

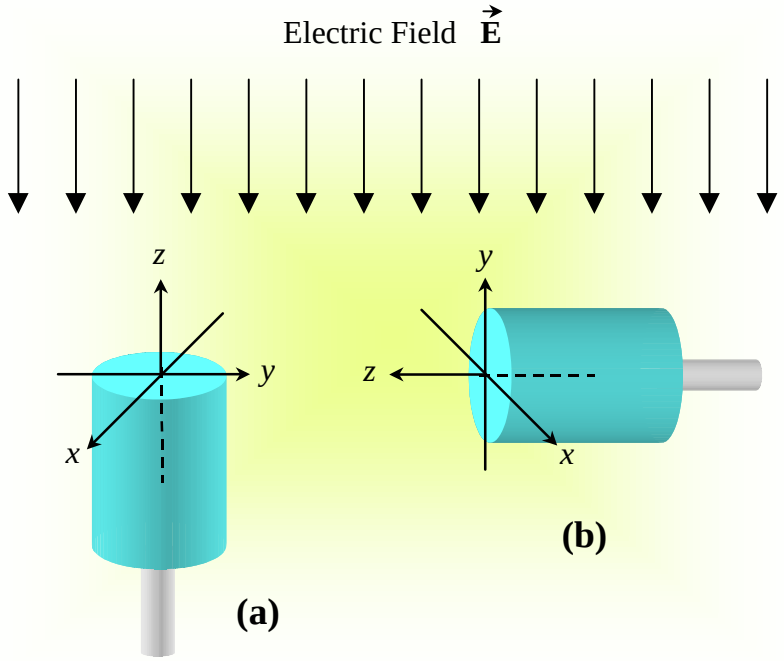

Figure 6.4 Electric field incidence over the plane surface of the sensor head: (a) normal to the *x-y* plane, (b) parallel to the *x-y* plane.

Sensor's response for several degrees of electric field's vector incidence were measured and plotted in Figure 6.5. We can observe that in normal incidence to the *x-y* plane we have the highest amount of electrical modulation. It is obvious if we consider that the optical modulator used in our sensor's configuration was designed to work like a longitudinal modulator [15].

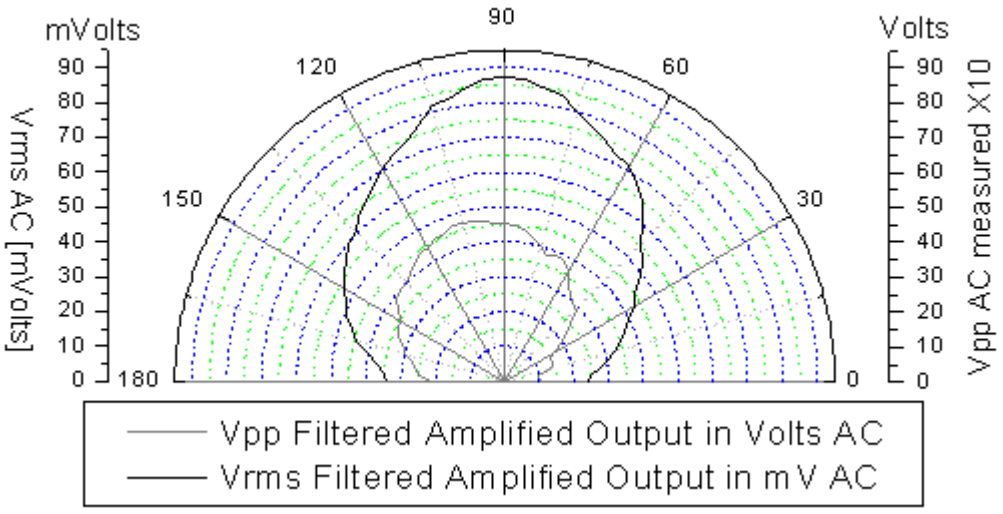

Figure 6.5 Filtered amplified output vs. electric field vector incidence for x-y plane at sensor's head.

Sensor's sensitivity is defined by the ratio of the output voltage sensor in mV to the voltage signal measured. That is:

$$\text{Sensitivity} = \frac{V_{sensor}[mV]}{V_{measured}[kV_{rms}]} \tag{6.2}$$

Where V_{sensor} is the filtered and amplified output of the photodetector when voltage is sensed by the sensor head in milivolts and $V_{measured}$ is the real voltage applied to the aluminum tube in kilovolts.

We define horizontal plane like the parallel plane to the physical ground that includes the sensor element and the voltage element V(t), and the vertical plane like the perpendicular plane to the physical ground that includes the sensor element V(t) (Figure 6.6). Next, we start to explain the experiments realized.

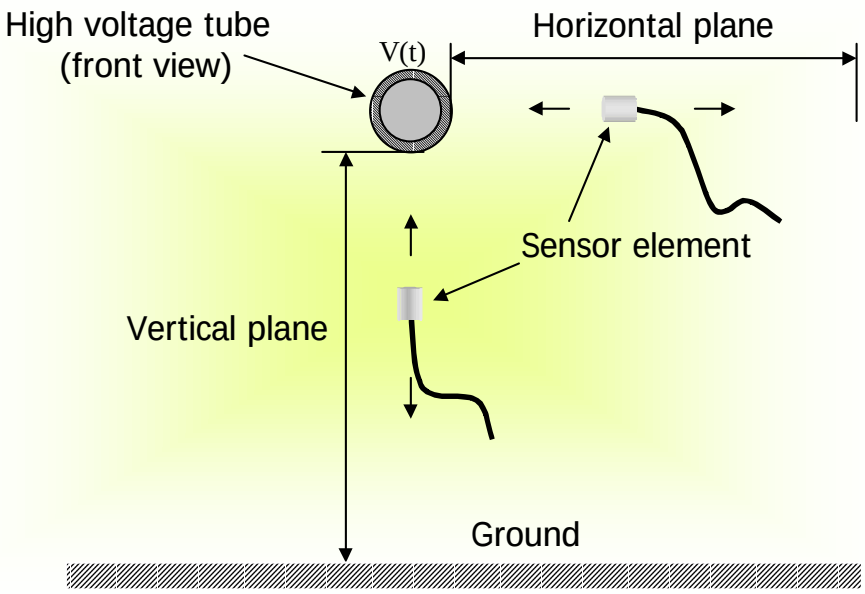

Figure 6. 6 Schematic view of the horizontal and vertical planes.

6.3.1 Continuos electric wave experiments

In the first experiment, a periodic signal of 60 Hz of high ac voltage was measured. For this, a cylindrical conductor of aluminum tube with 15 cm of diameter, was connected to a high voltage source that can be adjusted to vary voltage from 0 to 500 kV by means of transformers. Then the sensor's sensitivity was obtained by changing the distance every 10 cm between the sensor head and the cylindrical conductor in two mutually perpendicular directions.

Sensor sensitivity for horizontal/vertical displacement was measured and plotted in Figure 6.7. Making an approximation, the sensor's sensitivity in horizontal/vertical plane is given by the next calibration equation:

$$Sensitivity = 10^{-6} \times \left(0.941 + \frac{0.083}{d^2\,[\,mts\,]} \right) \tag{6.3}$$

Figure 6.7 shows the approximated sensitivity curve (calibration) in continuous line and measurements in horizontal and vertical planes are shown in dots. Sensitivity is very similar for vertical and horizontal planes. It is because the system has a cylindrical symmetry for the electric field originated by the voltage element [16]. Therefore, measurements made with this sensor assure us that it can be taking only with the consideration that the *x-y* plane must be perpendicular to the electric field to be measured.

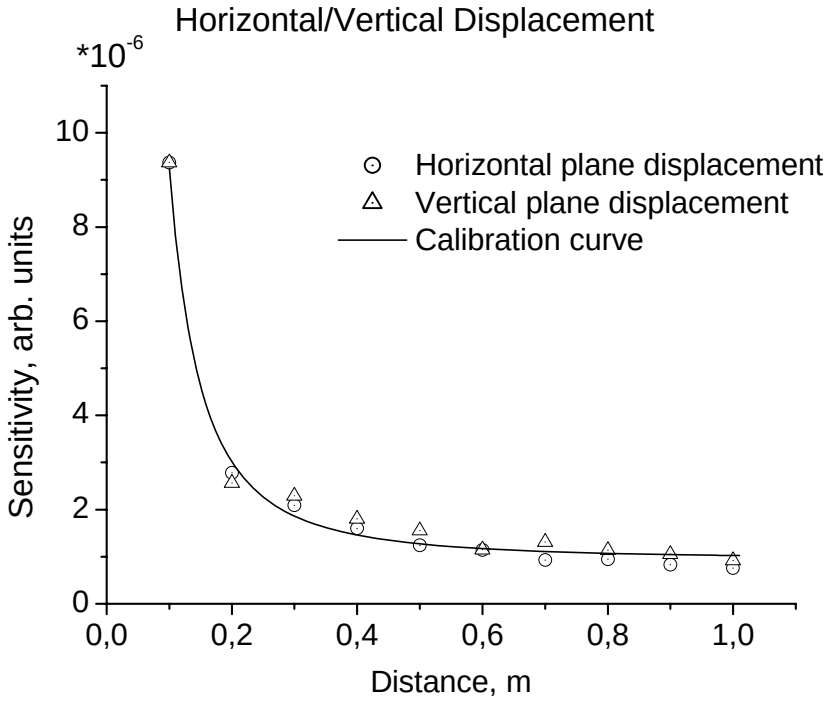

Figure 6.7 Sensor's sensitivity for horizontal and vertical planes.

Sensor's response is linear for each voltage amplitude signal. Figure 6.8 shows variations of the output signal for every 10 centimeters from the voltage element V(t) in horizontal plane with offset view; we can see the slope for each measurement and the dependence with the distance for intensity measurements in range of 50 kV to 400 kV/60 Hz.

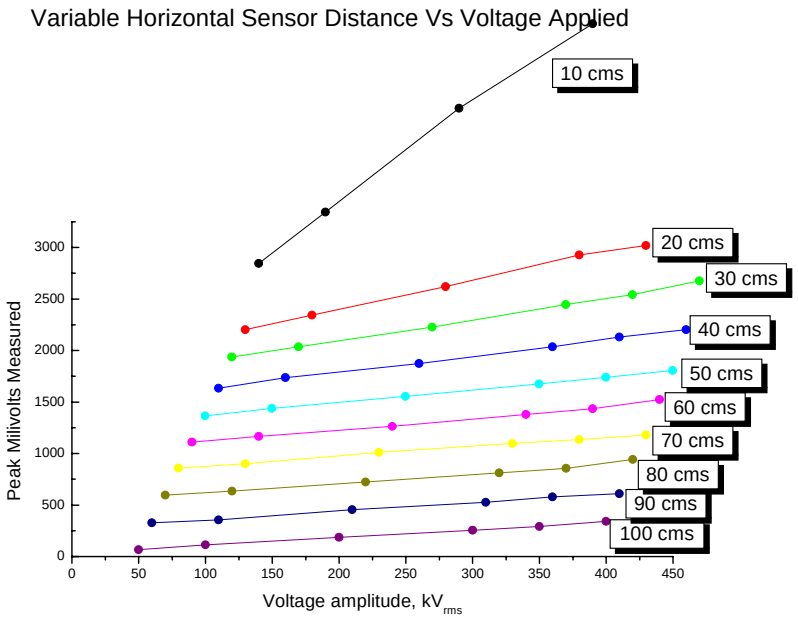

Figure 6.8 Horizontal distance of the sensor from the voltage element Vs. voltage applied (in offset view).

As we can see in figure 6.9, sensor's sensitivity has a similar behavior as horizontal plane, we made measurements from the voltage element V(t) for each 10 centimeters in vertical plane and all are plotted in this figure.

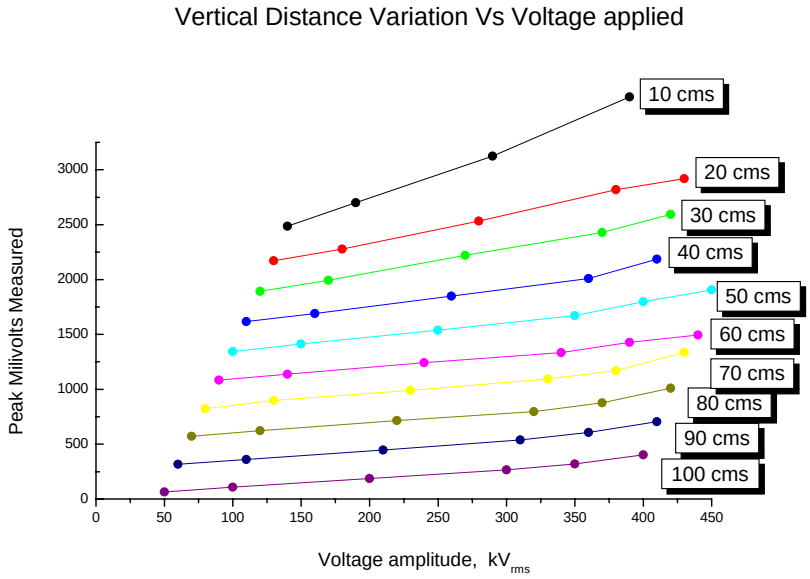

Figure 6.9 Vertical distance of the sensor from the voltage element Vs. voltage applied.

Therefore, voltage measured for a horizontal/vertical displacement directly results:

$$V_{measured}[kV] = 10^6 \times \frac{Vsensor[V]}{\left(0.941 + \frac{0.083}{d^2[mts]}\right)} \tag{6.4}$$

6.3.2 Pulsed electric wave experiments

We also determine the transient response of the fibre optic sensor for several high voltage impulses, with the sensor head at 1 meter away from the cylindrical conducting element V(t). Were applied high voltage pulses from 500 kV to 1100 kV/60 Hz. (Figure 6.10).

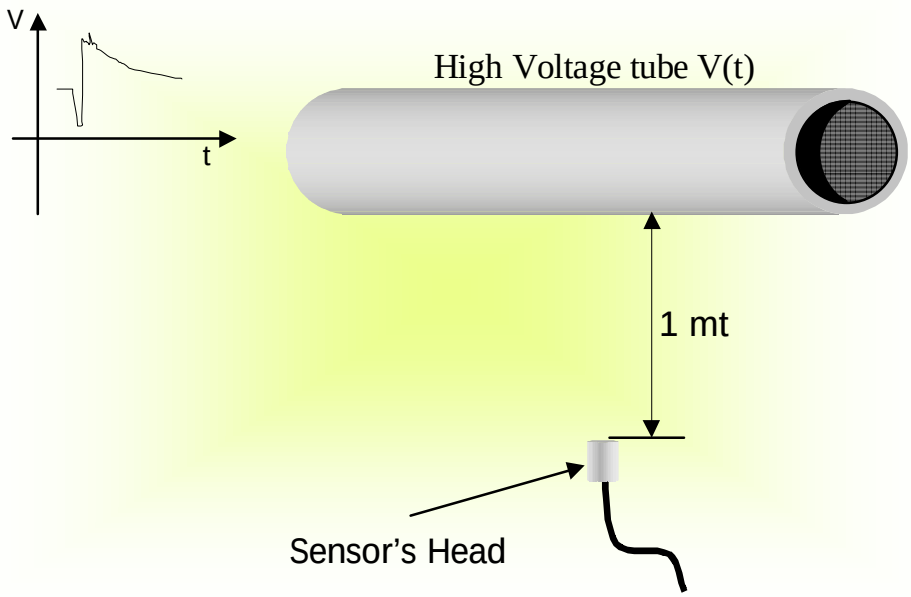

Figure 6.10. Schematic diagram for high voltage pulses measurement

We realized spectral measurements (with a spectrum analyzer ANDO™ AQ 6312B). We can see in Fig. 6.11 the transient response when were applied voltages of 699kv, 807kv and 1000kv. A temporal zoom of the negative impulse of 807kv demonstrate the high

resolution of the sensor response and we observed the sensor head resolution for those pulses. Spectral response of the sensor head, show us the behavior of the electric pulse at the beginning. We can solve for this pulse and is shown in Figure 6.11.

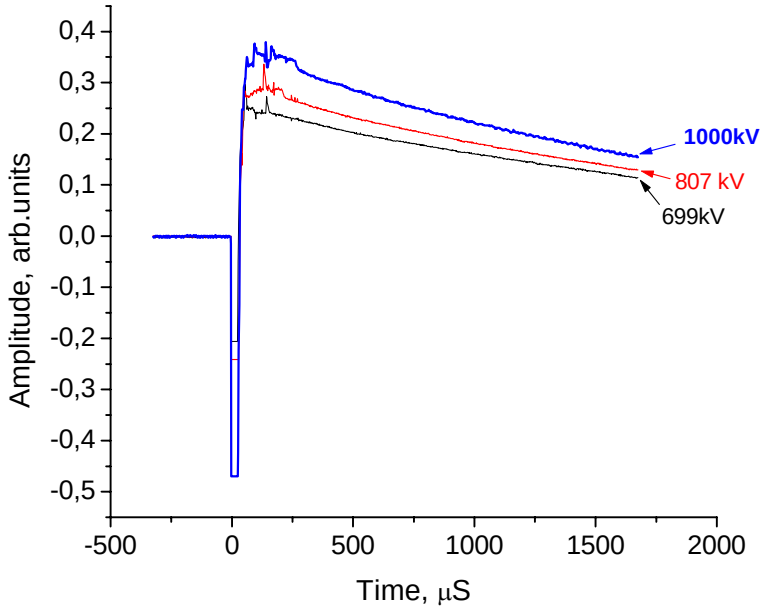

Figure 6.11. High voltage pulses detected at 1 meter from the voltage element V(t)

Taking the signal after 1 mS, we plotted the values and we observe the linearity and the transient response of the sensor element were registered. Sensor's response is plotted in Figure 6.12, from different pulse intensity.

Sensor's response to the transient experiment was of high linearity as we can see from the Figure 6.12. From this response, we obtained next calibration formulae:

$$V_{measured} = 10^4 \times \left(V_{sensor}[V] - \frac{0.028}{1.91} \right) \tag{6.7}$$

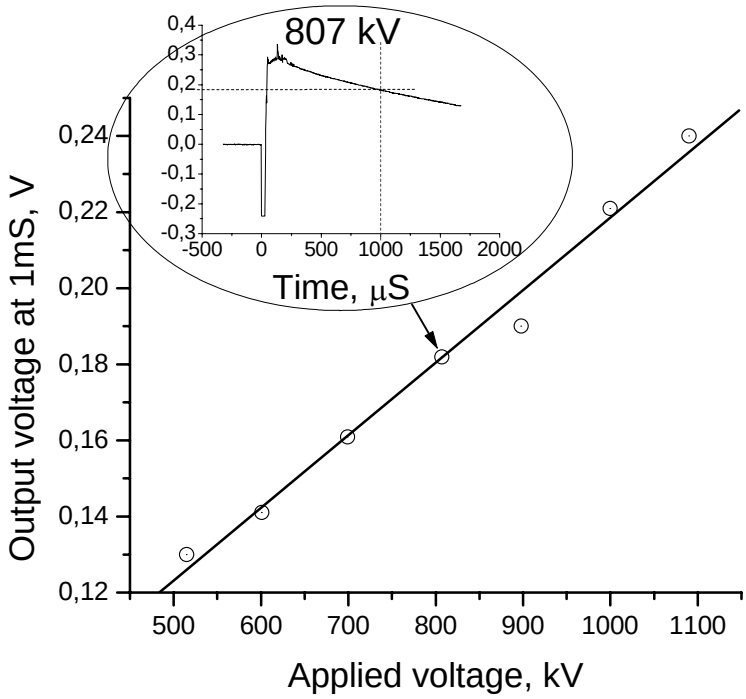

Figure 6.12 Sensor head's response to high voltage pulses.

We observe a negative pulse from the graphic; this negative pulse is solve in details in Figure 6.13 and we interpret this phenomena like a initial spark because the dielectric resistance has been reached when the high voltage pulse is generated. Moreover, Figure 6.13 show us the sensor's definition for pulses of few microseconds.

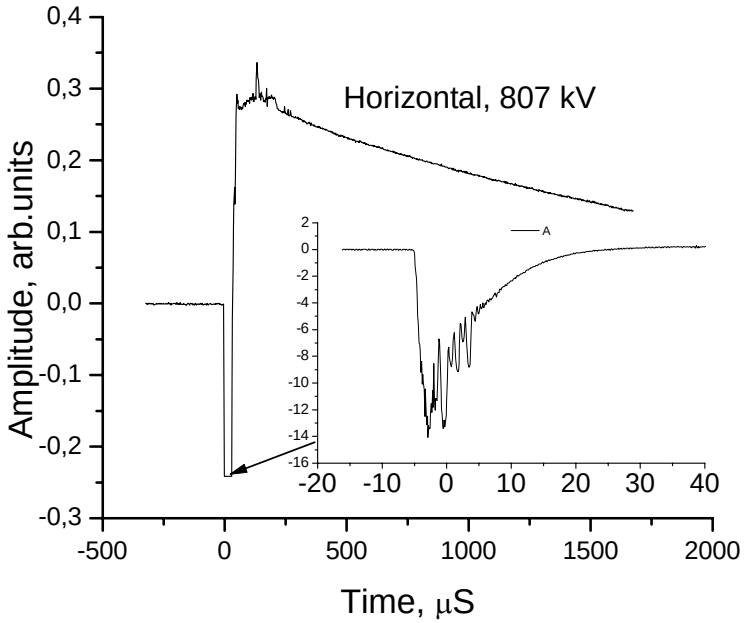

Figure 6.13. Details of the pulse detected by the sensor head.

§6.4 Conclusions and remarks

A remote fibre optic sensor for measuring high voltage in electric transmission lines was presented. This sensor is based on a double pass configuration, which increases the sensitivity and temperature stability. The measurements also show good modulation depth behaviour and with linear response. These advantages allow us to implement FOS in industrial environments where the risk of electric shocks exists, since the proposed FOS is robust and shows a fast response against faster impulse signals.

References

[1] Joseph Rohan Lucas, *High Voltage Engineering*, revised edition, (Open University of Sri Lanka), Chap 6, (2001).

[2] R. E. Hebner, R. A. Malewski and E. C. Cassidy, "Optical methods for electrical measurements at high voltage levels", *Proceedings IEEE*, vol. **65**, pp. 1524-1548, (1977).

[3] Alan J. Rogers, "Optical measurement of current and voltage on power systems", Electric Power Applications, vol. **2**, pp. 120-124, (1979).

[4] Susumu Namba, "High Voltage Measurement by ADP Crystal Plate", *Rev. Sci. Inst.*, vol. **27 A**, No. 5, p. 336, (1956).

[5] Yuji Hamasaki, Hideo Gotoh, Masaaki Katoh, Seiichi Takeuchi, "OPSEF : An Optical Sensor for Measurement of High Electric Field Intensity", *Electron. Le*tt., vol. **16**, No. 11, pp. 406-407, (1980).

[6] Catherine H. Bulmer, W. K. Burns and R. P. Moeller, "Linear Interferometric Waveguide Modulator for Electromagnetic-Field Detection", *Opt. Lett.*, vol. **5** No. 5, pp. 176-178, (1980).

[7] Kunhiko Hidaka and Hiroyuki Fujita, "A New Method of Electric Field Measurements in Corona Discharge Using Pockels Device", *J. Appl. Phys.*, vol. **53** No. 9, pp. 5999-6003, (1982).

[8] Y. Kuhara, Y. Hamasaki, A. Kawakami, Y. Murakami, M. Tatsumi, H. Takimoto, K. Tada and T. Mitsui, "BSO/Fibre-Optic Voltmeter with Excellent Temperature Stability", *Electron. Lett.*, vol **18**, No. 24, pp. 1055-1056, (1982).

[9] Kazuo Kyuma, Shuichi Tai, Masahiro Nunoshita, Noboru Mikami and Yoshiaki Ida, "Fiber-Optic current and voltage sensor using a $Bi_{12}GeO_{20}$ single crystal", *J. Lightwave Technol.*, vol. **LT-1**, No.1, pp. 93-97, (1983).

[10] John P. Dakin and M. C. Holliday, "A Passive All Dielectric Field Probe for R.F. Measurement Using the Electro-Optic Effect", *Proceedings of SPIE*, vol. **468**, pp. 237-240, (1984).

[11] Toshihico Yoshino, “Optical Fiber Sensors for Electric Industry”, *SPIE on Fiber Optic Sensors II*, vol. **798**, pp. 258-265, (1987).

[12] M. Norimatsu and M. Shirasaki, “$Bi_{12}SiO_{20}$ crystal application for voltage sensor in optical fibers”, *Ferroelectrics*, vol. **75**, pp. 189-196, (1987).

[13] Valery N. Filippov, Andrey N. Starodumov, Yuri O. Barmenkov and Vadim V. Makarov, “Fiber Optic Voltage Sensor Based on a $Bi_{12}TiO_{20}$ crystal”, *Appl. Opt*., vol. **39**, No. 9, pp. 1389-1393, (2000).

[14] Valery N. Filippov, Andrey N. Starodumov, Vladimir P. Minkovich and Francisco G. Peña Lecona, “Fiber Sensor for Simultaneous Measurement of Voltage and Temperature”, *IEEE Photonics Technol. Lett*., vol. **12**, No 11, pp. 1543-1545, (2000).

[15] A.Yariv and P.Yeh, *Optical waves in the crystals* (Wiley, New York, 1984).

[16] I. V. Savéliev, *Curso de Física General*, (MIR, Moscú, 1984)

Chapter Seven:

General conclusions and outlook

It has been the purpose of this dissertation to demonstrate the advantages that the $Bi_{12}TiO_{20}$ (BTO) fiber optic voltage sensor offers for industrial applications. It has been found that BTO crystal is the most sensitive, whilst using light at a wavelength of 633nm. BTO retains a good sensitivity even in the near infrared with certain crystal dimensions.

The role of the photoconductivity for operation of fiber optic voltage sensor was investigated and there was found that the degree of photoconductivity in a crystal together the optical power determines a non-uniform sensitivity region not considered before for designing voltage sensors.

Remote sensors with high stability to temperature variations can be made using fiber optics and a BTO crystal. It has been demonstrate in Chapters Four, Five and Six and we can summarize the advances achieved in the following relevant aspects:

1. New configuration of BTO based fiber optic voltage sensor with optically controlled sensitivity has been proposed. The sensor operates at two widely separated wavelengths, one of which is a control signal. Properly chosen wavelength of the control signal, as well as phase retarding element, allow increases or decreases in the sensitivity of the sensor by varying the power of the control signal. For a single wavelength sensor, the sensitivity does not depend of the optical power. In the dual-wavelength sensor, the sensitivity is function of optical powers and a relative phase shift, introduced by a phase retarding element. The main advantage of this sensor includes a remote control of sensitivity and fast changes of a measurable range using a low-power optical signal. Moreover, the control signal enables us to compensate changes in sensitivity caused by temperature variations.

2. New fiber optic voltage and temperature sensor. Taking advantage of a thick phase plate of the voltage sensor, we demonstrate experimentally, that is possible to measure temperature and voltage at the same time avoiding an additional temperature sensor and solving the problem of the temperature stability that this configuration involves.

3. New configuration for high voltage measurements. A double pass configuration for high voltage measurement has been studied and experimentally demonstrated. The use of this sensor allow us to measure high voltage impulses from 1 meter of distance away the electric field source avoiding the risk of electric shock to the user. This remote voltage sensor was implemented and is today in use by Laboratorio de Pruebas de Equipos y Materiales (LAPEM) of Comisión Federal de Electricidad (CFE).

Results obtained throw a new option for voltage sensor with several advantages. This suggests to investigate more materials with similar characteristics than BTO for voltage sensor applications and to investigate several configurations to compensate the temperature dependence and to increase the sensitivity for voltage sensors in general.